

Ultrafast spectroscopy and control of correlated quantum materials

By

Bryan T. Fichera

B.S., University of Pennsylvania (2017)

Submitted to the Department of Physics
in partial fulfillment of the requirements for the degree of

Doctor of Philosophy

at the

MASSACHUSETTS INSTITUTE OF TECHNOLOGY

May 2024

©Bryan Thomas Fichera, 2024. All rights reserved.

The author hereby grants to MIT a nonexclusive, worldwide, irrevocable,
royalty-free license to exercise any and all rights under copyright,
including to reproduce, preserve, distribute and publicly display copies
of the thesis, or release the thesis under an open-access license.

Authored by: Bryan T. Fichera
Department of Physics
May?, 2024

Certified by: Nuh Gedik
Donner Professor of Physics, Thesis supervisor

Accepted by: ?
? Professor of ?
? Chair of ?

Abstract

 Lorem ipsum dolor sit amet, consectetuer adipiscing elit. Etiam lobortis facilisis sem. Nullam nec mi et neque pharetra sollicitudin. Praesent imperdiet mi nec ante. Donec ullamcorper, felis non sodales commodo, lectus velit ultrices augue, a dignissim nibh lectus placerat pede. Vivamus nunc nunc, molestie ut, ultricies vel, semper in, velit. Ut porttitor. Praesent in sapien. Lorem ipsum dolor sit amet, consectetuer adipiscing elit. Duis fringilla tristique neque. Sed interdum libero ut metus. Pellentesque placerat. Nam rutrum augue a leo. Morbi sed elit sit amet ante lobortis sollicitudin. Praesent blandit blandit mauris. Praesent lectus tellus, aliquet aliquam, luctus a, egestas a, turpis. Mauris lacinia lorem sit amet ipsum. Nunc quis urna dictum turpis accumsan semper.

Acknowledgements

Preface

The physics of solids is, to me, one of the most important and fundamental fields of modern science. This might seem, to some, a bit of a hot take. After all, by studying condensed matter physics, one learns next to nothing about, say, the formation of the stars and planets, or the origin of the universe. Nor does one learn about life, death, consciousness, disease, ethics, God, or any other question that perhaps puzzled humanity prior to about five hundred years ago. Certainly no one would argue that condensed matter physics is quite *useless*, given that nearly every device we interact with in modern life required some condensed matter physicist somewhere along the way to make one brilliant discovery or another—yet when the human mind starts to wander, and our thoughts turn to the metaphysical, we tend to look up, not down.

In my work I have taken a quite different view. Condensed matter physics, to me, is ultimately the study of how *truly boring* objects, when brought together in large quantities, *become* interesting, seemingly in spite of themselves. When electrons are put together in a lattice and allowed to interact slightly with the massive nuclei, at low enough temperatures they pair, the low-energy excitations become gapped, and current can flow for infinite times and with absolutely zero energy loss. Those same electrons, with some other set of interactions, may instead ionize (the opposite of pairing!) to create an electrically insulating state, whose low-energy excitation spectrum is nevertheless gapless and consisting of charge-neutral spin- $1/2$ particles. In all such cases, these systems exist in otherwise ordinary-looking rocks, fit in the palm of a hand¹, and are more or less indistinguishable from something you might find sticking into the bottom of your shoe.

While such systems may not tell us a lot² about the early universe, considering these and related problems lets us ask deep, fundamental questions about the world we live in—like, why is this thing a metal, but this thing is an insulator? What do those terms even mean?—that I don’t think we would try to ask otherwise. To me, focusing our attention on

¹Hopefully, gloved.

²This discussion is obviously intentionally reductive. In truth there is still quite a bit one can learn about, e.g. the early universe by studying condensed matter physics, see the Kibble and Pickett [47].

these problems, despite their obviously terrestrial nature, is not a waste of time; rather, I think they remind us that even the most mundane aspects of the human experience involve a level of complexity far beyond what we are capable of understanding absent the pursuit of science.

Throughout the seven years of my Ph.D., I hope to have made a few contributions to this pursuit. As the title of this work implies, I have mainly focused on the application of ultrafast techniques to the study of correlated quantum materials, which I loosely define as those materials in which the interaction between particles is large enough so as to compete with the kinetic energy of those particles. It is in these materials that I think lies the true frontier of condensed matter physics; here, much of our basic intuition about non- or weakly-interacting theory fails, and more complicated notions of phase competition, phase separation, disorder, pairing, coherence, etc. are needed to properly describe the relevant physics.

In my own view, and in the view of many scientists in this field[2], the main question for strongly correlated physics amounts to: “Given a correlated system with some defined combination of different interaction strengths, is there a general theory which allows us to predict the phase diagram of this system *a priori*?” Related of course are questions about the origins of high- T_c superconductivity, strange metallicity, quantum spin liquids, and other exotic phases that we find emerging from strongly interacting systems. Since such a theory does not currently exist, at least with the level of predictive power that I think most would find satisfactory, new advances in this field typically come directly from experiment. Ultrafast optics plays a special role in this regard, for reasons that I will explain in chapter 1.

Progress thus happens in this field somewhat unsystematically, with small pieces of the puzzle added at random, but not infrequent, intervals. Usually it is either new techniques or new materials that are the driving force here. To this end, I have tried to pursue both directions in my Ph.D. Appearing also in chapter 1 is thus a description of the materials I studied the most during my thesis, two of them, CuBr₂ and CaMn₂Bi₂ I consider criminally understudied. On the technique side, almost all of the work presented in this thesis was done using time-resolved second harmonic generation (tr-SHG), a relatively new, nonlinear optical technique which, at the most basic level, probes the point group assumed by the charge distribution function $\rho(\mathbf{x})$ at any given point in time. Second harmonic

generation (SHG) and tr-SHG are tricky techniques, with many pitfalls both practically and theoretically; chapters 2 and 3 are thus devoted to what I hope is a useful, if not fully comprehensive, description of the technique. Chapter 4 is devoted to work that we did developing a new way to control the polarization of the light in a tr-SHG experiment using stepper motors. My hope is that these chapters are useful not only for the new student trying to build their own setup or analyze their own SHG data, but also for people for whom SHG is not a focus but nevertheless want to learn about it in slightly more detail than one would get from a typical paper or review article.

What follows, then, is a description of the three main research works I contributed during my Ph.D.. The first, which I describe in chapter 5, involves work that I did during my second and third years on 1T-TaS₂, a very interesting charge density wave (CDW) material that, among other things, undergoes a mirror symmetry breaking CDW transition at 350 K that shows up in the SHG as a sudden distortion of the flower pattern at that temperature. Since this transition breaks mirror symmetry, two energetically degenerate domains should be present, corresponding to two opposite planar chiralities; in this work, we showed that SHG could differentiate between these two domains (i.e. the flower pattern in either domain looks different).

The second and third works, which I describe in chapters 6 and 7, in contrast to the 1T-TaS₂ work, both involve taking the system out of equilibrium to study the dynamics. In CaMn₂Bi₂ (chapter 6), we discovered that photoexcitation causes the antiferromagnetic (AFM) order in that compound to reorient (relative to equilibrium) to a metastable state which is impossible to reach from the equilibrium state thermodynamically. Light is thus used to *control* the magnetic order in this material.

In CuBr₂ (chapter 7), light is not used to control the order parameter like in CaMn₂Bi₂, but it does excite coherent oscillations of the collective modes of the multiferroic order (electromagnons), whose frequency, amplitude, damping, etc. may be probed in tr-SHG as a function of temperature—a methodology referred to as ultrafast *spectroscopy*. In doing so, we found that one of these collective modes is actually quite special, as it is in fact the analogue of the Higgs mode of particle physics in the context of a multiferroic material.

I conclude with various remarks in chapter 8, as well as an appendix, in which I enumerate briefly all of the null-result experiments I performed

during my Ph.D., in the hopes that future scientists don't have to waste time on what we already know are fruitless pursuits. If you have any questions about this or any other section of this thesis, please do not hesitate to reach out via email.

Contents

Contents	ix
List of Figures	xii
List of Tables	xv
1 Ultrafast optics in correlated electron systems	17
1.1 Spectroscopy	20
1.1.1 Collective modes	20
1.1.2 Coherent oscillations	21
1.1.3 Excitation mechanisms	22
1.1.4 Collective modes in correlated materials	25
2 Second harmonic generation: theory	27
2.1 Space groups, point groups, and Neumann's principle	27
2.2 A classical understanding of SHG	31
2.3 SHG in quantum mechanics	33
2.4 SHG in the Ginzburg-Landau paradigm	37
3 Second harmonic generation: practical	41
3.1 Description of the setup	41
3.2 Before you build	44
3.2.1 Spot size	44
3.2.2 Oblique vs. normal incidence	45
3.2.3 Choice of detector	46
3.3 tr-SHG: methodology	47
3.4 Data analysis	49
3.4.1 Static RA-SHG patterns	49

3.4.2	Modeling χ_{ijk} : the simplified bond hyperpolarizability model	52
3.4.3	Fitting time traces in tr-SHG	53
4	Automated polarization rotation for multi-axis RA-SHG experiments	57
4.1	Preface	57
4.2	Abstract	57
4.3	Introduction	58
4.4	Design	62
4.4.1	Slip Ring	63
4.4.2	Miniature Stepper Motor	65
4.5	Validation and Discussion	67
5	Second harmonic generation as a probe of broken mirror symmetry in 1T-TaS₂	69
5.1	Preface	69
5.2	Abstract	69
5.3	Introduction	70
5.4	Results and discussion	73
5.5	Conclusion	80
5.6	Acknowledgments	80
5.7	Supplemental material	81
5.7.1	Probing broken mirror symmetry with RA-SHG	81
5.7.2	Physical importance of the P _{in} -S _{out} channel	85
5.7.3	Generalization to other mirror symmetry-breaking transitions	87
5.7.4	Probing the sense of planar chirality with RA-SHG	89
5.7.5	Bulk broken mirror symmetry in 1T-TaS ₂	91
5.7.6	Methods	95
6	Light-induced reorientation transition in the antiferromagnetic semiconductor CaMn₂Bi₂	97
6.1	Preface	97
6.2	Abstract	97
6.3	Introduction	98
6.4	Results	100
6.4.1	Equilibrium	100

6.4.2	Nonequilibrium	104
6.5	Discussion	106
6.6	Conclusion	109
6.7	Methods	109
6.7.1	Material growth	109
6.7.2	Tr-SHG measurements	110
6.7.3	PTMB measurements	110
6.7.4	XRD measurements	111
6.7.5	Data availability	111
6.8	Acknowledgments	111
6.9	Author contributions	112
6.10	Supplementary Material	112
6.10.1	Supporting theoretical discussion	112
6.10.2	Nonviability of secondary order parameter in de- scribing the rotational anisotropy SHG (RA-SHG) data	119
6.10.3	Fits to susceptibility tensors	120
6.10.4	Error bar estimation for Fig. 6.11	123
7	Amplitude-mode electromagnon in the XXZ chain CuBr ₂	135
8	Concluding remarks	137
	Bibliography	141

List of Figures

3.1 Schematic drawing of the SHG setup used in this research.	42
3.2 Photograph of the SHG setup.	43
4.1 A demonstration of RA-SHG in the test sample GaAs	60
4.2 A diagram of the full second harmonic generation setup	62
4.3 Exploded-view diagram of one of the automated polarization rotators	64
4.4 A 3-dimensional rendering of the automated polarization rotators	66
4.5 Demonstration of the automatic polarization rotators	67
5.1 Structure of 1T-TaS ₂ and schematic of the SHG setup	72
5.2 SHG in 1T-TaS ₂ above and below $T_{\text{IC-NC}}$	75
5.3 SHG in NC-TaS ₂	76
5.4 RA-SHG in the $S_{\text{in}}S_{\text{out}}$ polarization channel in 1T-TaS ₂	79
5.5 RA-SHG of 1T-TaS ₂ : all polarization channels	81
5.6 Intuition for mirror symmetry breaking in SHG	86
5.7 RA-SHG in the α and β phases of 1T-TaS ₂	90
5.8 Electron diffraction of 1T-TaS ₂	93
5.9 Electric quadrupole RA-SHG in 1T-TaS ₂ ($T = 295$ K)	94
5.10 Electric quadrupole RA-SHG in 1T-TaS ₂ ($T = 356$ K)	94
6.1	101
6.2	102
6.3	105
6.4	107

6.5	Energy difference between x and y -directions with respect to the easy axis. Blue bars indicate the x -direction for the AFM order parameter (OP) is preferred, and red bars indicate the y -direction for the AFM OP is preferred. Note that for strains in experiments, the difference value goes to zero, indicating a change in the in-plane magnetic moment direction.	113
6.6	118
6.7	118
6.8	Fits to the RA-SHG pattern in the four domains of Fig. 6.2 2.0 ps before (A, B, C, D) and \sim 40 ps after (A', B', C', D') zero delay. Data is represented by black circles; solid lines are fits to Eqs. 6.5 and 6.6 with χ^β denoted in the legend.	122
6.9	RA-SHG results of Fig. 6.11 depicted with estimated errorbars (see text).	123
6.10	125
6.11	126
6.12	127
6.13	128
6.14	RA-SHG results of Fig. 6.1 depicted in all four polarization channels ($P_{\text{in}}P_{\text{out}}$, $P_{\text{in}}S_{\text{out}}$, $S_{\text{in}}P_{\text{out}}$, and $S_{\text{in}}S_{\text{out}}$)	128
6.15	129
6.16	RA-SHG results of Fig. 6.3 depicted in all four polarization channels ($P_{\text{in}}P_{\text{out}}$, $P_{\text{in}}S_{\text{out}}$, $S_{\text{in}}P_{\text{out}}$, and $S_{\text{in}}S_{\text{out}}$). The pump fluence is set to \sim 600 $\mu\text{J} \cdot \text{cm}^{-2}$	130
6.17	RA-SHG results in a representative domain as a function of time for different pump polarization states (left circularly- (LCP), right circularly- (RCP), and linearly-polarized). The pump fluence is set to \sim 600 $\mu\text{J} \cdot \text{cm}^{-2}$	131
6.18	RA-SHG snapshots showing a transition to the state opposite to Figs. 6.3(c–d). The pump fluence is set to \sim 600 $\mu\text{J} \cdot \text{cm}^{-2}$. The last row depicts the corresponding value of the AFM OP proposed in the text, relative to the hexagonal crystallographic motif. The schematic representations beneath the RA-SHG plots are for illustration purposes only and the depicted angles are not quantitatively verified.	132

6.19 RA-SHG results in the same domain as Fig. 6.18 plotted out to longer times. The pump fluence is set to $\sim 600 \mu\text{J} \cdot \text{cm}^{-2}$. The last row depicts the corresponding value of the AFM OP proposed in the text, relative to the hexagonal crystallographic motif. The schematic representations beneath the RA-SHG plots are for illustration purposes only and the depicted angles are not quantitatively verified.	133
6.20 SHG intensity in the same domain as Fig. 6.2(f) as a function of temperature.	134

List of Tables

3.1	Vector definition of polarization channels.	50
5.1	Indicators of broken mirror symmetry in RA-SHG	88
6.1	Subgroups obtained by the onset of magnetic order of a given irreducible representation. The columns indicate the irreducible representations, the magnetic group, and the OP direction in the representation space.	116

Chapter One

Ultrafast optics in correlated electron systems

Interactions between electrons in solids can be treated broadly in two different ways, depending on the strength of the interaction. Let us start with the case where the interactions are weak compared to their kinetic energy. In this case, interactions may be treated as a perturbation

$$V = \sum_{\mathbf{p}\mathbf{p}'\mathbf{q},\sigma\sigma'} V(\mathbf{q}) c_{\mathbf{p}+\mathbf{q},\sigma}^\dagger c_{\mathbf{p}'-\mathbf{q},\sigma'}^\dagger c_{\mathbf{p}',\sigma'} c_{\mathbf{p},\sigma} \quad (1.1)$$

on top of the usual hamiltonian

$$H_0 = \epsilon_{\mathbf{p}} c_{\mathbf{p},\sigma}^\dagger c_{\mathbf{p},\sigma} \quad (1.2)$$

for the noninteracting electrons. The key insight, due conceptually to [1] and later formalized by [2], is that, as long as the interactions are sufficiently weak, this problem can be adiabatically connected to a similar problem with non-interacting quasiparticles. Since these quasiparticles are fermions, they obey the Pauli exclusion principle, and the phase space available for scattering low-energy excitations is thus goes to zero at small energies. By Fermi's golden rule, the lifetime of such particles thus approaches infinity as we get closer and closer to the Fermi surface; i.e., there are still well-defined quasiparticles there, even though we started with an interacting Hamiltonian. Such a system is hence referred as a “Fermi liquid,” to signify the fact that we have made only a slight departure from the nominal model of a Fermi gas where the particles are treated as noninteracting.

Fermi liquid theory is almost unreasonably successful in describing the ground state of a large number of correlated electron systems. Truly *most* metals can be very adequately described as a simple Fermi gas with renormalized effective mass, specific heat, etc.; while these modifications may be large (e.g. $m^*/m \approx 10^3$ in CeAl_3), they otherwise look like normal metals. Nevertheless, we can discuss circumstances in which the theory fails. Clearly various electronic instabilities may gap out the Fermi surface, resulting in an insulator; this happens for arbitrarily weak interactions in quasi-1D systems due to the Peierls mechanism, and in higher dimensions due to, e.g., Fermi surface nesting. Whether the interaction is attractive or repulsive determines whether the instability occurs in the charge or the spin channel. In the other limit, where the kinetic energy hamiltonian 1.2 is treated as a perturbation to the interaction term 1.1, the Fermi liquid state gives way to an (Mott) insulating state where the electrons become localized so as to minimize the coulomb repulsion U .

Studying such departures from Fermi liquid theory has become one of the most important fields in condensed matter physics. It is usually referred to as “strongly correlated electron physics”, but many of the instabilities mentioned above are present even in the limit of weak interactions. Much of this interest was spurred by the discovery in 1986 by [2] of high- T_c superconductivity in $\text{Ba}_x\text{La}_{5-x}\text{Cu}_5\text{O}_{5(3-y)}$, although the field has grown to include many other phenomena which occur in the strongly interacting limit that may or may not be related to superconductivity. Despite nearly four decades of research, however, there still exists no universal theory for strongly correlated electron systems, in the sense that, if someone hands you a random strongly correlated material, it is impossible from the outset to *predict* what will be the ground state, what are its low-energy excitations, etc. In fact, it is not even clear such a theory ought to exist[2].

The *field* of strongly correlated physics is thus, in some sense, still very much in its infancy, although that’s not to say there haven’t been huge advances, both theoretically and experimentally, especially since the discovery by [2]. A lot of the effort experimentally has been focused on cataloguing the huge number of different exotic ordered phases—charge density wave, spin density wave, superconducting, strange metals, spin liquids, pseudogap, etc.—that are realized in these systems. Usually this is done by mapping out a phase diagram for a given material, which indicates which phases are present at various values of external parameters like magnetic field, pressure, strain, etc. Ultrafast optics has played an

important role in this respect, as it allows one (heuristically) to add a *nonequilibrium* axis to such phase diagrams. Such experiments, for example, have not only helped illustrate the extent to which different phases compete with one another in the cuprate phase diagram, but also the extent to which the action of the light pulse in strongly correlated materials can be used to tune the properties of those materials for practical purposes. This paradigm is referred to as “ultrafast control,” and I will discuss it in more detail in ??.

A parallel effort in the field of ultrafast optics is to use the pump not to control the state of the material, but rather to excite coherent oscillations of the low-energy collective modes and study these oscillations in the time domain in a pump-probe scheme. This approach is advantageous for two reasons. For one, the frequencies accessible with this technique are bounded from below only by the length of one’s delay stage, in contrast to conventional spectrometer-based methods which involve finite-frequency filters, gratings, etc. Second of all, the ability to select both the excitation mechanism (the pump) and the measurement apparatus (the probe) allows one to design experiments that target specific degrees of freedom of interest. Thus, for example, in multiferroics, one can use SHG to selectively probe the collective modes which modulate the macroscopic polarization. This direction is referred to as “ultrafast spectroscopy,” which I will explain in detail in section 1.1.

This chapter may thus be regarded as an introduction to strongly correlated electron systems, with a special emphasis on ultrafast experiments (of the two types explained above). A complete review of this material is beyond the scope of this thesis; instead, I will focus on a few seminal works that I think tell this story most pedagogically. We will also need a bit of machinery to understand chapters 5 to 7, which focus on CDW, AFM, and multiferroic materials, respectively; hence I will primarily focus on these types of ground states, although of course this obviously misses e.g. strange metal phases, unconventional superconductivity, quantum spin liquids, etc. When appropriate, I point to pedagogical references that may be more useful than this thesis for these and other concepts.

1.1 Spectroscopy

1.1.1 Collective modes

The low-energy excitations of any many-body system are typically *collective*, in the sense that they involve motion of all of the particles in the system rather than just one. Let us consider, for example, the classical model consisting of two identical coupled harmonic oscillators

$$H = \sum_{i=1}^2 \left(\frac{p_i^2}{2m} + \frac{m\omega_0^2}{2} x_i^2 \right) + gx_1x_2, \quad (1.3)$$

with mass m , natural frequency ω_0 , and coupling constant g . When $g = 0$, the normal modes of this system are simply the independent oscillation modes of the two oscillators. However, for any nonzero g , the normal modes involve either symmetric or antisymmetric linear combinations of the two oscillator coordinates; that is, they involve collective motion of the two oscillators. The extension to an ensemble of harmonic oscillators is straightforward; there, too, the normal modes of the Hamiltonian involve collective motion of all of the coordinates at once.

Of course the solids that we are interested in are more complicated than a simple ensemble of harmonic oscillators. Usually, though, more complicated systems can be broken down into a small number of *subsystems* which may, as a first approximation, be treated separately. Thus, for example, it makes sense to refer to the phonon subsystem independently from the electronic subsystem, with different and independent collective mode spectra in the limit where the inter-subsystem coupling goes to zero.

When this coupling is finite, however, many interesting phenomena may occur. For example, spin-orbit coupling coupling—which implies a coupling between spin and orbital degrees of freedom of the electron—can, in the right circumstances, cause the statically ordered state of the spin subsystem to also induce a ferroelectric distortion of the electron orbitals. The normal modes of the system in the presence of this coupling are no longer pure magnon or orbital modes, but rather collective modes of the spin and orbital degrees of freedom together. Let us look at this phenomenon from a different perspective. Suppose we didn't know the ground state of the system, but we did know that the relevant low-energy

excitations involved both spin and orbital degrees of freedom (for example, we might see a response in both the time-resolved kerr rotation as well as the tr-SHG). This is good evidence that the ground state of the system involves this coupling to some extent. Thus, we have learned something quite important about our system without doing anything but look at the low-energy collective excitations.

1.1.2 Coherent oscillations

Clearly understanding the low-energy excitations corresponding to a given ground state is a useful way to understand its properties. So far, however, we have made no mention of how to *probe* these excitations in pump-probe spectroscopy. Let us consider the following Hamiltonian consisting of electrons $c_{k\sigma}$ (with dispersion $\epsilon_{k\sigma}$) and bosons b_q (with dispersion ω_q) interacting via some potential V_{kq}^σ

$$H = \sum_{k\sigma} \epsilon_{k\sigma} c_{k\sigma}^\dagger c_{k\sigma} + \sum_q \hbar\omega_q b_q^\dagger b_q + \sum_{\sigma kq} V_{kq}^\sigma (b_q + b_{-q}^\dagger) c_{k\sigma}^\dagger c_{k+q\sigma}. \quad (1.4)$$

The average lattice displacement is given by

$$\langle u(\mathbf{r}) \rangle \propto \sum_q (\langle b_q \rangle e^{i\mathbf{q}\cdot\mathbf{r}} + \langle b_q^\dagger \rangle e^{-i\mathbf{q}\cdot\mathbf{r}}). \quad (1.5)$$

Clearly, in order for us to have a macroscopic lattice displacement, we need to have a finite value for $\langle b_q \rangle$ and $\langle b_q^\dagger \rangle$, which is impossible if there are a definite number of phonons in the mode \mathbf{q} (since $\langle n | b_q | m \rangle = 0$ for $n = m$). In contrast, if the wavefunction of the system consists of a coherent superposition of different phonon numbers, $\langle u(\mathbf{r}) \rangle$ may acquire a finite value. One thematic example of such a wavefunction is the so-called “coherent state” of the quantum harmonic oscillator

$$|\alpha_q\rangle = \sum_n \frac{\alpha^n e^{-z^2/2}}{n!} (b_q^\dagger)^n |0\rangle, \quad (1.6)$$

although the real wavefunction need not be fully coherent to have a nonzero average lattice displacement.

One can show (see [?]) that the equation of motion for the operator $D_{\mathbf{q}} \equiv \langle b_{\mathbf{q}} \rangle + \langle b_{-\mathbf{q}}^\dagger \rangle$ due to Eq. 1.4 is

$$\frac{\partial^2}{\partial t^2} D_{\mathbf{q}} + \omega_{\mathbf{q}}^2 D_{\mathbf{q}} = -2\omega_{\mathbf{q}} \sum_{\mathbf{k}\sigma} V_{\mathbf{k}\mathbf{q}}^\sigma \left\langle c_{\mathbf{k}\sigma}^\dagger c_{\mathbf{k}+\mathbf{q}\sigma} \right\rangle, \quad (1.7)$$

i.e., $D_{\mathbf{q}}$ obeys a *wave equation* with an inhomogenous part related (in this case) to the electronic subsystem.¹ Thus, if we manage to initialize a wavefunction with a finite $D_{\mathbf{q}}$, the frequency with which $D_{\mathbf{q}}$ oscillates in time is the frequency $\omega_{\mathbf{q}}$ of the boson $b_{\mathbf{q}}$.

The central idea in ultrafast spectroscopy is therefore to excite coherent modes like Eq. 1.6, and then measure the frequency, damping, etc. of these modes by measuring $D_{\mathbf{q}}$. This is in contrast to equilibrium spectroscopies, which measure, for example, the transfer of energy from the light field to states with a definite number of bosons (i.e., $|n\rangle \rightarrow |n+1\rangle$). In theory, of course, the information obtained is the same—the frequency and damping coefficient of the collective modes in question may readily be obtained in the equilibrium spectroscopies as well as in the pump-probe scheme. However, as I argued at the start of this chapter, the pump-probe techniques offer a number of advantages, most notably (i) the ability to design the pump and the probe to specify exactly which excitations we would like to measure, and (ii) the ability to measure much lower frequencies than in conventional spectroscopy due to the energy being measured in the time domain, rather than the frequency domain.

1.1.3 Excitation mechanisms

The next question is how we typically excite these coherent collective oscillations in real materials. The truth is there are many such mechanisms; however, we can start by placing them into two generic categories. *Impulsive* mechanisms involve using the light pulse to apply an effective force to the relevant degrees of freedom in the material, which lasts for the duration of the light pulse; i.e., it is a delta function in time. *Displacive* mechanisms are, in contrast, typically a step function; i.e., the equilibrium position of the oscillator is different before and after the light pulse. One important experimental difference is that impulsive excitation results

¹There will also be a damping term, which may be added phenomenologically but is otherwise not considered in this treatment.

in a coordinate $D_q(t) \propto \sin(\omega t)$, whereas displacive excitation results in $D_q(t) \propto \cos(\omega t)$; this can be seen simply by solving

$$\frac{\partial^2}{\partial t^2} D_q + \omega_q^2 D_q = f(t) \quad (1.8)$$

for $f(t) \propto \delta(t)$ or $f(t) \propto \theta(t)$, respectively.

In absorption

Let us consider the Hamiltonian in Eq. 1.4. We saw that this Hamiltonian resulted in an equation of motion given by Eq. 1.7, which is a wave equation for D_q with a force term

$$f(t) = -2\omega_q \sum_{k\sigma} V_{kq}^\sigma \left\langle c_{k\sigma}^\dagger c_{k+q\sigma} \right\rangle, \quad (1.9)$$

where the time-dependence of the right hand side is complicated but may be phonemnologically modeled. For example, let us suppose that we are in a semiconductor and that photon energy of our pump pulse is greater than the band gap of the material. Thus, the action of the pump is to excite electrons from the valence band into the conduction band. On a very fast timescale (0.1–10 fs) these electrons thermalize with themselves via electron-electron scattering, resulting in a quasi-equilibrium carrier distribution in which electrons and holes have settled at the bottom of the conduction band and the top of the valence band, respectively. Since further decay of these excitations is gapped, the relaxation of this state back to equilibrium may be quite long, especially if the gap is indirect; thus, together with the assumption that the lattice dynamics happen on much longer timescales than the electron thermalization time, it is appropriate to model the force term in Eq. 1.9 as a step function in time

$$f(t) \propto \begin{cases} 0 & t < 0 \\ 1 & t \geq 0 \end{cases}. \quad (1.10)$$

Thus we have the generic result that above-gap excitation typically excites coherent oscillations *displacively*. In the case that the bosons of Eq. 1.4 are phonons, this is known as displacive excitation of coherent phonons (DECP), and was studied by many authors, notably Zeiger et al.

[111]. An important insight which follows from Eq. 1.9 is that, in the limit where the quasi-equilibrium electron distribution doesn't break any symmetries of the original hamiltonian, the applied force also does not break any symmetries. Thus only totally-symmetric phonons may be excited via DECP.

In transparency

While the DECP-like mechanisms tend to dominate when the photon energy is above the band gap, they are forbidden in transparency. In this case, the dominant excitation mechanism is actually impulsive. Let us consider the case of a collective mode with energy $\hbar\omega_0$ which we wish to excite coherently with an ultrafast laser pulse, below the band gap. If the central frequency of the light pulse is resonant with the collective mode (i.e., we have $\nu_{\text{photon}} = \hbar\omega_0$), then we may drive the coherent oscillation directly; i.e., the mode coordinate Q simply follows the electric field. This is of course only possible if the mode carries a finite dipole moment (i.e. it is odd under parity). Alternatively, we will see that, under the right conditions, we can also excite coherent oscillation of low-energy collective modes even if the photon energy is far away from any direct resonance.

To see this, recall that ultrafast laser pulses always have a nonzero bandwidth, proportional to the inverse of the pulse width. In a nonlinear optical effect known as difference frequency generation (DFG), pairs of these frequencies may *interfere* to produce electric field components at the difference frequency between the two members of the pair. Thus, as long as the collective mode in question has a frequency less than approximately the bandwidth $\delta\nu_{\text{photon}}$ of the incident light pulse, there will exist pairs of frequencies (ω_1, ω_2) in that light pulse such that $|\omega_1 - \omega_2| \approx \omega_0$. This electric field will last for the duration of the light pulse, which may be treated as a delta function in time. This phenomenon is referred to as impulsive stimulated raman scattering (ISRS).

Since the force is a delta function in time, the result indeed is an impulsive excitation where the coordinate $D_q(t) \sim \sin(\omega_0 t)$. Unlike the direct excitation mechanism mentioned above, ISRS requires two photons and the force is thus even under parity; i.e., we can only excite even-parity bosons.

It is instructive at this point to consider ISRS in a phenomenological Ginzburg-Landau (GL) model. We start by writing down an effective free

energy

$$F = -[\chi_{ijk} E_i^*(\omega_0) E_j(\omega_{\text{photon}}) E_k^*(\omega_{\text{photon}} + \omega_0) + c.c.] \quad (1.11)$$

with some tensor of coefficients χ_{ijk} (see chapter 2). The effective field P produced by the pump pulse is given by

$$P_i(\omega_0) = -\frac{\partial F}{\partial E_i^*(\omega_0)} \quad (1.12)$$

$$= \chi_{ijk} E_j(\omega_{\text{photon}}) E_k^*(\omega_{\text{photon}} + \omega_0) \quad (1.13)$$

$$(1.14)$$

1.1.4 Collective modes in correlated materials

Chapter Two

Second harmonic generation: theory

2.1 Space groups, point groups, and Neumann's principle

The utility of SHG in studying condensed matter systems is derived from the following simple statement, attributed to Franz Neumann[70] and later Pierre Curie[19]:

Theorem 2.1.1 (Neumann's principle) *Let P_G be the symmetry group of a crystal structure and P_H the symmetry group of some physical property of that crystal. Then, P_G is a subgroup of P_H .*

There are a few things to digest here. Let us start by understanding the meaning of the phrase “symmetry group”. For any given crystal, there exists some infinitely large set of operations G under which the crystal structure is symmetric. Each of these operations may be decomposed into two parts: a “point-preserving operation” R , corresponding to either the identity, rotation, inversion, mirror, or the product of mirror and rotation, followed by a translation by some vector τ :

$$G = \{(R|\tau)\} \tag{2.1}$$

where $(R|\tau)$ means “Perform R , then translate by τ ”. Clearly, the set G forms a group, since if both g_1 and $g_2 \in G$ leave the crystal structure

invariant, so does the product $g_1 g_2$, and so $g_1 g_2 \in G$. Thus, G is called the *space group* of the crystal. In three dimensions, there are 230 crystallographic space groups, which are tabulated in a number of places, most usefully Wikipedia[16].

For 73 of these groups, the translation parts of the τ 's in Eq. 2.1 are only ever linear combinations of integer multiples of the lattice vectors a , b , and c ; these are called *symmorphic* space groups. The remaining 157 groups involve translations that are not integer multiples of the lattice vectors; these are one's screw axes and glide planes, and so these groups are called *asymmorphic*.

Importantly, the “physical properties” of theorem 2.1.1 refer to the truly macroscopic properties of the crystal, like its conductivity, dielectric, or pyroelectric tensors. Consider, for example, that in SHG, we are typically studying the sample at optical wavelengths, where the wavelength of light is three or four orders of magnitude larger than the lattice spacing. Clearly, then, these properties do not care whether the correct symmetry is $(R|\tau)$ or $(R|\tau + a/2)$. A more useful group, then, is the *point group* of the crystal

$$P_G = \{R \text{ s.t. } \exists \tau \text{ s.t. } (R|\tau) \in G\} \quad (2.2)$$

i.e., the point group is the set of point-preserving operations R for which R appears in G , regardless of whether you need to perform a translation with it. Once can show that P_G is also a group, and thus it is P_G which is involved in Neumann's principle for all intents and purposes¹.

The last ingredient that we need to understand theorem 2.1.1 is the concept of what is meant by “physical property”. The idea is that the response of the crystal $J_{i_1 i_2 \dots i_n}$ (i.e., the current J_i , or the quadrupole moment Q_{ij}) is proportional to some field $F_{i'_1 i'_2 \dots i'_m}$ via some tensor χ :

$$J_{i_1 i_2 \dots i_n} = \chi_{i_1 i_2 \dots i_n i'_1 i'_2 \dots i'_m} F_{i'_1 i'_2 \dots i'_m}. \quad (2.3)$$

For example, the conductivity σ_{ij} relates a current density J_i to an applied electric field E_j :

$$J_i = \sigma_{ij} E_j. \quad (2.4)$$

¹Of course this breaks down when the wavelength of light is comparable to the lattice spacing; in that case you need to consider the full space group.

Likewise, the polarization P_i due to the pyroelectric effect is related to the a temperature difference ΔT by a tensor p_i :

$$P_i = p_i \Delta T. \quad (2.5)$$

The tensors σ_{ij} , p_i , and generally, $\chi_{i_1 i_2 \dots i_n i'_1 i'_2 \dots i'_m}$ are commonly referred to as *matter tensors*[81], to emphasize the fact that they are the only part of the response equations that depend on the material. It should be noted that matter tensors generically come in two types: those that transform like a vector under inversion and those that transform like a pseudovector under inversion. You can tell which is which by applying inversion to either side of the response equation. For example, the tensor ϵ_{ij} relating the displacement field to the electric field

$$D_i = \epsilon_{ij} E_j \quad (2.6)$$

is a polar tensor, whereas the tensor χ_{ij}^{me} describing the magnetoelectric effect

$$M_i = \chi_{ij}^{me} E_j \quad (2.7)$$

is an axial tensor.

We are now ready to restate theorem 2.1.1 in a slightly more useful form, using the terminology we have developed about point groups and matter tensors:

Theorem 2.1.2 (Neumann's principle, restated) *Let P_G be the point group of a given crystal, and let χ be a matter tensor describing some response function of that crystal. Then, for all $g \in P_G$, we have*

$$g(\chi) = \chi. \quad (2.8)$$

Eq. 2.8 can be more usefully expressed if we know the matrix R_{ij}^g corresponding to g . For example, if g is “threefold rotation about the z axis”, we have

$$R_{ij}^g = \begin{pmatrix} -\frac{1}{2} & -\frac{\sqrt{3}}{2} & 0 \\ \frac{\sqrt{3}}{2} & -\frac{1}{2} & 0 \\ 0 & 0 & 1 \end{pmatrix}, \quad (2.9)$$

in which case one can show that Eq. 2.8 reads

$$(\det R^g)^t R_{i_1 i'_1}^g R_{i_2 i'_2}^g \cdots R_{i_n i'_n}^g \chi_{i'_1 i'_2 \dots i'_n} = \chi_{i_1 i_2 \dots i_n}, \quad (2.10)$$

where t is 0 if χ is a polar tensor and 1 if χ is an axial tensor. Theorem 2.1.2 tells us that there is one copy of Eq. 2.10 for each $g \in P_G$.

Apparently, each element $g \in P_G$ gives us a *constraint* on the numbers $\chi_{i_1 i_2 \dots i_n}$, in that they have to satisfy Eq. 2.10. This is a remarkably useful fact. Since different point groups enforce different constraints on χ , that means the *form* of χ (e.g. when written as a list of numbers) depends quite sensitively on the point group of the crystal we are studying. As an example, here is the dielectric permittivity tensor for crystals with the point group (in Schoenflies notation) C_2 :

$$\epsilon_{ij} = \begin{pmatrix} a & 0 & e \\ 0 & b & 0 \\ e & 0 & c \end{pmatrix}_{ij} \quad (2.11)$$

versus in the point group D_{3d} :

$$\epsilon_{ij} = \begin{pmatrix} a & 0 & 0 \\ 0 & a & 0 \\ 0 & 0 & c \end{pmatrix}_{ij}. \quad (2.12)$$

Clearly, any *measurement* of ϵ_{ij} will be able to easily differentiate a crystal with point group C_2 from one with point group D_{3d} . This is the fundamental basis, then, for SHG. In SHG, we measure the tensor χ_{ijk} corresponding to the response equation²

$$P_i(2\omega) = \chi_{ijk} E_j(\omega) E_k(\omega); \quad (2.13)$$

the numbers χ_{ijk} thus tell us about the crystallographic point group we are measuring from.

There are a couple of advantages to measuring χ_{ijk} over any other matter tensor in a given system. For one thing, χ_{ijk} is a third rank tensor, which means it has a few more degrees of freedom to work with compared to ϵ_{ij} , and thus does a better job at uniquely specifying each point group. It also doesn't have *too many* degrees of freedom, so that most of the time your experiment will be able to tell you all of your tensor elements³. In addition, since we are typically doing SHG at optical wavelengths, the

²This discussion is a bit simplified in the sense that there are actually *many* response functions which will give you light at 2ω ; for a more detailed discussion, see section 2.2.

³Quadrupole SHG has this problem, see section 2.2.

form of χ_{ijk} reflects the symmetry of the *charge distribution* $\rho(\mathbf{x})$, in contrast to e.g. x-ray diffraction, where the relevant tensors will tell instead you about the electron distribution, $n(\mathbf{x})$. This can be advantageous in cases where the long range order you are trying to study involves an ordering of the valence electrons but not the electrons in the cores of atoms. This is entirely the result of the fact that Neumann's principle, as expressed both in theorem 2.1.1 and theorem 2.1.2, tells us that the point group of our crystal is a *subgroup* of the point group we get from our measurement—the measurement can always be more symmetric than the crystal!

As another example of this fact, let us note that the response equation given by Eq. 2.13 clearly has an additional symmetry $j \leftrightarrow k$, since the two copies of the electric field on the right hand side are equivalent. Obviously this is not a result of the material we are studying, it is simply a fact of doing SHG. Thus, in addition to the constraints given by Neumann's principle and Eq. 2.10, we have the additional constraint

$$\chi_{ijk} = \chi_{ikj} \forall i, j, k. \quad (2.14)$$

This is known as *particularization*[10].

2.2 A classical understanding of SHG

In the last section we considered the SHG response function given by Eq. 2.13. Where does this relationship come from, and how is $P(2\omega)$ eventually measured? Our starting point in the classical treatment will be the inhomogenous electromagnetic wave equation

$$\left(\nabla^2 - \frac{1}{c^2} \frac{\partial^2}{\partial t^2} \right) E_i(\mathbf{x}, t) = S_i(\mathbf{x}, t), \quad (2.15)$$

which we understand as defining the field $E_i(\mathbf{x}, t)$ radiated by the source term $S_i(\mathbf{x}, t)$, which is induced by the incident field. To lowest order in a multipole expansion, $S_i(\mathbf{x}, t)$ is given by[45, 52]

$$\mu_0 \frac{\partial^2 P_i(\mathbf{x}, t)}{\partial t^2} + \mu_0 \left(\epsilon_{ijk} \nabla_j \frac{\partial M_k(\mathbf{x}, t)}{\partial t} \right) - \mu_0 \left(\nabla_j \frac{\partial^2 Q_{ij}(\mathbf{x}, t)}{\partial t^2} \right) \quad (2.16)$$

where $P_i(\mathbf{x}, t)$, $M_i(\mathbf{x}, t)$, and $Q_{ij}(\mathbf{x}, t)$ are the induced electric dipole, magnetic dipole, and electric quadrupole densities, and ϵ_{ijk} is the Levi-Civita tensor.

If the incident electric field is small, then the terms $P_i(\mathbf{x}, t)$, $M_i(\mathbf{x}, t)$, and $Q_{ij}(\mathbf{x}, t)$ are linear functions of that electric field. However, for larger incident fields (such as those generated by pulsed lasers), they may be more generally written as a Taylor series:

$$P_i = \chi_{ij}^{ee} E_j + \chi_{ij}^{em} H_j + \chi_{ijk}^{eee} E_j E_k + \chi_{ijk}^{eem} E_j H_k + \dots \quad (2.17)$$

$$M_i = \chi_{ij}^{me} E_j + \chi_{ij}^{mm} H_j + \chi_{ijk}^{mee} E_j E_k + \chi_{ijk}^{mem} E_j H_k + \dots \quad (2.18)$$

$$Q_{ij} = \chi_{ijk}^{qe} E_k + \chi_{ijk}^{qm} H_k + \chi_{ijkl}^{qee} E_k E_l + \chi_{ijkl}^{qem} E_k H_l + \dots \quad (2.19)$$

where we have suppressed the arguments \mathbf{x} and t for brevity.

Assuming the incident field is monochromatic,

$$E_i(\mathbf{x}, t) = E_i(\omega) e^{i(\mathbf{k} \cdot \mathbf{x} - \omega t)} + \text{c.c.} \quad (2.20)$$

$$H_i(\mathbf{x}, t) = H_i(\omega) e^{i(\mathbf{k} \cdot \mathbf{x} - \omega t)} + \text{c.c.} \quad (2.21)$$

the induced sources are also monochromatic, and (keeping only terms proportional to $e^{i2\omega t}$) we thus get

$$P_i(2\omega) = \chi_{ijk}^{eee} E_j(\omega) E_k(\omega) + \chi_{ijk}^{eem} E_j(\omega) H_k(\omega) \quad (2.22)$$

$$M_i(2\omega) = \chi_{ijk}^{mee} E_j(\omega) E_k(\omega) + \chi_{ijk}^{mem} E_j(\omega) H_k(\omega) \quad (2.23)$$

$$Q_{ij}(2\omega) = \chi_{ijkl}^{qee} E_k(\omega) E_l(\omega) + \chi_{ijkl}^{qem} E_k(\omega) H_l(\omega). \quad (2.24)$$

Since Eq. 2.15 is linear, the electric field radiated by $S_i(\mathbf{x}, t)$ is simply proportional to it. In the limit where the first term of Eq. 2.22 dominates, the intensity measured at our detector thus satisfies

$$I(2\omega) \propto |\hat{e}_i^{\text{out}} \chi_{ijk}^{eee} \hat{e}_j^{\text{in}} \hat{e}_k^{\text{in}}|^2, \quad (2.25)$$

where \hat{e}^{in} and \hat{e}^{out} are unit vectors in the direction of the incoming and measured electric fields⁴. χ_{ijk}^{eee} does typically dominate when inversion symmetry is broken, but if not, you have to consider all of the terms in Eqs. 2.22–2.24. Actually, each of these terms needs to be considered twice, since there is both a surface contribution and a bulk contribution⁵. In my experience, the hierarchy of contributions (from most to least important, and assuming everything is allowed by symmetry) is typically:

⁴Usually there are polarizers in the experiment which define these directions.

⁵The space group which constrains the surface contributions is the bulk space group less the operations which involve some change in the z coordinate.

1. Bulk electric dipole
2. Surface electric dipole, bulk electric quadrupole, and bulk magnetic dipole, at the same order⁶
3. Everything else

I've never seen anything outside of items 1 and 2, but in rare cases an electronic resonance may cause an enhancement in one of the other contributions[31].

Let us take a moment now to emphasize the following extremely common misconception about SHG: just because you see SHG in your experiment, that does not mean that inversion symmetry is broken in your material! It also does not mean that your material is a ferroelectric, or really that there's anything special at all about your material, at least before you've done any further analysis. Similarly, if you *don't* see SHG, that doesn't mean inversion symmetry is preserved, either. I have repeatedly seen large electric quadrupole SHG show up in materials with inversion symmetry, while materials which definitely break inversion symmetry have absolutely zero SHG observable in the experiment. The reason for this is ultimately due to resonance, a topic which I will discuss in section 2.3, but I mention it here because it is truly quite common in the literature and it is surely a mistake worth avoiding. You are "allowed" to say your material breaks inversion symmetry only if there is no other contribution in Eqs. 2.22–2.24 which fits your data, and you are basically never allowed to say that your material preserves inversion symmetry when there is no SHG (a fact that should be obvious on a careful reading of theorem 2.1.1).

2.3 SHG in quantum mechanics

The description of SHG in the previous section is probably the most useful for understanding SHG from an "optics" perspective, but it gives little insight into the true microscopic origin of the SHG intensity. The

⁶Somehow the bulk electric quadrupole and magnetic dipole contributions have been labelled "exotic" by some in the community, but that has not been my experience. If I had to guess, almost half of the materials I have measured with inversion symmetry show electric quadrupole SHG.

quantum description, on the other hand, will tell you exactly where the SHG is coming from microscopically, but only if you have access to the eigenfunctions $|\psi\rangle$ of your hamiltonian—it is of little use otherwise. Nevertheless, we can still gain intuition about the dependence of our SHG intensity on the frequency of the light in the quantum picture, which will be useful for clearing up a whole other slew of misconceptions that have somehow made their way into the SHG literature. This treatment closely follows that of Boyd [13].

The starting point is to describe the system under study as a statistical ensemble specified by a Hamiltonian

$$H = H_0 + \lambda V \quad (2.26)$$

and a density matrix

$$\rho(t) = \sum_i p_i(t) |\psi_i(t)\rangle \langle \psi_i(t)| \quad (2.27)$$

where the $p_i(t)$'s specify the classical probability of the system being in state i at time t , and the $|\psi_i\rangle$'s are wavefunctions given by

$$|\psi_i(t)\rangle = \sum_n c_n^i(t) |n\rangle \quad (2.28)$$

for some $\{c_n^i(t)\}$, where

$$H_0 |n\rangle = E_n |n\rangle \quad (2.29)$$

for all n . In the presence of damping, the elements

$$\rho_{nm} = \langle \psi_n | \rho | \psi_m \rangle \quad (2.30)$$

of ρ satisfy the differential equation

$$\dot{\rho}_{nm} = \frac{1}{i\hbar} [H, \rho]_{nm} - \gamma_{nm} (\rho_{nm} - \rho_{nm}^{(eq)}), \quad (2.31)$$

where γ_{nm} is a matrix of (phenomenological) damping parameters⁷, and $\rho_{nm}^{(eq)}$ is the density matrix corresponding to the equilibrium steady state of the system.

⁷This is just one choice of $p_i(t)$.

We consider the case where V may be treated as a perturbation on top of H_0 , i.e. where λ is small. In this case, Eq. 2.31 can be written

$$\dot{\rho}_{nm} = -i\omega_{nm}\rho_{nm} + \frac{1}{i\hbar} \sum_k \lambda(V_{nk}\rho_{km} - \rho_{nk}V_{km}) - \gamma_{nm}(\rho_{nm} - \rho_{nm}^{(eq)}), \quad (2.32)$$

where $\omega_{nm} = E_{nm}/\hbar$, and we seek a solution

$$\rho_{nm} = \rho_{nm}^{(0)} + \lambda\rho_{nm}^{(1)} + \lambda^2\rho_{nm}^{(2)} + \dots \quad (2.33)$$

Turning the crank (see Boyd [13] for details) gives us the solution

$$\rho_{nm}^{(N)}(t) = \int_{-\infty}^t \frac{1}{i\hbar} [\lambda V(t'), \rho^{(N-1)}(t')]_{nm} e^{(i\omega_{nm} + \gamma_{nm})(t' - t)} dt'. \quad (2.34)$$

Carrying out this series to second order in λ with the perturbation $V(t) = -\boldsymbol{\mu} \cdot \mathbf{E}(t)$, where $\boldsymbol{\mu}$ is the dipole moment and $\mathbf{E}(t) = \sum_q \mathbf{E}(\omega_q) e^{-i\omega_q t}$ is the incident electric field, we get an expression for the density matrix $\rho_{nm}^{(2)}(t)$ as a function of the dipole matrix elements

$$\boldsymbol{\mu}_{nm} = \langle n | \boldsymbol{\mu} | m \rangle, \quad (2.35)$$

the frequencies ω_q , the damping constants γ_{nm} , and $\rho_{nm}^{(0)}$.

Once we have $\rho_{nm}^{(2)}(t)$, we can compute the expectation value

$$\langle \boldsymbol{\mu}(t) \rangle = \sum_{nm} \rho_{nm}(t) \boldsymbol{\mu}_{nm}, \quad (2.36)$$

from which the susceptibility can be computed by taking two derivatives with respect to the electric field amplitudes⁸. Reproducing the final answer

⁸We are specializing here to the case of electric dipole SHG, although the calculation proceeds similarly for magnetic dipole and electric quadrupole.

here (again, from Boyd [13]):

$$\begin{aligned} \chi_{ijk}^{(2)}(\omega_p + \omega_q, \omega_q, \omega_p) = & \frac{1}{2\epsilon_0 \hbar^2} \sum_{lmn} (\rho_{ll}^{(0)} - \rho_{mm}^{(0)}) \times \left\{ \right. \\ & \frac{\mu_{ln}^i \mu_{nm}^j \mu_{ml}^k}{[(\omega_{nl} - \omega_p - \omega_q) - i\gamma_{nl}] [(\omega_{ml} - \omega_p) - i\gamma_{ml}]} \\ & + \frac{\mu_{ln}^i \mu_{nm}^k \mu_{ml}^j}{[(\omega_{nl} - \omega_p - \omega_q) - i\gamma_{nl}] [(\omega_{ml} - \omega_q) - i\gamma_{ml}]} \\ & + \frac{\mu_{ln}^j \mu_{nm}^i \mu_{ml}^k}{[(\omega_{nm} + \omega_p + \omega_q) + i\gamma_{nm}] [(\omega_{ml} - \omega_p) - i\gamma_{ml}]} \\ & + \frac{\mu_{ln}^k \mu_{nm}^i \mu_{ml}^j}{[(\omega_{nm} + \omega_p + \omega_q) + i\gamma_{nm}] [(\omega_{ml} - \omega_q) - i\gamma_{ml}]} \\ \left. \right\}, \end{aligned} \quad (2.37)$$

where $\omega_{nm} = \omega_n - \omega_m$. The SHG susceptibility tensor is then obtained by taking the limit $\omega_p = \omega_q$.

We learned two things by doing the quantum calculation. First of all, clearly if we know all of the eigenfunctions $|n\rangle$ of our unperturbed Hamiltonian, we can calculate the susceptibility tensor *a priori*, although this is obviously difficult except in the simplest of cases. Secondly, we notice that there are two types of denominators in Eq. 2.37: those occurring at 2ω (remember we have set $\omega_q = \omega_p$) and those occurring at ω . Both can cause resonances in the SHG intensity and are observed abundantly in experiment[31]. The existence of resonances in the SHG spectrum makes comparison between different materials quite difficult if reference is made only to the SHG intensity at a single color. In one infamous example, Wu et al. [108] incorrectly attributed the large SHG amplitude at optical wavelengths in TaAs to the presence of Weyl nodes near the Fermi level; later SHG spectroscopy measurements demonstrated that the enhancement was due to a simple band resonance at the excitation frequency used in that paper[76]. The emerging consensus is that the SHG intensity at optical frequencies has more or less nothing to do with the low-energy excitation spectrum or its topology.

2.4 SHG in the Ginzburg-Landau paradigm

While Eq. 2.37 is quite general and completely correct microscopically, it obviously lends very little intuition into what kind of phenomenology we can expect to find in the SHG signal, say, across a phase transition, where the dipole matrix elements which determine Eq. 2.37 certainly change but may not do so in a simple or straightforward way. An alternative approach is to treat SHG in a generalized Ginzburg-Landau paradigm, in which all of the physics of the system is cast in terms of an order parameter $\mathcal{O}_{i_1 i_2 \dots i_r}$. This approach was mainly developed by Sa et al. [85], based off of early work by Pershan [77] in the 1960s.

The key insight of Pershan is that one can define a “time-averaged free energy” in nonlinear optics by considering the term (assuming the incident field $E^{\text{in}}(t)$ is monochromatic with frequency ω)

$$F_{\text{SHG}} = -P_i(2\omega)E_i^{*\text{out}}(2\omega) + \text{c.c.} \quad (2.38)$$

$$= -[\chi_{ijk}E_i^{*\text{out}}(2\omega)E_j^{\text{in}}(\omega)E_k^{\text{in}}(\omega) + \text{c.c.}] \quad (2.39)$$

Since F is a free energy, it must be a real, totally symmetric scalar, and Eq. 2.39 thus gives us a way to *derive* the form of the tensor χ_{ijk} in a particular point group using similar arguments as in section 2.1.

In the context of a (spontaneous) symmetry-breaking transition at T_c , the Ginzburg Landau paradigm asserts that the free energy of Eq. 2.39 still obeys the symmetry group of the high temperature phase, even though the low temperature phase explicitly breaks some of those symmetries. This is because the spontaneous symmetry breaking is considered a property of the *solution* of the free energy minimization problem, rather than a property of the minimization problem itself. Thus, a valid expression for the free energy in the low temperature phase is given by

$$F = -[\chi_{ijkl_1 l_2 \dots l_r}(T > T_c)E_i^{*\text{out}}(2\omega)E_j^{\text{in}}(\omega)E_k^{\text{in}}(\omega) + \text{c.c.}] \mathcal{O}_{l_1 l_2 \dots l_r}. \quad (2.40)$$

Comparing Eqs. 2.39 and 2.40, we have an equation for the SHG susceptibility tensor in the low temperature phase

$$\chi_{ijk}(T < T_c) = \chi_{ijkl_1 l_2 \dots l_r}(T > T_c) \mathcal{O}_{l_1 l_2 \dots l_r}. \quad (2.41)$$

In light of Eq. 2.41, let us consider the consequences of the symmetry of \mathcal{O} on the SHG signal. For simplicity, let us consider a situation that

resembles a ferroelectric phase transition; i.e., the high temperature phase preserves inversion symmetry, but the low temperature phase involves the emergence of a rank-1 order parameter \mathcal{O}_l which is odd under inversion. In that case, we have

$$\chi_{ijk}(T < T_c) = \chi_{ijkl}(T > T_c)\mathcal{O}_l(T), \quad (2.42)$$

i.e. the SHG at low temperature is simply a product of a high-temperature tensor and the order parameter \mathcal{O} . We of course need to check that χ_{ijkl} is allowed in the high temperature phase; here, we need χ_{ijkl} to be an even rank polar tensor, which is allowed in the presence of inversion symmetry (see Eq. 2.10).

Let us now imagine that the polarization \mathcal{O}_l is known to be directed along the y axis, i.e.

$$\mathcal{O}_l = (0, P_0, 0)_l, \quad (2.43)$$

for some P_0 . Then, by Eq. 2.42, we have

$$\chi_{ijk}(T < T_c) = \chi_{ijky}(T > T_c)P_0. \quad (2.44)$$

Besides telling us that the susceptibility tensor is linear in the polarization magnitude P_0 , what this formulation gets us is also that the elements of χ_{ijk} are just the elements of χ_{ijkl} with $l = y$. In many cases this is more information than you would have if you only knew the point group of the low temperature phase!

Eq. 2.41 is also quite useful in the case where the low temperature phase is heterogenous; i.e. the order parameter \mathcal{O} varies spatially from one point to another. This is commonly the case in magnets, for example, where rotational symmetry is spontaneously broken at T_c and the low temperature free energy thus consists of multiple energetically degenerate states related to each other by elements R of the high temperature point group which are broken at low temperature. These states have the same free energy since, again, the symmetry-breaking is due to the order parameter, not due to the free energy itself. The order parameter in the different domains are thus related to each other via

$$\mathcal{O}_{i_1 i_2 \dots i_r}(\mathbf{x}_1) = R[\mathcal{O}_{i_1 i_2 \dots i_r}(\mathbf{x}_2)], \quad (2.45)$$

where the right hand side is given by Eq. 2.10. Combining Eq. 2.41 and Eq. 2.45, the SHG tensor thus satisfies

$$\chi_{ijk}(\mathbf{x}_1) = R[\chi_{ijk}(\mathbf{x}_2)]. \quad (2.46)$$

Eq. 2.46 is the fundamental basis for our SHG works on 1T-TaS₂ and CaMn₂Bi₂, discussed in chapters chapter 5 and chapter 6.

Chapter Three

Second harmonic generation: practical

3.1 Description of the setup

In the last chapter we saw that the SHG intensity in a given crystal is related to the point group, order parameter, band structure, etc. of that crystal via the susceptibility tensor χ_{ijk} . It is also obvious from section 2.1 that the ideal scenario is to be able to measure as many of the numbers χ_{ijk} as possible; after all, if you only measured the xx component of Eqs. 2.11 and 2.12, you would have obtained essentially no information about your crystal whatsoever. The SHG setup that we built (whose design is mostly credited to Torchinsky and Hsieh[99], with some improvements by us which I will discuss below) was designed with exactly this goal in mind. There are two key insights which make this design work: one, the light is obliquely incident on the sample so there is some component of E^{in} directed along the sample normal, and two, we rotate the plane of incidence so that the in-plane field direction sweeps an entire 360° . The first point allows us to measure elements of χ_{ijk} with z indices¹, and the second point makes sure we get all of the x and y elements of χ_{ijk} too. All of the tensor elements are thus given a chance to contribute to the SHG intensity in a given experiment.

With those considerations in mind, let me proceed to give a schematic description of our SHG setup (see Figs. 3.1 and 3.2). Some of the choices

¹Here and unless otherwise noted I define the sample normal to be the z axis.

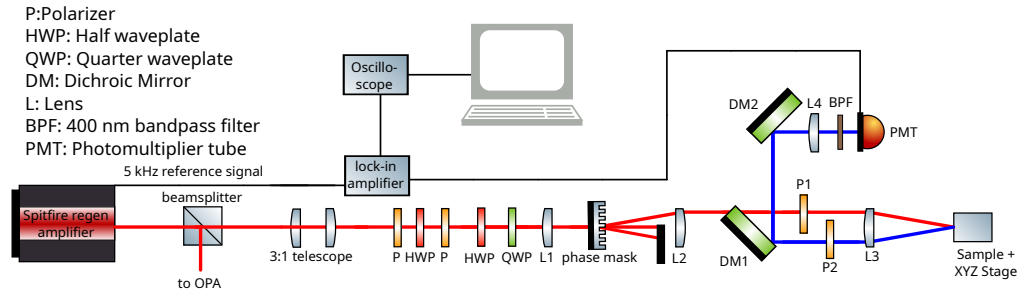


Figure 3.1: Schematic drawing of the SHG setup used in this research. After Morey et al. [68].

we made may seem arbitrary right now, but I will go over them in detail in section 3.2. The starting point is our regenerative amplifier (Spectra-Physics Spitfire Sptf-100f-5k-xp), which produces 100 fs 800 nm pulses at a 5 kHz repetition rate from an 86 MHz seed laser (Spectra-Physics Tsunami 3941-M1S). 90% of the beam is split off to power an optical parametric amplifier (OPA), and the remaining 10% is used for the SHG probe beam. After passing through an optical telescope, which creates a collimated beam of width 1 – 2 mm, this beam is attenuated with a polarizer - half-wave plate - polarizer triplet, and then elliptically polarized with a quarter-wave plate and half-wave plate in series. The ellipticity at this stage is set so the light is perfectly circularly polarized following transmission through a phase mask, as described below.

After passing through these polarization optics, the beam is focused with a lens onto the aforementioned phase mask, which acts as a transmissive diffraction grating and separates the beam into multiple different diffraction orders. The +1 order diffraction comes off at an angle of roughly 7°, while the other orders are blocked with anodized aluminum foil. This (diverging) beam then propagates at 7° to the optical axis before meeting a lens set at the appropriate distance so as to both collimate the beam and rectify the 7° propagation angle. Then, the light passes through a dichroic mirror (which transmits 800 nm and reflects 400 nm), becomes linearly polarized by a wire-grid polarizer, and is then focused onto the sample at a 10° angle of incidence by passing through the edge of a 1 in-diameter 50 mm achromatic focusing lens. The interaction between the light and the sample causes SHG to be radiated in reflection at the same

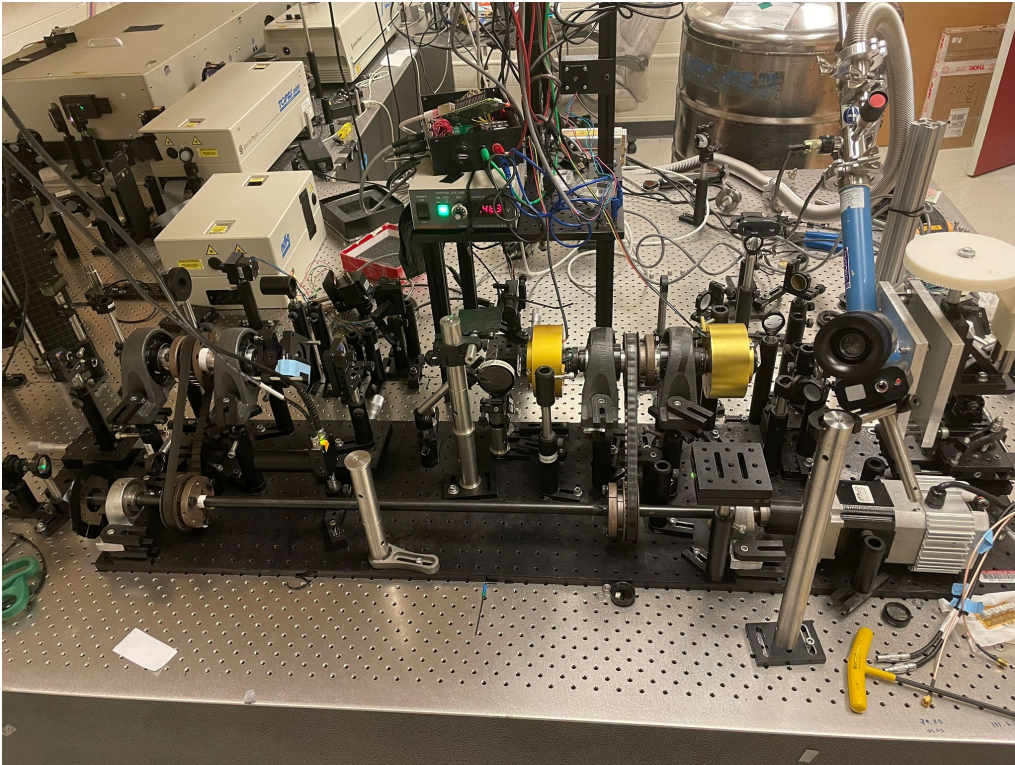


Figure 3.2: Photograph of the SHG setup used in this research. The sample lies in the blue cryostat on the right side of the image. The phase mask is mounted in a black holder with blue masking tape on the left side, and the polarizers are mounted in the two gold-colored slip rings (described in chapter 4).

10° angle of incidence, so that the SHG beam passes through the opposite side of the 50 mm lens before passing through a second, independent polarizer which is used to control the polarization of the measured light.

Finally, the polarized output reflects off of two dichroic mirrors (oriented in such a way as to cancel the differing effect of the Fresnel equations on the reflectivity of S and P polarized light) and is focused through a 400 nm bandpass filter onto a photomultiplier tube (PMT) by a 400 mm lens. The current output of the PMT is filtered by a lock-in amplifier (for static SHG, set to the 5 kHz repetition rate of the laser) and read out on an oscilloscope. The phase mask, incoming polarizer, and outgoing polarizer

are mounted on rotating lens tubes which are connected via pulley to a common motor shaft driven at ~ 5 Hz by a brushless DC motor. The motor thus continuously rotates the plane of incidence of the experiment, since the latter is entirely defined by the phase mask and the polarizers. The rotation angle is tracked as a function of time by an optical rotary encoder, consisting of a laser pointer passed through a chopper wheel (with 100 slots) mounted at the end of the motor shaft and detected via photodiode. The encoder signal and the lock-in signal are both sent to a homemade oscilloscope (an Arduino Uno microcontroller which separates the lock-in signal into different individual rotations by looking for peaks in the encoder signal), the output of which is sent to a computer for further data processing.

3.2 Before you build

I list here a few essential aspects of SHG that should be considered before designing a new setup.

3.2.1 Spot size

One of the most important quantities in an SHG setup is the diameter of the probe spot. Ideally, this diameter is as small as possible, so as to measure the smallest samples or domain sizes. However, there is an important caveat: for constant fluence (i.e. supposing we are limited by the sample damage threshold), the SHG signal to noise ratio scales linearly in the area excited by the probe, and thus SHG microscopes have a difficult time measuring small SHG signals compared to traditional SHG setups with a larger excitation area. To see this, let us say that our detector measures the number of photons per SHG pulse, which is proportional to the pulse energy $U_p(2\omega)$. Assuming the input and output pulse intensity profiles have the shape of a square wave with width τ and height $I_p(\omega)$ and $I_p(2\omega)$, respectively, we have

$$U_p(2\omega) = AI_p(2\omega)\tau \quad (3.1)$$

and

$$U_p(\omega) = AI_p(\omega)\tau \quad (3.2)$$

where A is the area of the beam at the sample surface. The SHG intensity is proportional to the square of the input intensity

$$I_p(2\omega) \propto I_p^2(\omega) \quad (3.3)$$

so that

$$U_p(2\omega) \propto \frac{U_p^2(\omega)}{A\tau}. \quad (3.4)$$

Substituting for the fluence f

$$f(\omega) = \frac{U_p(\omega)}{A} \quad (3.5)$$

we have

$$U_p(2\omega) \propto \frac{f^2(\omega)A}{\tau} \quad (3.6)$$

i.e., if we hold the fluence constant at the sample damage threshold, the number of photons in the generated SHG pulse is proportional to the excitation area and inverse to the pulse width. The signal to noise ratio is then given by

$$\text{SNR} \propto \frac{U_p(2\omega)}{\sqrt{r}} \quad (3.7)$$

where r is the system repetition rate.

3.2.2 Oblique vs. normal incidence

While all of the results presented in this thesis utilized the setup in Fig. 3.1, where the incident beam makes a small angle with respect to the sample normal, plenty of groups use a different approach where that angle is set to 0° . This has the obvious disadvantage of not specifying all of the tensor elements, since any element χ_{ijk} with $i, j, k = z$ is not accessible in this geometry. However, in some cases this can actually be something of an advantage. For example, sometimes unwanted SHG contributions (see section 2.2) may be avoided in the normal incidence geometry, assuming the numerical aperture (NA) of the focusing optic is small enough that longitudinal components of the electric field are nearly zero. Furthermore, in some materials the order parameter only couples to one or two elements of χ_{ijk} ; if none of these elements have a z index, it is needless to complicate the analysis with oblique incidence.

In my experience, oblique incidence seems to be useful in two broad cases. For one thing, some order parameters only show up in the z components of χ_{ijk} (this is the case in 1T-TaS₂, see chapter 5), in which case one obviously needs a nonzero angle of incidence to access these components. A more subtle point is that, even if in practice all of the phenomenology of a particular sample only shows up in the x and y indices of χ_{ijk} , still one must measure the full tensor to *rule out* unseen phenomenology in the other indices. Both the CaMn₂Bi₂ (chapter 6) and CuBr₂ (chapter 7) works presented in this thesis are examples of exactly this point, where the main scientific arguments involve either comparing SHG patterns in two domains or comparing oscillation amplitudes in different polarization channels. Clearly one needs to know all of the tensor elements to make those arguments exact.

3.2.3 Choice of detector

Our setup is somewhat unique in using a PMT for data collection rather than an electron multiplying charge coupled device (EM-CCD), which is the slightly more traditional method. Frankly, this decision was not based on the detection efficiency, but rather the fact that PMTs typically cost about two orders of magnitude less than EM-CCDs. However, the setup construction with a PMT is slightly different than with an EM-CCD, so you should probably decide which you want to use before you start building your setup. With an EM-CCD, the beam is sent into the device without focusing (L4 in Fig. 3.1) so that the beam traces a circle on the sensor as a function of time[37]. The rotational anisotropy signal is read off by performing a radial integration of the camera image (after masking the part of the image which is outside from the circle traced by the beam). In this way, the rotation angle of the motor is correlated with the SHG signal via the azimuthal degree of freedom on the camera image. In contrast, with a PMT the SHG signal is read out as a function of time on an oscilloscope (see section 3.1), and must be correlated with the rotation angle of the motor by some other method. We use an optical chopper wheel attached to the motor shaft; a beam from a laser pointer is directed through the chopper wheel and onto a photodiode, which produces a square wave signal that is used to trigger the oscilloscope. One must also be careful that the PMT is aligned as close to normal as possible to the axis

defined by DM2 and L4 in Fig. 3.1, as the PMT output is actually quite sensitive to the angle of incidence of the input radiation.

As for the detection efficiency of the two devies, an EM-CCD is basically an *array* of PMTs—thus, there is no fundamental difference in the detection efficiencies of the two methods, although having never used an EM-CCD I cannot speak to any specific considerations that might favor one over the other.

3.3 tr-SHG: methodology

Polarization control

The main limitation for doing tr-SHG is simply that the experiment becomes longer. Each measurement of χ_{ijk} requires averaging four different polarization channels ($P_{\text{in}}P_{\text{out}}$, $P_{\text{in}}S_{\text{out}}$, $S_{\text{in}}P_{\text{out}}$, and $S_{\text{in}}S_{\text{out}}$), which, depending on the signal to noise ratio, can take as long as 2 – 3 minutes each. In a time-resolved experiment, that procedure must be repeated at least once for each time delay; in fact, it us often useful to sweep the delay stage multiple times to reduce the extent to which systematic drifts in in the laser power, alignment, etc. affect the time trace. Not only is this time-consuming (typically taking ~ 12 hours to get a good dataset), but it also requires four rotations of the polarizers at each delay, which is simply not feasible if the polarizers are to be rotated manually. Unfortunately, automated polarizer rotation is difficult in the RA-SHG experimental geometry because the polarizers must be rotated relative to a lens tube which is *itself* rotating at 5 Hz. The traditional method of rotating polarizers via stepper motor is thus not possible, unless one finds a method to transmit power between the stationary laboratory frame and the rotating frame that the polarizer lives in. Myself and Karna Morey designed such a method using an electronic device known as a hollow-bore electric slip ring, which uses ring-shaped conductive pads in combination with low-friction metallic brushes to conduct electricity between two rotating objects. In my opinion, such a design is essential to doing tr-SHG unless one is satisfied with only measuring a single polarization channel; thus, I have dedicated the entirety of chapter 4 to our solution, which in my opinion represents the largest contribution we made to SHG methodology during this thesis.

The pump beam path

Having discussed the modifications needed for tr-SHG on the probe arm, let us now describe the pump beam path. 100 fs pulses from the regenerative amplifier (Spectra-Physics Spitfire Sptf-100f-5k-xp) are split by 90 : 10 beamsplitter (with the 10% becoming the probe beam, see section 3.1) and are used as input to an OPA (Light Conversion TP8F1N3) which produces light of variable wavelength between 1100 and 2080 nm. The output of the OPA is directed through a wire-grid polarizer (to pick out the signal or idler, as needed) to an optical delay line (Newport DL125 with SMC100 motion controller) and a second polarizer to vary the beam power. The beam then passes through a NIR (near-infrared) longpass filter to remove unwanted visible wavelengths that are output by the OPA. A 400 nm lens focuses the beam past two mirrors (one mounted with epoxy onto the focusing lens L3 of Fig. 3.1²) and finally onto the sample. The diameter of the pump beam at the focus is set by moving the lens position along the beampath and monitoring the beam shape with a CCD camera. The pointing of the beam is aligned so that the light reflected off the sample is perfectly backscattered. Pump scatter is avoided by mounting a small black circular disk in the center of L3, and by subtracting “dark” scans without the probe beam from the final dataset.

An optical chopper wheel is placed somewhere in the pump beam path which blocks every other pulse from the OPA, so that the effective repetition rate of the pump pulsetrain is 2.5 kHz. The output of the PMT (see Fig. 3.1) is sent to a lock-in amplifier synced to this frequency, so that the output of the lock-in is proportional to

$$I_{\text{Pump+Probe}}^{\text{SHG}} - I_{\text{Probe}}^{\text{SHG}} \quad (3.8)$$

i.e. the output of the lock-in is the pump-induced change in the measured SHG intensity.

Finally, the pump-probe time delay is varied, and for each delay the rotational anisotropy in the SHG intensity is measured in each of the four polarization channels. Alternatively, the motor rotation may be parked at a fixed angle and the SHG intensity at this angle measured as a function of delay time.

²Remember that the probe beam is arriving at oblique incidence and thus passes through the edge, rather than the center, of L3.

3.4 Data analysis

Finally, we discuss the analysis of SHG data, first in the static limit and then in the context of tr-SHG.

3.4.1 Static RA-SHG patterns

The typical static RA-SHG dataset consists of a set of points $\{(\phi_n, I_n^p)\}$, $n \in \{0, 1, \dots, N - 1\}$ and standard errors $\{\sigma_n^p\}$ for each of the four independent polarization channels

$$p \in \{P_{\text{in}}P_{\text{out}}, P_{\text{in}}S_{\text{out}}, S_{\text{in}}P_{\text{out}}, S_{\text{in}}S_{\text{out}}\}.$$

By Eq. 2.13, each of these patterns may be modeled by an equation³

$$I^p(\phi) \propto |\hat{e}_i^{p,\text{out}}(\phi) \chi_{ijk} \hat{e}_j^{p,\text{in}}(\phi) \hat{e}_k^{p,\text{in}}(\phi)|^2, \quad (3.9)$$

where \hat{e} is a unit vector in the direction of the corresponding electric field. These unit vectors are given as a function of ϕ and the angle of incidence θ in table 3.1.

³I will focus on electric dipole SHG for now, although note that the equations for electric quadrupole and magnetic dipole SHG (Eqs. 2.23 and 2.24) are different—by Eq. 2.16, both involve a factor of the incident wavevector \mathbf{k} , and the magnetic dipole term has a cross product.

Table 3.1: Vector definition of polarization channels. θ is the angle of incidence and ϕ is the angle of the plane of incidence with respect to the \hat{x} axis.

Input	Output	$\hat{e}^{\text{in}}(\phi)$			$\hat{e}^{\text{out}}(\phi)$		
		$\hat{e}_x^{\text{in}}(\phi)$	$\hat{e}_y^{\text{in}}(\phi)$	$\hat{e}_z^{\text{in}}(\phi)$	$\hat{e}_x^{\text{out}}(\phi)$	$\hat{e}_y^{\text{out}}(\phi)$	$\hat{e}_z^{\text{out}}(\phi)$
P	P	$\cos \phi \cos \theta$	$\sin \phi \cos \theta$	$-\sin \theta$	$-\cos \phi \cos \theta$	$-\sin \phi \cos \theta$	$-\sin \theta$
P	S	$\cos \phi \cos \theta$	$\sin \phi \cos \theta$	$-\sin \theta$	$-\sin \phi$	$\cos \phi$	0
S	P	$-\sin \phi$	$\cos \phi$	0	$-\cos \phi \cos \theta$	$-\sin \phi \cos \theta$	$-\sin \theta$
S	S	$-\sin \phi$	$\cos \phi$	0	$-\sin \phi$	$\cos \phi$	0

Let us assume that we know the point group P_G of our material. Then, the first step is to constrain the values of χ_{ijk} using the arguments of section 2.1. One can do this manually by solving the system of equations defined by Eq. 2.10, or one can simply look up the answer in one of a number of tables (e.g. Boyd [13])⁴; in the end we are left with a tensor $\chi_{ijk}^{P_G}$ with M independent elements $\{\chi_i, i \in 0, 1, \dots, M - 1\}$.

The goal is to simultaneously fit the four patterns $\{(\phi_n, I_n^p)\}$ to Eq. 3.9 using the χ_i 's. Our objective function is thus

$$f(\{\chi_i\}) = \sum_{p \in \{P_{\text{in}} P_{\text{out}}, P_{\text{in}} S_{\text{out}}, S_{\text{in}} P_{\text{out}}, S_{\text{in}} S_{\text{out}}\}} \sum_{n=0}^{N-1} \left(\frac{I^p(\phi_n) - I_n^p}{\sigma_n^p} \right)^2 \quad (3.10)$$

with $I^p(\phi)$ defined in Eq. 3.9. Unfortunately, such a function is quite difficult to minimize. The reason is that $I^p(\phi)$ is ultimately a sum of products of trigonometric functions of ϕ (due to table 3.1) which can be difficult for typical minimization algorithms. An alternative is to cast the problem in terms of the Fourier transforms (FTs)

$$\hat{I}^p(k) \equiv \frac{1}{2\pi} \int_0^{2\pi} I^p(\phi) e^{-ik\phi} d\phi \quad (3.11)$$

of $I^p(\phi)$ and the discrete Fourier transforms (DFTs)

$$\{(k, \hat{I}_k^p)\}, \quad (3.12)$$

of $\{(\phi_n, I_n^p)\}$, where⁵

$$\hat{I}_k^p \equiv \frac{1}{N} \sum_{n=0}^{N-1} I_n^p e^{-ik\phi_n}. \quad (3.13)$$

Since the DFT is unitary, the uncertainties $\hat{\sigma}_k^p$ are simply the DFT of the σ_n^p 's. Thus, our new objective function is

$$f(\{\chi_i\}) = \sum_{p \in \{P_{\text{in}} P_{\text{out}}, P_{\text{in}} S_{\text{out}}, S_{\text{in}} P_{\text{out}}, S_{\text{in}} S_{\text{out}}\}} \sum_{k=0}^{N-1} \left(\frac{\hat{I}^p(k) - \hat{I}_k^p}{\hat{\sigma}_k^p} \right)^2. \quad (3.14)$$

⁴Be aware that these tensors are given in just one of many choices of coordinates; a rotation of χ_{ijk} may be needed to agree with the orientation of the crystal in the experiment.

⁵I am assuming the ϕ_n 's are equally spaced.

This is a much easier function to minimize for two reasons: one, the function is now just a quadratic function of the $\{\chi_i\}$'s, and two, since there are only six factors of trigonometric functions of ϕ in $I^p(\phi)$, $\hat{I}^p(k) = 0$ for $k \notin \{-6, -5, \dots, 6\}$ ⁶ (the other terms in Eq. 3.14 just contribute an overall constant to f).

What is left then is just the choice of minimization algorithm. Unfortunately, simple gradient descent algorithms are not ideal here unless you have a really good initial guess, since Eq. 3.11 is still quadratic in the fitting parameters and the global minimum is often surrounded by many local minima which can easily cause these algorithms to become trapped. Global minimization routines are thus optimal; I have used the simulated annealing algorithm of Xiang et al. [110] with success, as well as the related “basinhopping” algorithm of Wales and Doye [102], both of which are implemented in `scipy.optimize`[100]. Ultimately, though, it is up to the experimenter to ensure they have found the true global minimum of Eq. 3.14.

As part of this thesis, I wrote a software package in Python called ShgPy which uses `sympy`[65] to compute the FT model Eq. 3.11 and `scipy.optimize`[100] to fit this model to the data via Eq. 3.14. Installation instructions and a comprehensive documentation may be found at the project home page <https://bfichera.github.io/shgpy/>.

3.4.2 Modeling χ_{ijk} : the simplified bond hyperpolarizability model

Sometimes the symmetry-constrained χ_{ijk} of section 3.4.1 is difficult to analyze (perhaps it has too many fitting parameters), in which case it might be prudent try and justify an even more tightly constrained χ_{ijk} via some a microscopic model. We have already seen two such models via Eqs. 2.37 and 2.41, but the former is typically not tractable and the latter may only be valid in the presence of a spontaneous symmetry-breaking phase transition with a well-defined order parameter. One alternative is to model the microscopic charge degrees of freedom classically—suppose most of the motion of charges in our solid occurs in the bonds between atoms, and that that motion is constrained to occur along the bond direction only.

⁶This is the case for electric dipole SHG; for electric quadrupole and magnetic dipole, we can have as much as $k = \pm 8$.

Then, the solid can be modeled as an ensemble of oscillating dipoles (one for each bond in the unit cell) with corresponding hyperpolarizabilities $\{\alpha_n\}$. Symmetry may dictate how many independent α_n 's there are in the unit cell, but otherwise these are considered unknown and to be fit to the data. The electric dipole SHG response of such an ensemble was analyzed by Powell et al. [80], and the electric quadrupole response was later considered by Bauer and Hingerl [7]; the answer in both cases is quite simple:

$$\chi_{ijk}^{eee} = \sum_n \alpha_n b_i^n b_j^n b_k^n \quad (3.15)$$

$$\chi_{ijkl}^{gee} = \sum_n \gamma_n b_i^n b_j^n b_k^n b_l^n \quad (3.16)$$

where b^n is a unit vector in the direction of bond n and the α_n 's and γ_n 's are the unknown parameters of the dipole and quadrupole models, respectively.

When valid, this simplified bond hyperpolarizability model (SBHM) is powerful for two reasons: for one, Eqs. 3.15 and 3.16 typically have fewer unknown parameters than the naive, symmetry-constrained tensor $\chi_{ijk}^{P_G}$ of section 3.4.1, and two, there is a direct connection between the unknown parameters α_n and γ_n and the microscopic degrees of freedom. One can thus draw conclusions *about* the microscopic degrees of freedom by fitting the SHG patterns to Eqs. 3.15 and 3.16 (see, e.g., Ron et al. [84]). Of course, one must be careful that the assumptions of this model—that the charges are localized to the bonds, and that the only relevant motion is along the bond direction—are actually correct before proceeding with this sort of analysis.

Myself and Karna Morey built a comprehensive interface to the SBHM in Python using pymatgen[73], which takes an arbitrary crystallographic information file (CIF) and calculates the relevant susceptibility tensors via Eqs. 3.15 and 3.16. The change to the susceptibility tensor induced by an elastic distortion mode ($\chi_{ijk}(q)$, where q is the mode amplitude) can be computed via integration with ISODISTORT[15, 94]. See the package documentation (<https://github.com/morey18k/sbhm.git>) for examples and further information.

3.4.3 Fitting time traces in tr-SHG

As the final section of this chapter, let me remark on a few aspects of fitting time-domain signals that are not necessarily specific to SHG, but are nevertheless essential for tr-SHG analysis.

Typically, in tr-SHG we plot the pump-induced change in the SHG intensity at a single angle ϕ_0 as a function of the delay time t ; more complicated analysis of the tensor elements themselves is possible but often unnecessary. This intensity change $\Delta I_{2\omega}(t, \phi_0)$ is related to $P(2\omega)$ via

$$\Delta I_{2\omega}(t, \phi_0) = I_{2\omega}^{\text{Pump+Probe}}(t, \phi_0) - I_{2\omega}^{\text{probe}}(0, \phi_0) \quad (3.17)$$

$$\propto |P_{2\omega}(0, \phi_0) + \delta P_{2\omega}(t, \phi_0)|^2 - |P_{2\omega}(0, \phi_0)|^2 \quad (3.18)$$

$$\propto 2P_{2\omega}(0, \phi_0)\delta P_{2\omega}(t, \phi_0) + |\delta P_{2\omega}(t, \phi_0)|^2 \quad (3.19)$$

where we have used that the signal is presumably independent of time if there is no pump pulse. When $|\delta P_{2\omega}(t, \phi_0)| \ll |P_{2\omega}(0, \phi_0)|$, this reduces to

$$\Delta I_{2\omega}(t, \phi_0) \propto P_{2\omega}(0, \phi_0)\delta P_{2\omega}(t, \phi_0). \quad (3.20)$$

The basic problem is then that we have a dataset

$$\{t_n, I_n\}, n \in \{0, 1, \dots, N - 1\} \quad (3.21)$$

with uncertainties σ_n which we wish to fit to some model, typically consisting of some (e.g. polynomial) background

$$b(t, \{b_k\}), k \in \{0, 1, \dots, K - 1\} \quad (3.22)$$

plus 1 to M damped harmonic oscillators

$$I(t, \theta) = \begin{cases} 0 & t < 0 \\ b(t, \{b_k\}) + \sum_{m=1}^M A_m e^{-t/\tau_m} \cos(2\pi f_m t + \psi_m) & t > 0 \end{cases}, \quad (3.23)$$

where θ refers to the set of unknown parameters $\{b_k\}$, $\{A_m\}$, $\{\tau_m\}$, $\{f_m\}$, and $\{\psi_m\}$. We wish to determine the model coefficients θ by minimizing the objective function

$$f(\theta) = \sum_{n=0}^{N-1} \left(\frac{I(t_n, \theta) - I_n}{\sigma_n} \right)^2. \quad (3.24)$$

Various algorithms exist to find the minimum θ_0 of f ; the Levenberg-Marquardt (LM) algorithm [56, 62] is known to have trouble with exponential functions, so it is recommended to do a Nelder-Mead search [69] first and then use LM to refine the solution. These methods also report the uncertainties $\{\sigma_i\}$ on each fitting parameter, basically by computing the curvature of the function f near θ_0 (which depends, among other things, on the data uncertainty $\{\sigma_n\}$). Importantly, however, these uncertainties are only valid when f is a linear function of the model parameters near the minimum!⁷ This is a point which is completely overlooked in the ultrafast condensed matter literature, even though there is really no reason that Eq. 3.24 should satisfy this criterion for typical uncertainty levels in pump-probe experiments.

The correct approach in this case is to note that the data set $D_0 \equiv \{t_n, I_n\}$ is just one of many possible datasets D_0, D_1, D_2, \dots that we *could* have measured during our experiment.⁸ If we could run the minimization procedure described above for each of these hypothetical datasets, we would end up with a whole distribution of model coefficients $\theta_0, \theta_1, \theta_2, \dots$ from which our measurement θ_0 was just a single draw. The spread of this distribution (or, more precisely, the spread of the distribution $\theta - \theta_{\text{true}}$) reflects exactly the quantitative uncertainty in our measurement of θ that we would like to report.

Our goal, then, is to approximate this distribution by some method. One approach (which works when we have many observations $\{t, I\}$ with the same t) is called the nonparametric bootstrap[18]. For each time t_n , let us say that we have a set of measured intensities $\{I_m^n\}$, with $m \in \{1, 2, \dots, M_n\}$. Then, we generate new hypothetical datasets $\mathcal{D}_1, \mathcal{D}_2, \dots$ by (for each t_n) drawing M_n items *with replacement* from the $\{I_m^n\}$'s. The fact that this new distribution of datasets is a faithful representation of the true distribution $\{D_0, D_1, D_2, \dots\}$ is not obvious, but theoretical work by many authors (see Wackernagel [101] for a review) has established that it is nevertheless true.

If we are confident that our model $I(t, \theta)$ is, in fact, the true model (at least for some set of coefficients θ_{true}), then rather than using the dataset D_0 to generate our hypothetical datasets, we can instead choose to use the model *itself*. The idea is to take our estimate $I(t, \theta_0)$ and generate new

⁷Here, “near” means “in a neighborhood of size σ_i .

⁸The following discussion closely follows that of *Numerical Recipes*, chapter 15[82].

datasets $\{\mathcal{D}_m\}$ essentially by adding noise:

$$\mathcal{D}_m = \{(t_n, I(t_n, \theta_0) + N_n), n \in \{0, 1, \dots, N - 1\}\}, \quad (3.25)$$

for some random variable N_n which we put in by hand. This is called the parametric bootstrap, referring to the fact that we are estimating our true distribution $\{D_0, D_1, D_2, \dots\}$ via the parameters θ_0 [21]. In order for the distribution of \mathcal{D}_m 's to faithfully represent the true distribution $\{D_0, D_1, D_2, \dots\}$, obviously N_n needs to reflect the actual noise distribution of the experiment. Thankfully, in pump-probe experiments, we usually know this distribution—as long as we have enough points (t_n, I_n) with $t_n < 0$, we can estimate N_n with a normal distribution centered about 0 with variance $\langle (I_n)^2 \rangle_{<0} - \langle I_n \rangle_{<0}^2$, where $\langle \cdot \rangle_{<0}$ means “average over points with $t_n < 0$.”

Once we have the hypothetical datasets $\{\mathcal{D}_m\}$ (regardless of how we generated them), we proceed by estimating a θ_m for each one using Eq. 3.24, and then plotting the distribution $\{\theta_m - \theta_0\}$; the spread of this distribution tells us the uncertainties σ_i in each of our model coefficients. The important part is that these uncertainties are much more reflective of the true uncertainty in our measurement of θ than the curvature of Eq. 3.24 near θ_0 , which we have argued is strictly incorrect in many cases.

Chapter Four

Automated polarization rotation for multi-axis RA-SHG experiments

4.1 Preface

This chapter is based on a manuscript intended for standalone publication and modified to fit the format of this thesis. It was coauthored by myself and Karna Morey (as co-first authors), along with Baiqing Lv, Zongqi Shen, and Nuh Gedik. Karna Morey and I initiated the project, designed and built the polarization rotators, performed the demonstration experiment, and wrote the paper. Baiqing Lv and Zongqi Shen contributed to the design and helped review the manuscript. Nuh Gedik supervised the project.

4.2 Abstract

RA-SHG is a nonlinear optical technique used to probe the symmetry of condensed matter systems. Measuring the dependence of the SHG susceptibility on one or more external parameters, notably strain, field, temperature, or time delay, is an extremely powerful way to probe complex phases of quantum materials. Experimentally, extracting maximal information about the SHG susceptibility tensor requires measurements of S and P polarized input and output combinations, which naturally

involves the rotation of the polarizers during data collection. For multi-axis experiments, this has proved challenging since polarization rotation is typically done manually. Automating this process eliminates labor constraints, reduces uncertainty due to low-frequency noise, and expands the type of multi-axis datasets that can be collected; however, it is difficult due to geometrical constraints within the setup. In this work, we design and implement low-cost, high-fidelity automated polarization rotators for use in multi-axis RA-SHG. These polarization rotators utilize an electrical slip ring to transfer power to the rotating RA-SHG optical setup as well as a miniature stepper motor to perform the polarization rotation. We demonstrate this automated system in time-resolved RA-SHG measurements in the non-centrosymmetric semiconductor GaAs. For the multi-axis measurements described above, this automated system permits data averaging over longer periods, vastly expedites data collection, and expands the setup measurement capability. This ultimately opens new frontiers in probing quantum materials using multiple tunable external parameters.

4.3 Introduction

Probing the structure of crystalline solids is essential to understanding their intrinsic functionalities. Traditionally, diffraction techniques based on the scattering of e.g. x-rays are used to determine this structure; however, these techniques predominantly measure the total electron density and are thus insensitive to long-range ordering of the valence electron subsystem. In contrast, nonlinear scattering techniques at optical frequencies like RA-SHG are sensitive rather to the total charge density, and thus offer a complementary view of the electronic, magnetic, and lattice properties of quantum materials [27, 99].¹

Furthermore, due to the non-invasive nature of RA-SHG, it can also be used to investigate changes along one or more measurement axes, such as strain, field, pressure, temperature, or time delay. The phase diagram of quantum materials is heavily influenced by these independent variables, and thus, changes to the SHG response along such measurement axes are of great interest. For example, previous studies have used various

¹In this paper, we discuss RA-SHG, although the results are fully generalizable to arbitrary harmonics, e.g. third harmonic generation.

continuous experimental parameters such as pressure [57], time delay[89], and magnetic field to investigate phase transitions in quantum materials. Such measurements can illuminate the roles that charge, spin, and thermal degrees of freedom play within quantum materials.

Second harmonic generation gleans microscopic information through the coupling of an order parameter to the second harmonic susceptibility tensor (at least a third-rank tensor with 18 independent components) [13]. This tensor governs the relationship between the vector properties (i.e. polarization and intensity) of the incident radiation and the generated second harmonic, as shown in Eq. 4.1. The complexity of this tensor means that a significant amount of data is needed to fully resolve the tensor components, posing experimental challenges with data collection. The importance of resolving the tensor components can be seen by considering Neumann's principle, which states that these tensors must be invariant under symmetry operations of the material's point group, which constrains the tensors' independent and nonzero elements [10]. By measuring the intensity and polarization of the generated second harmonic radiation, RA-SHG provides information about these tensor elements and thus the underlying point group. When performing experiments with more than one measurement axis, the data constraints mentioned above can often be especially burdensome, limiting the type of experiments that can be performed using RA-SHG. Thus, new methods for collecting data efficiently for multi-axis RA-SHG experiments are incredibly important.

A more detailed understanding of the information that needs to be collected to fully resolve the second harmonic susceptibility can be seen by considering Fig. 4.1. Fig. 4.1 shows a schematic of an RA-SHG setup, where near-infrared light from the laser source enters at oblique incidence and is scattered off the front of the sample, generating blue light at the second harmonic frequency. To leading order, the measured second harmonic intensity is given by

$$I(\phi) = |E_i^{\text{out}}(\phi)\chi_{ijk}^{(2)eee}E_j^{\text{in}}(\phi)E_k^{\text{in}}(\phi)|^2, \quad (4.1)$$

where ϕ is the azimuthal angle between the crystallographic axes and the plane of incidence, E^{out} and E^{in} are the polarization vectors of the outgoing and incoming light, respectively, and $\chi^{(2)eee}$ is the SHG electric-dipole susceptibility tensor. For certain values of ϕ , as shown in Fig. 4.1(a), the sample is symmetric with respect to the polarization axis of the incoming light; in this case, the second harmonic generation is constrained

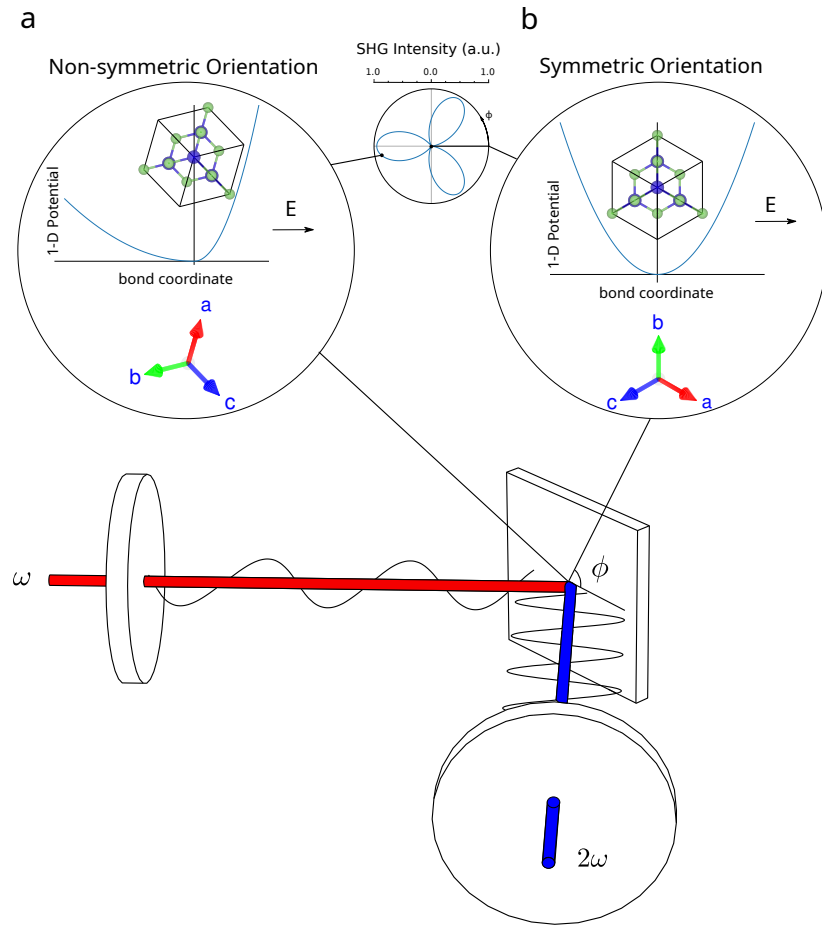


Figure 4.1: A demonstration of RA-SHG in the test sample GaAs. 800 nm light comes in at an oblique angle of incidence, after being passed through a polarizer. The polarization axis of the light is in the plane of incidence and is denoted in the insets of the figure with a black arrow. Depending on the angle of the plane of incidence relative to the crystallographic axes, as well as the polarization of the beam relative to that incoming plane of incidence, the second harmonic response to the stimuli should vary from zero points (nodes) to non-zero maxima.

to be zero, whereas in general arbitrary angles give a non-zero second-harmonic response (see Fig. 4.1(b)). Neumann’s principle dictates that Eq. 4.1 captures the symmetry considerations shown in Fig. 4.1, i.e. the symmetries of the crystal are embedded into its nonlinear susceptibility tensor $\chi^{(2)}$.

These considerations demonstrate the necessity of measuring the full rotational anisotropy of the SHG response, as well as its dependence on the incoming and outgoing polarization directions (which may be P or S-polarized, leading to four independent polarization channels). The former requires rotating the plane of incidence, which is typically done by rotating the optical setup itself rather than the sample [27, 28, 78, 99]. The geometric constraints involved in rotating the optical setup make it challenging to use electromechanical components to rotate the polarizers shown in Fig. 4.1 between S and P configurations, since naively it is difficult to transfer power to the rotating frame of reference. Because of this, switching between different polarization channels is typically done manually, resulting in time and labor constraints that often limit data collection beyond a single polarization combination [89]. Such constraints severely restrict the ability to infer tensor elements from the RA-SHG data and limit RA-SHG to studies involving often just a single tuning parameter.

Previous multi-axis RA-SHG studies typically either collected exclusively one polarization channel [89] (for more than one axis) or simply sacrificed the quantity of collected data and therefore inferred statistics. However, these approaches can often miss certain features in RA-SHG data that would be apparent if more efficient data-taking methods were available. For example, phase transitions in which the order parameter couples differently to different polarization channels through the second harmonic susceptibility [28] are best characterized by taking the full rotational anisotropy data. The benefit of collecting all four polarization combinations underscores the appeal of automated polarization control of RA-SHG setups.

In this work, we design and implement automated polarization rotators for use in multi-axis RA-SHG measurements. The devices utilize a miniature stepper motor housed in an electrical slip ring to circumvent the geometrical constraints imposed by the rotating plane of incidence. In section 4.5, we discuss the specific application of automated polarization rotation to time-resolved RA-SHG and show that it not only expedites

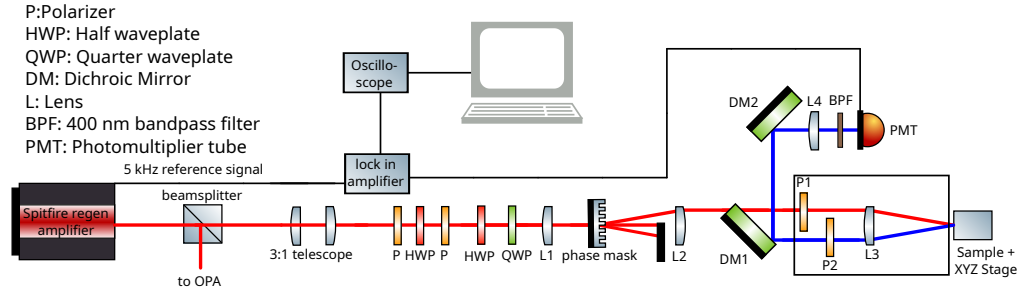


Figure 4.2: A diagram of the full second harmonic generation setup developed and described in Fichera et al. [27]. Boxed in part of the setup shows the area of interest of this work, where the incoming and outgoing polarization channels are set.

data collection but also reduces the setup's sensitivity to low-frequency noise. The advantages afforded by the automated polarization rotators exist not only for time-resolved measurements but for any measurements where an external parameter is being varied and compound rapidly as multiple parameters are varied at the same time.

4.4 Design

A detailed schematic of the RA-SHG setup is shown in figure 2. Telescopied pulses from a 5 kHz pulsed regenerative amplifier (Spectra-Physics Spitfire) are attenuated using a half-waveplate set between two polarizers and then elliptically polarized using a half-waveplate and quarter-waveplate in series. The light is then focused by a lens onto a rotating phase mask (which separates the beam into different diffraction orders), and a beam block selects the +1 order beam which is then collimated using another lens (L2). Finally, the beam passes through a dichroic mirror and a polarizer (P1) before being focused by a third lens (L3) onto the sample. The reflected radiation is passed through an analyzer (P2) and is redirected using a dichroic mirror periscope, which has equal reflectivity for S and P-polarized light and selects exclusively the 400 nm reflected radiation. The two polarizers (P1 and P2) and the phase mask are mounted on a rotating shaft coupled to an optical rotary encoder. After the dichroic mirrors, the second harmonic radiation is focused by a final lens (L4) onto a 400 nm

bandpass filter and photomultiplier tube. The signal from the photomultiplier tube is sent to a lock-in amplifier synced to the 5 kHz pulsed laser reference signal and the amplified signal is then correlated with the signal from the optical rotary encoder using a home-built oscilloscope.

Importantly, the geometrical constraints introduced by the rotating plane of incidence mean that rotating P1 and P2 between S and P configurations electromechanically is challenging, as power must be transmitted from the stationary laboratory frame to electrical components lying in the rotating frame.

To solve this problem, we utilize a hollow-bore electrical slip ring and a miniature stepper motor, shown in an exploded-view diagram in Fig. 4.3(a). A slip ring uses stationary conductive brushes sliding against a rotating through-bore cylinder to transfer power from a stationary reference frame to a rotating one, as shown in Fig. 4.3(b) [3]. To accommodate the further requirement that the beams pass through the entire device unimpeded, we employ an 8 mm stepper motor that fits in between the two beams. Fig. 4.3(c) and Fig. 4.3(d) show a front view of the device, with the wire grid polarizer in the P and S positions, respectively, and the polarization direction of the polarizer shown in arrows on the edge of the polarizer. A full rendering, to scale, of the automated system within the full setup is shown in Fig. 4.4.

4.4.1 Slip Ring

Slip rings are a standard electromechanical device for transferring power from a stationary assembly to a rotating assembly. An inner, rotating part of the slip ring can freely rotate relative to an outer, stationary part without compromising signal or power transmission. This functionality is enabled by low-friction metal brushes that slide against another set of electrical contacts, allowing free rotation while maintaining good electrical conductivity [3], as shown in Fig. 4.3(b). To allow for the uninterrupted passage of the beams through the device, we use a hollow-bore slip ring (Moflon MT3899-S040-VD) whose 38 mm inner bore rotates along with the lens tube-pulley assembly shown in Fig. 4.4. Either set screws located on the front side of the slip ring (as shown in Fig. 4.3) or a 3D-printed cylindrical hollow bore adapter (not shown) can secure the inner bore of the slip ring to the lens tube.

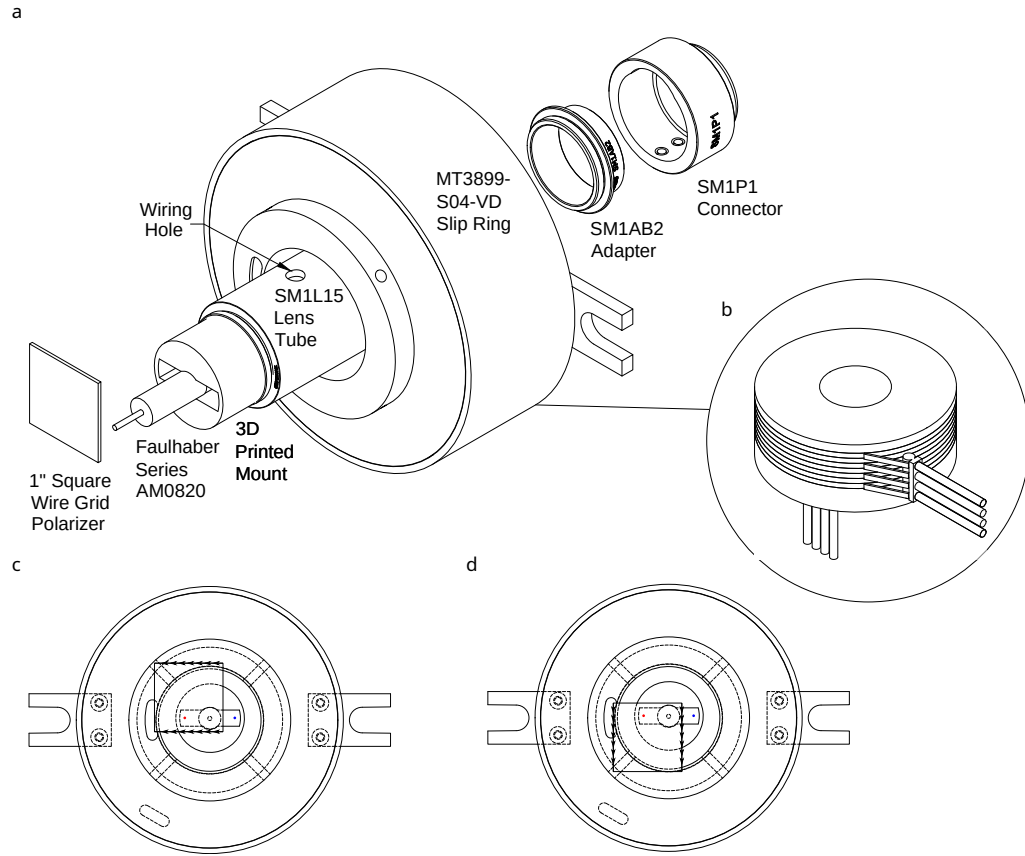


Figure 4.3: (a) An exploded-view diagram of one of the automated polarization rotators, with the individual components labeled. Each of these is a manufactured part except for the 3D-printed mount. (b) A schematic of the interior of an electrical slip ring, where low-friction metal brushes allow for electrical conduction across a rotating assembly. (c) A front view of the device, in the P-polarized state, with arrows on the edge of the polarizer indicating the polarization direction. (d) Same as Fig. 4.3(c), but in the S-polarized state.

4.4.2 Miniature Stepper Motor

The hollow bore slip ring allows for the transfer of power to the rotating shaft. To rotate the wire grid polarizer between S and P configurations while also allowing both beams to pass through the entire device, we use an 8 mm diameter Faulhaber Series AM0820 stepper motor. The stepper motor's shaft is epoxied to a 1 inch square wire-grid polarizer roughly 5 mm from the closest horizontal and vertical edges, as shown in Fig. 4.3(c) and Fig. 4.3(d). The stepper motor is mounted in the center of the SM1L15 lens tube using a custom, 3D printed mount as shown in Fig. 4.3(a). This mount, along with careful epoxying of the polarizer to the motor shaft, ensures that the incidence angle of the beam is close to normal. Furthermore, the mount ensures that the stepper motor's shaft is aligned closely to the central rotation axis of the entire assembly, minimizing torques on the motor and polarizer. This stepper motor can support up to 800 total micro-steps per revolution (0.45° per micro-step) and 0.65 mNm of holding torque, and is small enough to fit in between the incoming and outgoing beams.

The motor can then move the polarizer between the P configuration (Fig. 4.3(c)) and the S configuration (Fig. 4.3(d)) without manual intervention or the need to stop the rotation of the entire assembly. The offset placement of the polarizer on the motor shaft allows only one of the beams (either incoming or outgoing) to pass through the polarizer. The SM1AB2 and SM1P1 adapter pieces allow for arbitrary rotation relative to the longer lens tube-pulley assembly, allowing the beams to be aligned with the empty spaces in the stepper motor mount. These adapter pieces also allow for small ($\pm 20^\circ$) rotations of the polarizer about the central axis to account for factory defects which may cause the polarization axis to be misaligned with the straight edges of the polarizer.

Another copy of the same system shown in Fig. 4.3 is mounted on the other side of the lens tube-pulley assembly and controls the polarization of the reflected beam, as shown in Fig. 4.4. The back sides of both devices, shown in Fig. 4.4, are attached to the rotating lens tube-pulley-motor-shaft assembly shown in Fig. 4.4 via threads on the long central lens tube. A hole drilled in the top and bottom of the SM1L15 piece in each device shown in figure Fig. 4.3(a) allows feedthrough wires to connect the four leads of the stepper motor to the four rotating inner-bore slip ring leads. The four leads on the stationary side of each slip ring directly connect to

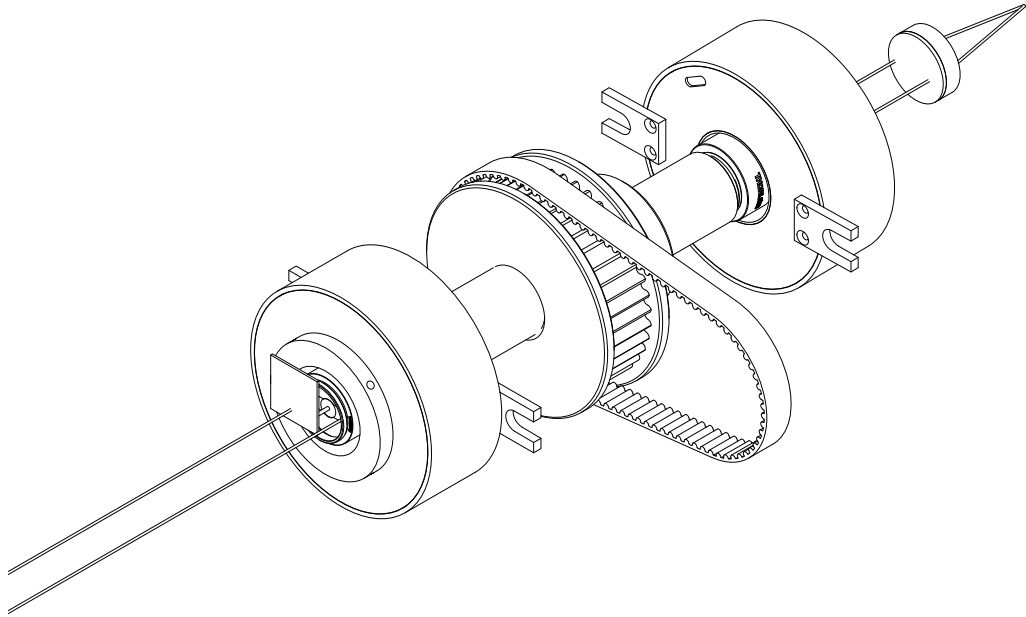


Figure 4.4: A 3-dimensional rendering of the boxed-in part of the setup in Fig. 4.2, with fully automated polarization rotators.

a Geckodrive G250X digital step driver for each device, controlled by a single Arduino Nano Every. This control circuit allows for the integration of the stepper motors with existing instrumentation software.

Whenever the stepper motors lose power, the polarizers need to be re-aligned due to the loss of their holding torque. The alignment is performed by using a reference polarizer with a known polarization axis. First, the plane of incidence of the entire assembly is positioned to the known polarization plane of the reference polarizer, then the polarizers themselves can be oriented by placing the beam through the reference polarizer and rotating the stepper motor until beam extinction (yielding an S-polarized alignment). The polarizers can then freely rotate between this S-polarized position and the orthogonal P-polarized position.

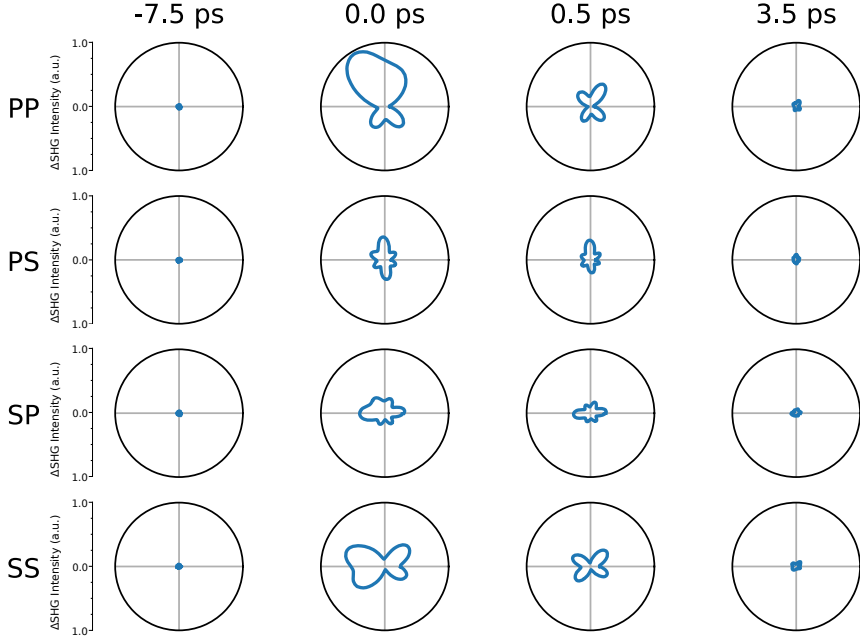


Figure 4.5: A polar plot of the change in SHG intensity (from the pre-pump state) as a function of time since zero-delay for the test sample GaAs. This is a demonstration of using the automated polarization rotators to take tr-SHG data. 55 different pump-probe delays (only four time delays are plotted) were taken in this dataset, meaning that 220 polarization rotations were performed using the automated polarizers.

4.5 Validation and Discussion

To test these automated polarization rotators, we performed time-resolved RA-SHG on the non-centrosymmetric semiconductor GaAs [24, 99]. A pump line was added to the setup shown in Fig. 4.2 by mounting a 45° mirror onto L3 so that the pump beam may be reflected directly onto the sample. The pump pulse is produced by an optical parametric amplifier (Spectra-Physics Topas) tuned to a wavelength of $1.3 \mu\text{m}$. The pump line

includes a delay stage, which controls the relative time delay between the pump and the probe pulses, and a chopper wheel, which reduces the effective repetition rate of the pump pulses to 2.5 kHz. With the pump repetition rate of 2.5 kHz and the probe repetition rate of 5 kHz, locking in at a frequency of 2.5 kHz produces a signal proportional to the change in the SHG intensity relative to equilibrium. For time-resolved measurements on GaAs, shown in Fig. 4.5, 55 different pump-probe delays were taken, resulting in 220 different automatic rotations of the polarizers. The data in Fig. 4.5 shows the change in the SHG intensity relative to equilibrium as a function of the pump-probe delay, for each of the polarization channels. The use of the polarization rotators in this validation measurement demonstrates their functionality and broad utility for multi-axis RA-SHG measurements.

This system was also used to expedite data collection in recent studies of time-resolved, temperature-dependent RA-SHG [28]. This particular type of RA-SHG measurement demonstrates the general advantages of automated polarization control in multi-axis RA-SHG measurements. To see this, note that if the rotation of the polarizers is performed manually, the best data-taking strategy involves taking the time dependence of one polarization channel in full before moving to the next. However, in the presence of low-frequency noise (due to e.g. fluctuations in the laser intensity), this is problematic as the different polarization channels will not be taken under equivalent conditions. In the automated case, in contrast, all polarization channels can be taken at each time delay. This greatly decreases the experiment's susceptibility to low-frequency noise and expedites data taking by allowing for overnight and multi-day scans.

Automated polarization rotation thus vastly improves RA-SHG data collection, eliminating the need for manual polarization rotation, especially in cases of multiple experimental axes. The roughly 1.000 \$ total cost of both devices (not including polarizers) makes them relatively inexpensive, and the design is easily implementable in existing RA-SHG setups. Multi-axis measurements are becoming increasingly important to resolve complicated phase diagrams and competing orders, and thus future measurements will increasingly rely on automated systems such as the one presented in this work.

Chapter Five

Second harmonic generation as a probe of broken mirror symmetry in 1T-TaS₂

5.1 Preface

This chapter is based on a manuscript that was published as a Rapid Communication in *Physical Review B* in 2020, again modified to fit the format of this thesis. It was coauthored by myself, Anshul Kogar, Linda Ye, Bilal Gökce, Alfred Zong, Joseph G. Checkelsky, and Nuh Gedik. Anshul Kogar and I initiated the project and took the RA-SHG data. Linda Ye and Joseph G. Checkelsky grew the samples, Bilal Gökce helped build the RA-SHG setup, and Alfred Zong took some electron diffraction data. I analyzed the data and wrote the paper. Nuh Gedik supervised the project.

5.2 Abstract

The notion of spontaneous symmetry breaking has been used to describe phase transitions in a variety of physical systems. In crystalline solids, the breaking of certain symmetries, such as mirror symmetry, is difficult to detect unambiguously. Using 1T-TaS₂, we demonstrate here that RA-SHG is not only a sensitive technique for the detection of broken mirror symmetry, but also that it can differentiate between mirror symmetry-broken structures of opposite planar chirality. We also show that our

analysis is applicable to a wide class of different materials with mirror symmetry-breaking transitions. Lastly, we find evidence for bulk mirror symmetry-breaking in the incommensurate charge density wave phase of 1T-TaS₂. Our results pave the way for RA-SHG to probe candidate materials where broken mirror symmetry may play a pivotal role.

5.3 Introduction

In condensed matter systems, phases are often classified by the symmetries that they break. Identifying these symmetries enables one to understand a system's order parameter, collective excitations, topological defects, and allowable topological indices [87, 97]. Together, these attributes allow one to predict how a material will respond to external perturbations like electromagnetic fields, heat, and mechanical forces, which is a central goal of condensed matter physics.

Specifically, the presence or absence of mirror symmetry can lead to a variety of unusual phases and properties. For example, the absence of mirror plane symmetry in noncentrosymmetric materials can give rise to gyrotropic order, which can lead to a nonzero out-of-plane circular photovoltaic effect [8]. Moreover, in certain topological crystalline insulators, such as SnTe, the presence of mirror symmetry can give rise to conducting surface states through the existence of a nonzero mirror Chern number. This topological index guarantees an even number of Dirac cones on surfaces where mirror symmetry is retained [33, 43, 96].

In other circumstances, like that in the pseudogap regime of cuprate superconductors, the existence of mirror symmetry is more controversial and has led some to seek an experimental method to serve as a binary indicator of broken mirror symmetry [41]. In principle, several tools can already do this, including resonant ultrasound spectroscopy [55, 66], X-ray, neutron, and electron diffraction [4, 23], and a recently-proposed method, shear conductivity [41]. Resonant ultrasound spectroscopy and the diffraction-based techniques are more sensitive to the ionic lattice, which makes the identification of subtle electronic symmetry-breaking challenging. And while shear conductivity has the potential to be an extremely versatile tool for identifying broken point group symmetries, experimental pursuits are currently only preliminary [41]. In this study, we focus on a nonlinear optical technique, RA-SHG, which we show is

capable not only of identifying broken mirror symmetry [39] but also of resolving its sense (left- or right-handed). Furthermore, RA-SHG is sensitive to the electronic subsystem and can be used for microscopy studies, making it an ideal experimental tool for probing phase transitions where domains may arise [38, 52].

In this direction, we choose a material, 1T-TaS₂, in which vertical mirror plane symmetry is manifestly broken across an incommensurate (IC) to nearly commensurate (NC) CDW transition [107, 113]. Using this material, we demonstrate in this Rapid Communication that RA-SHG is an effective probe of broken mirror symmetry. We also show that the sense (i.e. left- or right-handed) associated with the mirror symmetry-broken structure is encoded in the angular dependence of the RA-SHG signal. Thus, RA-SHG can be used to differentiate mirror-opposite domains. While the data presented in this work is specific to the case of 1T-TaS₂, we also show analytically that our technique is applicable to a wide class of transitions involving spontaneously broken mirror symmetry.

1T-TaS₂ is a layered material with a crystallographic structure identical to other octahedrally-coordinated transition metal dichalcogenides (Fig. 5.1(a)). The space group of the high temperature, undistorted phase is $P\bar{3}m1$ (no.164, point group D_{3d}) [92], and the point group of the surface normal to the (001) direction in this phase is C_{3v} [34, 86]. Upon lowering temperature, 1T-TaS₂ undergoes a series of CDW transitions. At $T_{IC} = 550$ K, a triple- q IC CDW forms which breaks translational symmetry but retains the surface point group symmetries of the undistorted phase [34, 86]. The effects of the CDW on the bulk symmetries in this phase are not yet understood. On further cooling, at $T_{IC-NC} = 353$ K there is a weak first-order transition to an NC CDW phase where three vertical mirror plane symmetries are broken [92] and the surface point group becomes C_3 . The NC phase has been visualized with scanning tunneling microscopy and exhibits patches of commensurate “Star of David” hexagrams that are separated by a network of discommensurations [109]. Because mirror symmetry is broken, there are two energetically equivalent CDW configurations (α and β) in the NC phase that have opposite planar chirality (Figs. 5.1(c)–d)). At even lower temperatures, $T_{NC-C} = 184$ K, 1T-TaS₂ undergoes a symmetry-preserving first-order transition, where the discommensurations disappear and the CDW locks into a structure commensurate with the underlying lattice [44].

Recent interest in the NC phase of 1T-TaS₂ has arisen due to the possi-

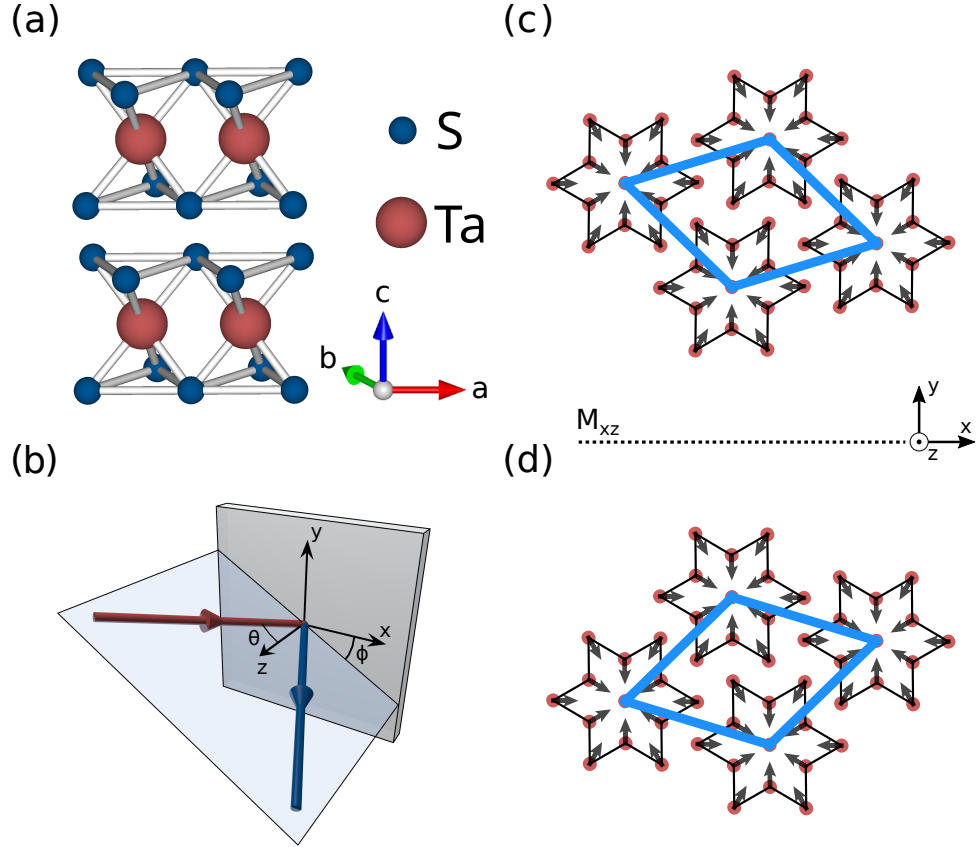


Figure 5.1: (a) Structure of 1T-TaS₂ in the undistorted phase. Ta and S atoms are depicted in red and blue, respectively. (b) Schematic of the experimental geometry. (c) (d) Structure of the CDW in the NC phase. Arrows denote the movement of the Ta atoms (red) below $T_{\text{IC-NC}} = 353$ K from their undistorted positions. The transition at $T_{\text{IC-NC}}$ spontaneously breaks mirror symmetry, so that two different CDW configurations (α and β) can form which have opposite planar chirality. The new unit cells of the two configurations are depicted in blue. M_{xz} denotes one vertical mirror plane which is broken beneath $T_{\text{IC-NC}}$. The others are related to M_{xz} by $\pm 120^\circ$ rotation about the z axis.

bility of injecting mirror-opposite domains into the CDW structure [113] which do not otherwise develop during the IC-NC transition. Zong *et al.* were able to induce these domains using a single ultrafast pulse of light, which was found to drive the material into a long-lived metastable state possessing domains of opposite planar chirality. Partly motivated by the desire to image these domains, we seek here a simple experimental method that could identify domains with opposite planar chirality.

5.4 Results and discussion

1T-TaS₂ samples used in the experiment were grown using the chemical vapor transport technique, as described in Ref. [113]. We verified that the NC phase of 1T-TaS₂ was single-domain by performing electron diffraction on a sample from the same batch (see section 5.7). This is in agreement with previous works [12, 36, 107, 113].

In RA-SHG [37, 59, 60, 98], a pulsed laser beam of frequency ω and amplitude $E(\omega)$ is focused onto a sample with nonzero angle of incidence θ (Fig. 5.1(b)). The 2ω component of the radiation emitted by the sample is subsequently measured in various combinations of incoming and outgoing polarizations (either parallel (P) or perpendicular (S) to the plane of incidence) and as a function of the angle ϕ between the plane of incidence and some crystallographic axis. In noncentrosymmetric materials, the response is dominated by the bulk electric dipole moment $P_i(2\omega) = \chi_{ijk}E_j(\omega)E_k(\omega)$ [13], where χ_{ijk} is a material-specific susceptibility tensor which must be invariant under all symmetry operations present in the crystallographic point group. In centrosymmetric crystals such as 1T-TaS₂, the bulk electric dipole response is forbidden [13, 81]. In this case, the dominant response often comes from the surface of the sample, which necessarily breaks inversion symmetry [11]. SHG from surfaces of materials is described by a different susceptibility tensor, χ_{ijk}^S , which is constrained by the crystal symmetries of the surface. In addition, there can be bulk contributions from higher-order processes which are allowed in the presence of inversion symmetry, such as the bulk quadrupole response $Q_{ij}(2\omega) = \chi_{ijkl}^Q E_k(\omega)E_l(\omega)$ [52, 90]. Our experimental implementation uses a fast-rotation setup similar to that described in Harter *et al.* [37] and Torchinsky *et al.* [99]. Here, we use an 800 nm (1.55 eV) laser beam incident at 10° with respect to the (001) sample normal. Further

experimental details can be found in the supplement (see section 5.7).

To show that we are sensitive to the breaking of mirror symmetry across the IC to NC transition, we took RA-SHG data on 1T-TaS₂ in both phases. Figs. 5.2(a) and 5.2(b) show the second harmonic response from the sample above and below $T_{\text{IC-NC}} = 353$ K in two polarization channels, plotted as a function of ϕ . We are able to fit the rotational anisotropy in the IC phase using the surface point group C_{3v} (Fig. 5.2(a)), which is in agreement with previous reports [34, 86]. It should be noted that in order to fit the S_{in}-S_{out} polarization channel appropriately, we find that it is necessary to add an additional bulk quadrupole contribution to the signal. The consequences of this contribution will be discussed later, but at the moment they do not affect our conclusions.

Upon cooling into the NC phase, mirror symmetry is spontaneously broken and the surface point group reduces to C_3 [92]. As a result, the RA-SHG exhibits a marked lowering of symmetry (Fig. 5.2(b)). This lowering of symmetry can be understood by noting that the ϕ dependence of $I_{\text{PS}}(2\omega)$ under C_3 is given by (see section 5.7)

$$I_{\text{PS}}(2\omega) = (A_0 + A_1 \cos(3\phi) + A_2 \sin(3\phi))^2, \quad (5.1)$$

where A_0 , A_1 , and A_2 are functions of the susceptibility elements χ_{ijk}^S .

Symmetry considerations (see section 5.7) show that A_0 and A_1 vanish identically in the presence of mirror symmetry. The absence of these terms lead to the six-fold symmetry in the P_{in}-S_{out} channel and its alignment with the crystallographic axes as seen in Fig. 5.2(a). However, these terms can adopt nonzero values when mirror symmetry is broken. Below $T_{\text{IC-NC}}$, the RA-SHG intensity therefore exhibits a three-fold rather than six-fold symmetric pattern, arising from a nonzero A_0 . The effect of a nonzero A_1 is to rotate the RA-SHG intensity away from the high-symmetry axes, but we observe this coefficient to be zero within the resolution of our instrument. A negligible rotation of the SHG pattern should be expected, as the atomic positions of the Ta atoms only contract towards a central Ta atom and do not rotate away from their high symmetry axes to break the mirror symmetry (see Figs. 5.1(c)-d)).

The three-fold nature of the RA-SHG intensity can be quantified experimentally by performing a spectral (sine) decomposition of the intensity and extracting the third Fourier coefficient, $\mathcal{I}_{PS}^{(3)}$, of $I_{\text{PS}}(2\omega)$ (see section 5.7). Fig. 5.2(c) shows that $\mathcal{I}_{PS}^{(3)}$ appears discontinuously below

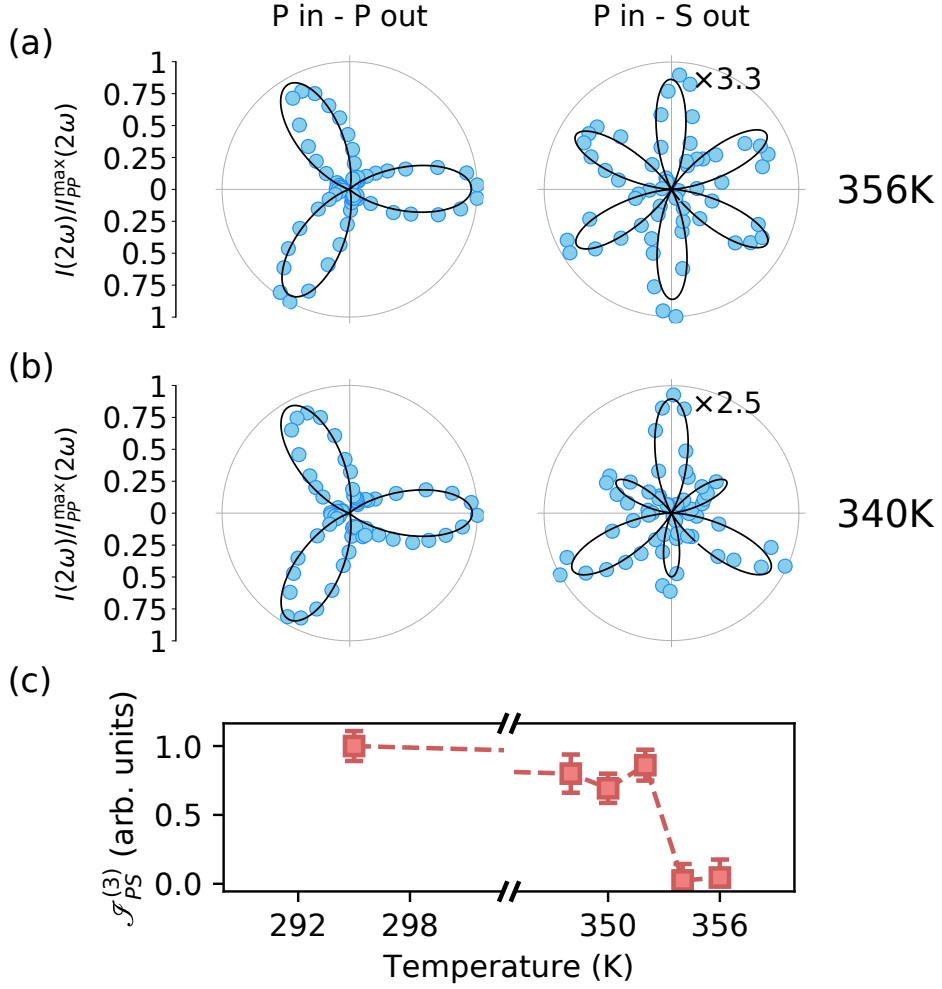


Figure 5.2: (a) (b) Second harmonic intensity from 1T-TaS₂ as a function of ϕ above (Fig. 5.2(a)) and below (Fig. 5.2(b)) $T_{\text{IC-NC}} = 353\text{K}$. For clarity, only two polarization channels are shown; the others are reproduced in the supplement (see section 5.7). Solid lines in Fig. 5.2(a) and Fig. 5.2(b) are best fits to the data using the surface point groups C_{3v} and C_3 , respectively. Data is normalized to the maximum value of the P_{in}-P_{out} signal for each temperature. (c) Temperature dependence of the third Fourier coefficient, $\mathcal{I}_{PS}^{(3)}$, of the intensity (see main text and section 5.7 for details).

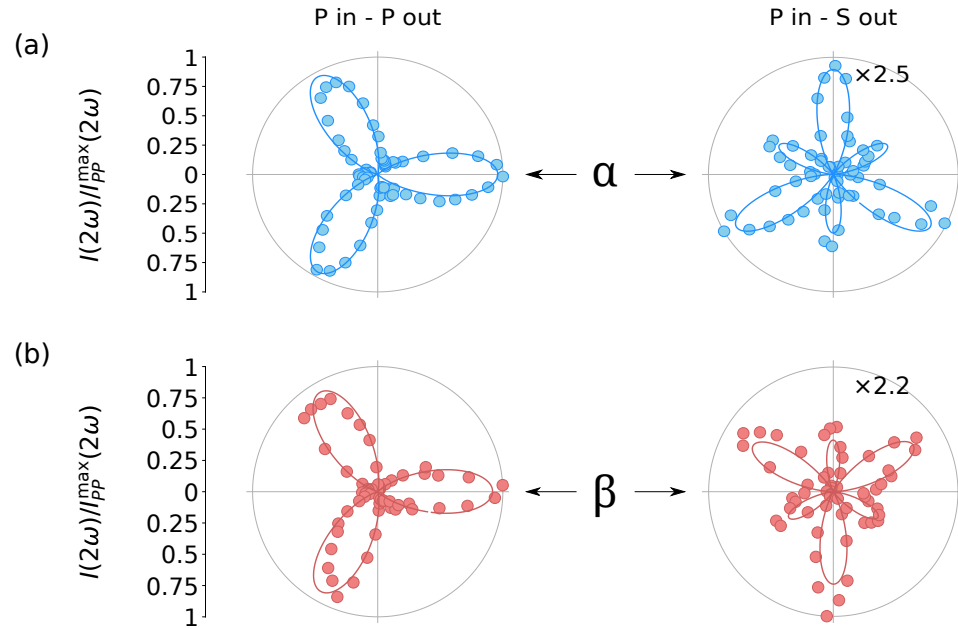


Figure 5.3: Second harmonic intensity as a function of ϕ from mirror-opposite samples of 1T-TaS₂ in the NC phase ($T = 340$ K). The labels α and β refer to the two degenerate mirror-image configurations which are allowed in the NC phase. The solid line in (a) is a fit to the data using the surface point group C_3 . The fit in (b) was generated by performing a mirror operation (see section 5.7) to the numerical susceptibility tensor obtained from 5.3(a). Data is normalized to the maximum value in the P_{in} - P_{out} polarization channel for each sample.

$T_{\text{IC-NC}}$, consistent with the first-order nature of the phase transition. Taken together, the above considerations confirm that $\mathcal{I}_{PS}^{(3)}$ is a binary indicator of broken mirror symmetry in 1T-TaS₂.

Having established that RA-SHG is sensitive to the breaking of vertical mirror plane symmetry in 1T-TaS₂, we now seek to demonstrate that it can differentiate between CDW configurations of opposite planar chirality in the NC phase. To do so, we generate two samples with opposite planar chirality by cleaving a single sample of 1T-TaS₂. We then perform RA-SHG on both sides of the same cleave. Referring to Figs. 5.1(c) and 5.1(d), cleaving the sample is equivalent to performing a 180° rotation about the x -axis, which in a single layer is equivalent to a mirror reflection about M_{xz} .

Fig. 5.3 shows the results of RA-SHG measurements in the P_{in}-P_{out} and P_{in}-S_{out} polarization channels as functions of ϕ , where the two mirror images are labeled α and β . As shown in the figure, whether the CDW configuration was α or β is indicated in RA-SHG by the orientation (up or down) of the pattern in the P_{in}-S_{out} channel, which is determined by the sign of A_0 in Eq. 5.1 (see section 5.7). This feature constitutes an experimental observable capable of identifying the sense associated with broken mirror symmetry in 1T-TaS₂.

To validate the analysis contained above, we first fit the data for the α structure using the surface point group C_3 to generate a tensor χ_{ijk}^{α} with numerical coefficients. The fit is shown in Fig. 5.3(a). Then, we transform χ_{ijk}^{α} by a mirror reflection about M_{xz} to generate χ_{ijk}^{β} (see section 5.7); with this transformation, we find that the rotational anisotropy simulated using χ_{ijk}^{β} collapses onto the measured signal, as shown in Fig. 5.3(b).

While the data contained in this work is specific to 1T-TaS₂, the analysis is applicable to a variety of different phase transitions involving broken mirror symmetry. By understanding which Fourier coefficients of the SHG intensity adopt nonzero values in the low-symmetry phase, one can show that almost every structural phase transition involving broken mirror symmetry implies a measurable change in the symmetry of the SHG pattern (i.e. beyond a simple change in overall intensity). We have performed a symmetry analysis of all possible phase transitions involving spontaneously broken mirror symmetry and in each case identified the relevant experimental indicator(s). The results of this analysis can be found in the supplement (see section 5.7).

The final observation of this work concerns the contribution from the bulk of the sample to the measured RA-SHG signal. As mentioned above, we find that in order to fit the data in the S_{in}-S_{out} polarization channel correctly, we need to introduce an additional bulk quadrupole contribution to the SHG signal. This contribution, which is described by the effective polarization $\nabla_j Q_{ij} = 2i\chi_{ijkl}^Q k_j E_k E_l$, is the next-lowest order contribution to SHG and is allowed in the presence of inversion symmetry [52, 90]. Importantly, the quadrupole contribution is generated by the entire illumination volume and is therefore insensitive to the surface symmetry. Quadrupole SHG can be identified by examining the θ dependence of the SHG intensity in the S_{in}-S_{out} channel. For purely electric dipole SHG, the symmetry in this channel does not depend on the incident angle. The θ dependence depicted in Figs. 5.4(a) and 5.4(b) therefore establishes the presence of a quadrupole contribution in our signal.

According to diffraction measurements [34], the correct surface and bulk point groups in the NC phase are C_3 and S_6 , respectively. Fig. 5.4(a) shows our results in this phase, which are consistent with this assignment. To understand the three-fold symmetry in Fig. 5.4(a), we note that the ϕ dependence of $I_{SS}(2\omega)$ in this symmetry assignment is given by (see section 5.7)

$$I_{SS}(2\omega) = (B_0 + B_1 \cos(3\phi) + B_2 \sin(3\phi))^2, \quad (5.2)$$

where B_1 and B_2 are functions of the susceptibility elements χ_{ijk}^S and χ_{ijkl}^Q , but B_0 depends on χ_{ijkl}^Q only (and is zero when the quadrupole contribution is ignored). B_0 is then a probe of the bulk structure only and is not affected by the surface symmetry. When mirror symmetry is broken, all three coefficients are allowed and the function is three-fold symmetric as in Fig. 5.4(a).

However, symmetry considerations (see section 5.7) show that B_0 is zero in the presence of mirror symmetry. If bulk mirror symmetry were fully restored in the IC phase, we would therefore expect the signal to be six-fold symmetric. Fig. 5.4(c) shows that the RA-SHG instead remains three-fold symmetric in this phase, suggesting that the bulk breaks mirror symmetry. On the other hand, the highest-symmetry surface point group consistent with Figs. 5.2(a) and 5.4(c) is C_{3v} , which retains mirror symmetry. With RA-SHG, it is not possible to deduce the full crystal structure, but we speculate that this discrepancy between surface

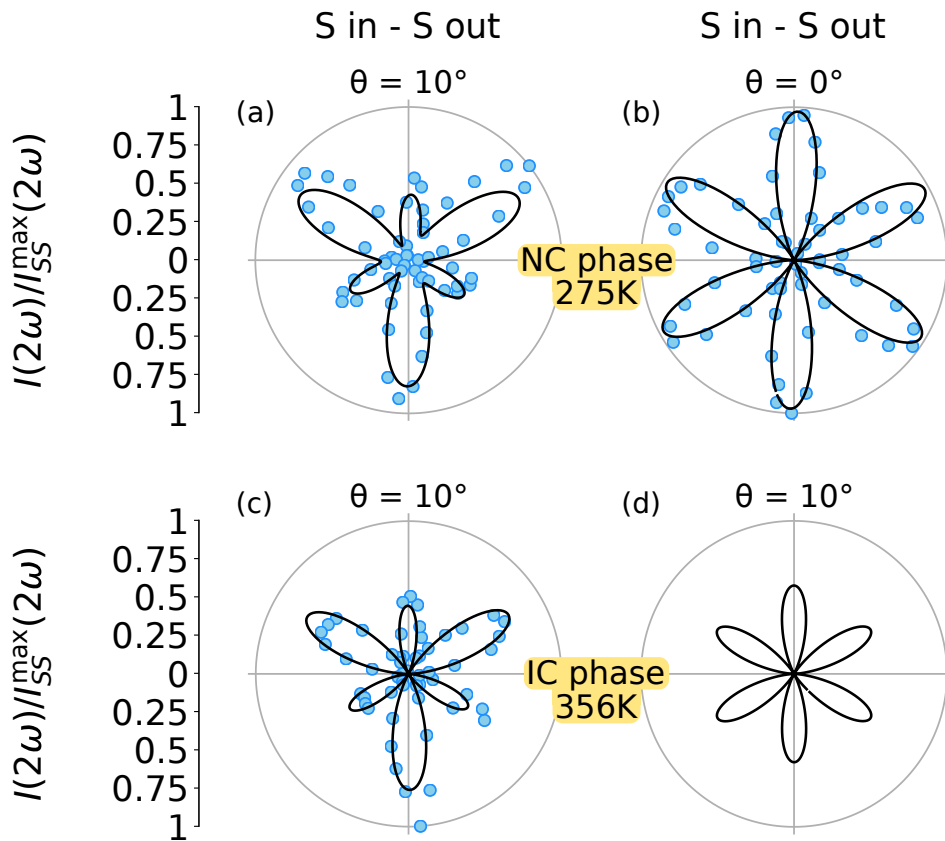


Figure 5.4: Second harmonic intensity as a function of ϕ in the $S_{in}-S_{out}$ polarization channel. Temperatures, phases and incident angles (θ) are indicated on the figure. Also shown are fitting curves using the point group assignments (a) C_3 surface and S_6 bulk, (b) C_3 surface and S_6 bulk, (c) C_{3v} surface and S_6 bulk. (d) Best fit to data in 5.4(c) using C_{3v} surface and D_{3d} bulk. Data in all plots was normalized to one for clarity. Other polarization channels are depicted in the supplement (see section 5.7).

and bulk symmetries might be attributable to the particular stacking arrangement associated with the CDW above $T_{\text{IC-NC}}$ (see section 5.7). This would explain why the surface component, which is measuring the local structure at the surface of the sample [11], is consistent with the existence of mirror symmetry, whereas the bulk component, which measures the global structure of many layers, is not.

5.5 Conclusion

In summary, we have demonstrated here that RA-SHG can be used to identify broken mirror symmetry in crystalline materials. In addition, we have found that RA-SHG can differentiate between structural configurations related by mirror reflection. By considering the different symmetry constraints on the $S_{\text{in}}-S_{\text{out}}$ channel, we have also shown that RA-SHG is sensitive to broken mirror symmetry in the bulk of 1T-TaS₂, and have found evidence that the IC phase of this material breaks mirror symmetry in the bulk. Importantly, our analysis is generalizable beyond the specific case of 1T-TaS₂, and therefore opens up the possibility for RA-SHG to detect mirror symmetry-broken phases and their domain structures in other candidate materials.

5.6 Acknowledgments

We would like to thank Adrian Po and Liang Fu for helpful discussions regarding this work. This work was supported by the Gordon and Betty Moore Foundation’s EPiQS Initiative Grant GBMF4540 to NG (data analysis and manuscript writing) and Grant GBMF3848 to JGC (instrumentation), Shell through the MIT Energy Initiative (experimental setup and material development) and through DARPA DSO under DRINQS program grant number D18AC00014 (sample growth and data taking). L.Y. acknowledges support by the STC Center for Integrated Quantum Materials, NSF Grant No. DMR-1231319 and by the Tsinghua Education Foundation. B.G. gratefully acknowledges the German Academic Exchange Service (DAAD) for supporting his research stay with a fellowship.

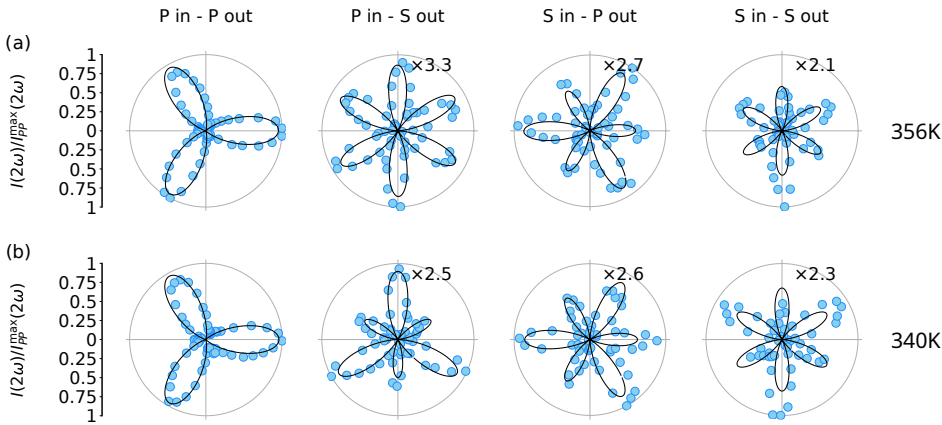


Figure 5.5: RA-SHG intensity as a function of ϕ above (a) and below (b) $T_{IC-NC} = 353K$. Solid lines are best fits to the data using electric dipole SHG in the surface point groups C_{3v} and C_3 , respectively. Data is normalized to the maximum value of the $P_{in}-P_{out}$ signal for each temperature.

5.7 Supplemental material

5.7.1 Probing broken mirror symmetry with RA-SHG

Complete RA-SHG data

In the first section of the main text, we discuss how RA-SHG is sensitive to the breaking of mirror symmetry in 1T-TaS₂. In Fig. 5.2 and Fig. 5.2(b) of the main text, we display RA-SHG data in two polarization channels: $P_{in}-P_{out}$ and $P_{in}-S_{out}$. For completeness, the other polarization channels are reproduced in Fig. 5.5. Importantly, the fits in the figure only include a surface electric dipole contribution (see main text). The inability to fit the $S_{in}-S_{out}$ polarization channel with a pure electric dipole contribution suggested to us that a second contribution was necessary in the form of a bulk electric quadrupole term. This is discussed in the main text as well as in section 5.7.5.

$\mathcal{I}_{PS}^{(3)}$ as an indicator of broken mirror symmetry

In the main text, we used the relation given by Eq. 5.1 to show that the breaking of sixfold symmetry in the P_{in}-S_{out} channel is consistent with the lowering of the surface point group from C_{3v} to C₃ during the IC to NC phase transition. In this section, we show how Eq. 5.1 is derived.

Given any crystallographic point group, it is always possible to compute the form of the susceptibility tensor χ_{ijk}^S . In C₃, the susceptibility tensor is given by [13]

$$\chi_{ijk}^S = \begin{pmatrix} a & -b & c \\ -b & -a & -d \\ c & -d & 0 \\ \hline -b & -a & d \\ -a & b & c \\ d & c & 0 \\ \hline e & 0 & 0 \\ 0 & e & 0 \\ 0 & 0 & f \end{pmatrix}_{ijk} \quad (5.3)$$

for some a, b, c, d, e , and f which are dependent on the material. Here, the threefold axis is taken to be along the z direction. In the point group C_{3v}, the susceptibility tensor is constrained by symmetry so as to take a form which is the same as Eq. 5.3, but with $b = d = 0$, i.e.

$$\chi_{ijk}^S = \begin{pmatrix} a & 0 & c \\ 0 & -a & 0 \\ c & 0 & 0 \\ \hline 0 & -a & 0 \\ -a & 0 & c \\ 0 & c & 0 \\ \hline e & 0 & 0 \\ 0 & e & 0 \\ 0 & 0 & f \end{pmatrix}_{ijk} . \quad (5.4)$$

Here, the mirror planes are taken to be the xz -plane and those related to it by rotation about the z -axis through $\pm 120^\circ$.

To compute the RA-SHG intensity in the P_{in}-S_{out} channel, we consider a frame of reference in which the plane of incidence is held fixed and the

sample is rotated about the optical axis. This reference frame is equivalent to that of the experimental setup (where the sample is fixed and the plane of incidence rotates), but it is easier to visualize and formulate mathematically. In this frame, the incoming P -polarized light at frequency ω is parallel to the vector $E_i(\omega) = (-\cos \theta, 0, \sin \theta)_i^T$, and the outgoing S -polarized light which we wish to compute is parallel to the y -axis. The RA-SHG intensity in this channel is therefore given by

$$I_{PS}^{2\omega}(\phi) \propto |P_y^{2\omega}(\phi)|^2 \propto |\bar{\chi}_{ijk}^S(-\phi)E_j(\omega)E_k(\omega)|^2, \quad (5.5)$$

where $\bar{\chi}_{ijk}^S(\phi)$ is the susceptibility tensor corresponding to the sample when it has been rotated by an angle ϕ . The relative sign in the argument of $\bar{\chi}_{ijk}^S$ is due to the different reference frame used here compared to Fig. 5.1(b), where ϕ is defined.

With the rotation matrix

$$R(\phi)_{ij} = \begin{pmatrix} \cos \phi & -\sin \phi & 0 \\ \sin \phi & \cos \phi & 0 \\ 0 & 0 & 1 \end{pmatrix}_{ij}, \quad (5.6)$$

$\bar{\chi}_{ijk}^S(\phi)$ is given by

$$\bar{\chi}_{ijk}^S(\phi) = R(\phi)_{il}R(\phi)_{jm}R(\phi)_{kn}\chi_{lmn}^S. \quad (5.7)$$

Substituting Eq. 5.7 into Eq. 5.5, we then have

$$I_{PS}^{2\omega}(\phi) \propto |R(-\phi)_{yl}R(-\phi)_{jm}R(-\phi)_{kn}\chi_{lmn}^S E_j(\omega)E_k(\omega)|^2. \quad (5.8)$$

With Eq. 5.3 as χ_{ijk}^S , we arrive at Eq. 5.1 in the main text,

$$I_{PS}(2\omega) \propto (A_0 + A_1 \cos(3\phi) + A_2 \sin(3\phi))^2, \quad (5.9)$$

where

$$A_0 = 2d \sin(\theta) \cos(\theta), \quad (5.10)$$

$$A_1 = -b \cos^2(\theta), \quad (5.11)$$

and

$$A_2 = a \cos^2(\theta). \quad (5.12)$$

Since $b = d = 0$ in C_{3v} , these equations show that A_0 and A_1 are zero in the presence of mirror symmetry, as cited in the main text. Furthermore, in C_{3v} , Eq. 5.9 reduces to

$$I_{\text{PS}}(2\omega) \propto A_2^2 \sin^2(3\phi), \quad (5.13)$$

which possesses sixfold rotational symmetry.

In the main text, we also remark that the breaking of sixfold rotational symmetry across the IC to NC phase transition can be quantified experimentally by performing a spectral (sine) decomposition of the measured intensity ($I_{\text{PS}}^{2\omega}(\phi)$) and extracting the third Fourier coefficient, which we called $\mathcal{I}_{\text{PS}}^{(3)}$. Here, we define $\mathcal{I}_{\text{PS}}^{(3)}$ explicitly and show that it is present in 1T-TaS₂ only when mirror symmetry is broken.

The spectral decomposition for any given polarization channel (Γ_{in} - Γ_{out}) is defined formally by writing

$$I_{\Gamma_{\text{in}}\Gamma_{\text{out}}}^{2\omega}(\phi) = \sum_{n=0}^{\infty} \mathcal{I}_{\Gamma_{\text{in}}\Gamma_{\text{out}}}^{(n)} \sin \left[n\phi + \psi_{\Gamma_{\text{in}}\Gamma_{\text{out}}}^{(n)} \right]. \quad (5.14)$$

This equation defines $\mathcal{I}_{\Gamma_{\text{in}}\Gamma_{\text{out}}}^{(n)}$ and $\psi_{\Gamma_{\text{in}}\Gamma_{\text{out}}}^{(n)}$ as the amplitude and phase of the n -fold Fourier component of the corresponding SHG intensity.

Using Eqs. 5.3, 5.8 and 5.14, we can then compute $\mathcal{I}_{\text{PS}}^{(3)}$ and $\psi_{\text{PS}}^{(3)}$ in the low temperature phase as

$$\mathcal{I}_{\text{PS}}^{(3)}(\chi_{ijk}^S) \propto 4\sqrt{C_1^2 + C_2^2} \quad (5.15)$$

and

$$\psi_{\text{PS}}^{(3)}(\chi_{ijk}^S) = \text{atan2}(C_1, C_2), \quad (5.16)$$

where

$$C_1 = -b \cdot d \sin \theta \cos^3 \theta, \quad (5.17)$$

$$C_2 = a \cdot d \sin \theta \cos^3 \theta, \quad (5.18)$$

θ is the angle of incidence, and

$$\text{atan2}(y, x) \equiv \begin{cases} \arctan\left(\frac{y}{x}\right) & x > 0 \\ \arctan\left(\frac{y}{x}\right) + \pi & y > 0, x < 0 \\ \arctan\left(\frac{y}{x}\right) - \pi & y < 0, x < 0 \\ +\frac{\pi}{2} & y > 0, x = 0 \\ -\frac{\pi}{2} & y < 0, x = 0 \\ \text{undefined} & x = y = 0 \end{cases}. \quad (5.19)$$

By comparing Eqs. 5.3 and 5.4, we find that

$$C_1 = C_2 = 0 \quad (5.20)$$

in the high temperature phase, so that $\mathcal{I}_{PS}^{(3)}(\chi_{ijk}^S) = 0$.

Note that Eq. 5.15 highlights an important aspect of our experiment, which is that $\mathcal{I}_{PS}^{(3)}$ requires a nonzero angle of incidence to be observed. This can be understood by noting that $\mathcal{I}_{PS}^{(3)}$ is nonzero only when the tensor element χ_{yxz}^S is nonzero. However, for such a term to be observable in the experiment, there needs to be an out-of-plane component to the incoming electric fields, which in turn requires a nonzero angle of incidence. Moreover, in a system with three-fold symmetry like 1T-TaS₂, the aforementioned tensor element can only be nonzero in a system where mirror symmetry is absent. To see that this is true, consider the term $P_y(2\omega) = \chi_{yxz}^S E_x(\omega) E_z(\omega)$. Under an $x \rightarrow -x$ mirror operation, we require that $P_y \rightarrow P_y$, $E_x \rightarrow -E_x$, $E_z \rightarrow E_z$, and $\chi_{yxz}^S \rightarrow \tilde{\chi}_{yxz}^S$. However, if this operation is a symmetry of the crystal then we have $\tilde{\chi}_{yxz}^S = \chi_{yxz}^S$, so that $P_y = -P_y$. This implies that $\chi_{yxz}^S = 0$. Therefore both a nonzero angle of incidence and broken mirror symmetry are required for a nonzero $\mathcal{I}_{PS}^{(3)}$ in the geometry of our experiment.

5.7.2 Physical importance of the $P_{\text{in}}\text{-}S_{\text{out}}$ channel

In this section we explain physically why the $P_{\text{in}}\text{-}S_{\text{out}}$ polarization channel is the most sensitive to mirror symmetry breaking in 1T-TaS₂. Consider the experimental geometry depicted in Fig. 5.6(a). A P -polarized electric field E_{in} is incident on a sample with vertical mirror symmetry about the xz plane (indicated by the sides A and B of the sample being the same color). The geometry is such that the plane of incidence makes an angle ϕ with the reflection plane. Let $\mathbf{P}_\perp(\phi)$ be the S -polarized component of the polarization resulting from second harmonic generation by the interaction of the sample with E_{in} .

Now consider applying the mirror operation both to E_{in} and to the sample (Fig. 5.6(b)). Then the resulting S -polarized component of the polarization (in the frame of the plane of incidence) will be $-\mathbf{P}_\perp(\phi)$. However, since the sides A and B in Fig. 5.6(b) are the same, by symmetry the problem is equivalent to Fig. 5.6(a) but with ϕ replaced by $-\phi$. Thus $\mathbf{P}_\perp(-\phi) = -\mathbf{P}_\perp(\phi)$, implying that $\mathbf{P}_\perp(0) = \mathbf{P}_\perp(\pi) = 0$. This along with

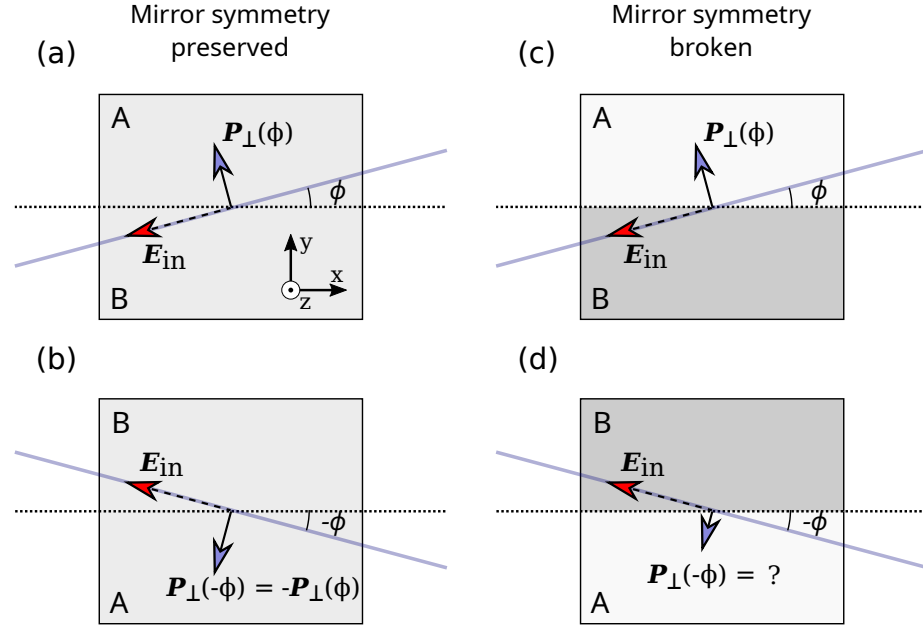


Figure 5.6: (a) Geometry referenced in showing that the $P_{\text{in}}\text{-}S_{\text{out}}$ geometry is sensitive to the breaking of vertical mirror symmetry. E_{in} is the input electric field and \mathbf{P}_{\perp} is the S -polarized component of the polarization. The arrow identifying the direction of E_{in} is dashed to indicate that there is a component in the z -direction (out of the page). The solid blue and dotted black lines represent the plane of incidence and the mirror symmetry plane, respectively, which are in the z -direction and make an angle ϕ with each other. The two halves (A and B) of the sample are the same color to indicate that mirror symmetry is present in this sample. (b) Mirror image of 5.6(a), showing that \mathbf{P}_{\perp} flips sign (when measured in the frame of the plane of incidence) under mirror reflection. (c) Same geometry as 5.6(a) with broken mirror symmetry, represented by the difference in color between sides A and B. (d) Mirror image of 5.6(c).

threefold rotational symmetry is sufficient to prove that the RA-SHG pattern from IC-phase 1T-TaS₂ in the P_{in}-S_{out} polarization channel is purely sixfold-symmetric. However, in the case where mirror symmetry is broken (Figs. 5.6(c) and 5.6(d)) the above argument no longer holds and the constraint $\mathbf{P}_\perp(-\phi) = -\mathbf{P}_\perp(\phi)$ is relaxed. Therefore in 1T-TaS₂, $\mathcal{I}_{PS}^{(3)}$ is allowed in the NC phase but not in the IC phase.

In contrast to the *S*-polarized output ($\mathbf{P}_\perp(\phi)$), the *P*-polarized output ($\mathbf{P}_\parallel(\phi)$) does not change sign (as defined in the frame of the plane of incidence) under mirror reflection. Therefore the constraint for *P*-polarized output is that $\mathbf{P}_\parallel(\phi) = \mathbf{P}_\parallel(-\phi)$. Importantly, this constraint does not forbid Fourier components like $\mathcal{I}_{PP}^{(3)}$ and $\mathcal{I}_{SP}^{(3)}$, even when mirror symmetry is present.

Finally, while the S_{in}-S_{out} channel is subject to the constraint $\mathbf{P}_\perp(-\phi) = -\mathbf{P}_\perp(\phi)$, it can also be shown (see section 5.7.5) that in the electric dipole regime, S_{in}-S_{out} is twofold-symmetric regardless of the crystallographic point group. Therefore the P_{in}-S_{out} polarization channel is especially sensitive to the breaking of vertical mirror plane symmetry in the geometry depicted in Fig. 5.6.

5.7.3 Generalization to other mirror symmetry-breaking transitions

While the argument above is effective in the case of a C_{3v} to C₃ transition (as in 1T-TaS₂), the presence or absence of other symmetries in different point groups may call for symmetry arguments which differ from those above. Therefore, to generalize this work we provide in table 5.1 a list of mirror-symmetry-breaking transitions between noncentrosymmetric point groups and identify corresponding terms (like $\mathcal{I}_{PS}^{(3)}$ in 1T-TaS₂) which adopt nonzero values in the low-symmetry phase. This table was generated using the same analysis as in section 5.7.1 for 1T-TaS₂. Note that while RA-SHG is only nonzero in noncentrosymmetric point groups, it can still be used in centrosymmetric materials because crystal surfaces necessarily break inversion symmetry.

In most of the transitions in table 5.1, $\mathcal{I}_{PS}^{(n)}$ can be used as an indicator of broken mirror symmetry for some n . However, for others the RA-SHG pattern rotates rather than (or in addition to) changing symmetry, which is indicated by a change in the phase $\psi_{\Gamma_{in}\Gamma_{out}}^{(n)}$ of certain Fourier components.

Initial group	Final group	Indicator(s)
T_d	T	None
T_d	D_{2d}	None
T_d	C_{3v}	None
C_{6v}	C_{3v}	$\mathcal{I}_{PP}^{(3)}, \mathcal{I}_{PP}^{(6)}, \mathcal{I}_{PS}^{(0)}, \mathcal{I}_{PS}^{(6)}, \mathcal{I}_{SP}^{(3)}, \mathcal{I}_{SP}^{(6)}, \mathcal{I}_{SS}^{(0)}, \mathcal{I}_{SS}^{(6)}$
C_{6v}	C_{2v}	$\mathcal{I}_{PP}^{(2)}, \mathcal{I}_{PP}^{(4)}, \mathcal{I}_{PS}^{(0)}, \mathcal{I}_{PS}^{(4)}, \mathcal{I}_{SP}^{(2)}, \mathcal{I}_{SP}^{(4)}$
C_{6v}	C_6	$\mathcal{I}_{PS}^{(0)}$
C_{4v}	C_{2v}	$\mathcal{I}_{PP}^{(2)}, \mathcal{I}_{PP}^{(4)}, \mathcal{I}_{PS}^{(0)}, \mathcal{I}_{PS}^{(4)}, \mathcal{I}_{SP}^{(2)}, \mathcal{I}_{SP}^{(4)}$
C_{4v}	C_4	$\mathcal{I}_{PS}^{(0)}$
D_{3h}	C_{3h}	$\psi_{PP}^{(6)*}, \psi_{PS}^{(6)*}, \psi_{SP}^{(6)*}, \psi_{SS}^{(6)*}$
D_{3h}	C_{2v}	None
D_{3h}	D_3	$\mathcal{I}_{PS}^{(3)}$
C_{3h}	C_3	$\psi_{PP}^{(1)*}, \psi_{PP}^{(2)*}, \psi_{PP}^{(3)*}, \psi_{PP}^{(4)*}, \psi_{PP}^{(5)*}, \psi_{PP}^{(6)*}, \psi_{PS}^{(1)*}, \psi_{PS}^{(2)*}, \psi_{PS}^{(3)*}, \psi_{PS}^{(4)*}, \psi_{PS}^{(5)*}, \psi_{PS}^{(6)*}, \psi_{SP}^{(1)*}, \psi_{SP}^{(2)*}, \psi_{SP}^{(3)*}, \psi_{SP}^{(4)*}, \psi_{SP}^{(5)*}, \psi_{SP}^{(6)*}, \psi_{SS}^{(1)*}, \psi_{SS}^{(2)*}, \psi_{SS}^{(3)*}, \psi_{SS}^{(4)*}, \psi_{SS}^{(5)*}, \psi_{SS}^{(6)*}$
C_{3v}	C_3	$\psi_{PP}^{(3)}, \psi_{PP}^{(6)*}, \mathcal{I}_{PS}^{(3)}, \psi_{PS}^{(6)*}, \psi_{SP}^{(3)}, \psi_{SP}^{(6)*}, \psi_{SS}^{(6)*}$
C_{3v}	C_{1h}	$\mathcal{I}_{PP}^{(1)}, \mathcal{I}_{PP}^{(2)}, \mathcal{I}_{PP}^{(4)}, \mathcal{I}_{PP}^{(5)}, \mathcal{I}_{PS}^{(1)}, \mathcal{I}_{PS}^{(2)}, \mathcal{I}_{PS}^{(3)}, \mathcal{I}_{PS}^{(4)}, \mathcal{I}_{PS}^{(5)}, \mathcal{I}_{SP}^{(1)}, \mathcal{I}_{SP}^{(2)}, \mathcal{I}_{SP}^{(4)}, \mathcal{I}_{SP}^{(5)}, \mathcal{I}_{SS}^{(2)}, \mathcal{I}_{SS}^{(4)}$
D_{2d}	S_4	$\psi_{PP}^{(4)*}, \psi_{PS}^{(4)*}, \psi_{SP}^{(4)*}$
D_{2d}	D_2	$\mathcal{I}_{PS}^{(2)}$
C_{2v}	C_2	$\psi_{PP}^{(2)*}, \psi_{PP}^{(4)*}, \mathcal{I}_{PS}^{(2)}, \psi_{PS}^{(4)*}, \psi_{SP}^{(2)*}, \psi_{SP}^{(4)*}$
C_{2v}	C_{1h}	$\mathcal{I}_{PP}^{(1)}, \mathcal{I}_{PP}^{(3)}, \mathcal{I}_{PP}^{(5)}, \mathcal{I}_{PP}^{(6)}, \mathcal{I}_{PS}^{(1)}, \mathcal{I}_{PS}^{(2)}, \mathcal{I}_{PS}^{(3)}, \mathcal{I}_{PS}^{(5)}, \mathcal{I}_{PS}^{(6)}, \mathcal{I}_{SP}^{(1)}, \mathcal{I}_{SP}^{(3)}, \mathcal{I}_{SP}^{(5)}, \mathcal{I}_{SP}^{(6)}, \mathcal{I}_{SS}^{(0)}, \mathcal{I}_{SS}^{(2)}, \mathcal{I}_{SS}^{(4)}, \mathcal{I}_{SS}^{(6)}$

* Measured from $\pi/2$

Table 5.1: Indicators of broken mirror symmetry in mirror-symmetry-breaking transitions between noncentrosymmetric point groups. Values in the rightmost column (defined in Eq. 5.14) are zero in the initial group and nonzero in the final group. In all cases, the analysis was done in a geometry such that the sample normal is parallel to the broken mirror plane (i.e. the mirror plane is vertical).

Additionally, it should be observed that for a minority of the transitions in table 5.1, RA-SHG is not sensitive to the breaking of mirror symmetry (e.g. in the transition from T_d to T , two point groups for which the susceptibility tensor is equivalent).

5.7.4 Probing the sense of planar chirality with RA-SHG

Complete RA-SHG data

As in section 5.7.1, for completeness we reproduce in Fig. 5.7 the RA-SHG data in the α and β CDW configurations, including the two polarization channels which were truncated from Fig. 5.3 in the main text. The poor fit in the $S_{\text{in}}\text{-}S_{\text{out}}$ polarization channel again indicated to us that there was an additional bulk quadrupole contribution to the signal.

Electron diffraction confirming the sample is single domain

To confirm that 1T-TaS₂ is single-domain in the NC phase, we performed electron diffraction on a sample from the same batch as the one used for the RA-SHG measurements. The absence of CDW sister peaks in Fig. 5.8 demonstrates that the sample is single-domain, in agreement with previous reports [12, 36, 107, 113]. The thickness of the sample measured by electron diffraction was ~ 80 nm, which is approximately equal to the penetration depth of 1T-TaS₂ at 800 nm [61]. We note that recent studies have demonstrated that it is possible to inject mirror domains into an otherwise uniform sample of 1T-TaS₂ using intense pulses of light [113]. To control for this effect, we used an incident fluence of 1.4 mJ/cm² which is well below the threshold fluence 5 mJ/cm² reported in Zong et al. [113].

Fitting RA-SHG data in the α and β configurations

To fit the data in Fig. 5.3 of the main text, we performed the following procedure. First, we used the six independent elements in the C_3 susceptibility tensor given by Eq. 5.3 as fitting parameters to fit the data on the α sample (Fig. 5.7(a)) to

$$|P_i(\phi)|^2 \propto |R(-\phi)_{il}R(-\phi)_{jm}R(-\phi)_{kn}\chi_{lmn}^S E_j(\omega)E_k(\omega)|^2. \quad (5.21)$$

The fit was constrained in such a way as to forbid large changes in the susceptibility elements that exist in both phases (i.e. a , c , e , and f). This

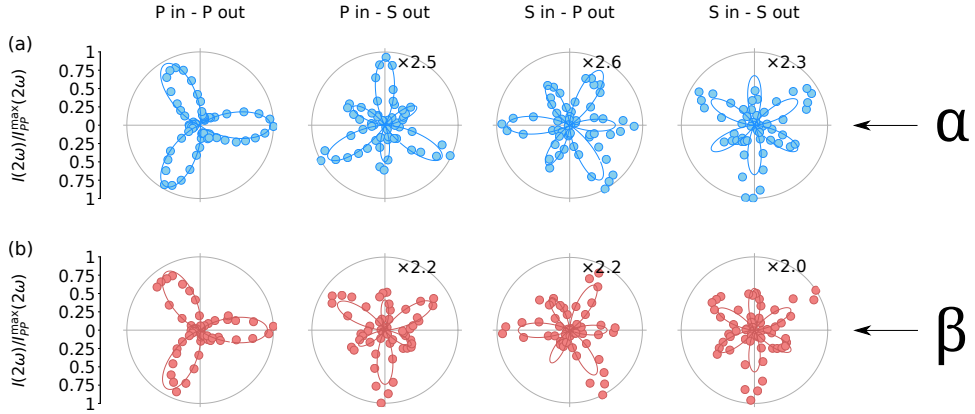


Figure 5.7: Second harmonic intensity as a function of ϕ from two samples of 1T-TaS₂ in the NC phase ($T = 340\text{K}$). The labels α and β refer to the two degenerate mirror-image configurations which can exist in the NC phase. The solid line in (a) is a fit to the data using the surface point group C_3 . The fit in (b) was generated by performing a mirror operation (see section 5.7.4) to the numerical susceptibility tensor obtained from 5.7(a). Data is normalized to the maximum value in the P_{in}-P_{out} polarization channel for each sample.

gave us a set of six numbers $\{\chi_{ijk}^{\alpha}\}$, from which we can form the tensor χ_{ijk}^{α} . The cleaving operation can be represented by the operator $\mathcal{C} = A\Gamma(\gamma)R_x$, where R_x is the operator which rotates the sample 180° about the x -axis,

$$R_x = \begin{pmatrix} 1 & 0 & 0 \\ 0 & -1 & 0 \\ 0 & 0 & -1 \end{pmatrix}, \quad (5.22)$$

$\Gamma(\gamma)$ is the operator which rotates the sample about the z -axis by an arbitrary angle γ ,

$$\Gamma(\gamma) = \begin{pmatrix} \cos \gamma & -\sin \gamma & 0 \\ \sin \gamma & \cos \gamma & 0 \\ 0 & 0 & 1 \end{pmatrix}, \quad (5.23)$$

and A is a positive overall constant which represents minor, day-to-day fluctuations in experimental conditions. If we were able to cleave the sample exactly along the high-symmetry axis, then γ would be 0° and $\Gamma(\gamma)$ would be identity. Also note that the fact that the determinant of \mathcal{C} in the (x, y) subspace is -1 is equivalent to the statement that \mathcal{C} switches the planar chirality of the sample.

To simulate the effect of cleaving the sample, we therefore applied \mathcal{C} to χ_{ijk}^α to form $\chi_{ijk}^\beta(\{\chi_{ijk}^\alpha\}, \gamma, A)$. Formally, this amounts to computing

$$\chi_{ijk}^\beta(\{\chi_{ijk}^\alpha\}, \gamma, A) = \mathcal{C}_{il}(\gamma, A)\mathcal{C}_{jm}(\gamma, A)\mathcal{C}_{kn}(\gamma, A)\chi_{lmn}^\alpha. \quad (5.24)$$

Now, $\chi_{ijk}^\beta(\{\chi_{ijk}^\alpha\}, \gamma, A)$ is a function of only two free parameters (γ and A). We find that with the proper choice of γ and A , the signal computed with χ_{ijk}^β collapses onto the data in Fig. 5.7(b).

By applying R_x to the tensor given in Eq. 5.3, one can see that the effect of cleaving the sample is to flip the sign of b and d . By examining Eqs. 5.9–5.12, and noting that $A_1 \approx 0$ within the resolution of our instrument, we see that this reproduces the change of the orientation of the RA-SHG pattern in the P_{in} - S_{out} channel depicted in Fig. 5.3 of the main text.

5.7.5 Bulk broken mirror symmetry in 1T-TaS₂

Complete RA-SHG data at $T = 295K$

As in section 5.7.4, for completeness we reproduce in Fig. 5.9 the RA-SHG data at $T = 295K$ (NC phase) which is used in Fig. 5.4 to argue that there is a nonzero bulk electric quadrupole component to the measured signal. Furthermore, we reproduce in Fig. 5.10 the RA-SHG data at $T = 356K$ (IC phase) to show that we can fit all four polarization combinations using the surface point group C_{3v} as well as a bulk point group S_6 , which is the highest-symmetry subgroup of the undistorted point group which breaks mirror symmetry (see below). The S_{in} - S_{out} channel of Fig. 5.10 is shown in Fig. 5.4 of the main text.

Symmetry analysis of RA-SHG data

In the last section of the main text, we used the relation given by Eq. 5.2 to argue that the breaking of sixfold symmetry in the S_{in} - S_{out} polarization

channel indicates that bulk mirror symmetry is broken in the IC phase of 1T-TaS₂. Here we derive Eq. 5.2 as we did Eq. 5.1 in section 5.7.1.

As mentioned in the main text, the effective polarization for bulk electric quadrupole SHG is given by [52, 90]

$$\nabla_j Q_{ij} = 2i\chi_{ijkl}^Q k_j E_k E_l, \quad (5.25)$$

so that the total intensity in the S_{in}-S_{out} channel (including surface electric dipole) is given by

$$I_{SS}^{2\omega}(\phi) \propto \left| \left(\bar{\chi}_{yjk}^S(-\phi) + 2i\bar{\chi}_{ypjk}^Q(-\phi)k_p \right) E_j(\omega) E_k(\omega) \right|^2, \quad (5.26)$$

where

$$\bar{\chi}_{ijk}^S(\phi) = R(\phi)_{il} R(\phi)_{jm} R(\phi)_{kn} \chi_{lmn}^S, \quad (5.27)$$

$$\bar{\chi}_{ipjk}^Q(\phi) = R(\phi)_{il} R(\phi)_{pq} R(\phi)_{jm} R(\phi)_{kn} \chi_{lqmn}^Q, \quad (5.28)$$

and $E_i(\omega) = (0, 1, 0)_i^T$.

In the NC phase of 1T-TaS₂, the appropriate assignment for the surface and bulk point groups is given by diffraction measurements [92] to be C_3 and S_6 , respectively. Therefore for χ_{ijk}^S we use the tensor defined by Eq. 5.3, and for χ_{ijkl}^Q we use the tensor given in Boyd [13] for the point group S_6 (which for the sake of brevity we do not reproduce here). With these tensors, we then have

$$I_{SS}(2\omega) \propto (B_0 + B_1 \cos(3\phi) + B_2 \sin(3\phi))^2, \quad (5.29)$$

with

$$B_0 = \chi_{xyxx}^Q \sin \theta, \quad (5.30)$$

$$B_1 = \chi_{yyy}^S - \chi_{xzxz}^Q \cos \theta, \quad (5.31)$$

and

$$B_2 = -\chi_{xxx}^S + \chi_{xzzy}^Q \cos \theta. \quad (5.32)$$

Importantly, if bulk mirror symmetry were restored in the IC phase we would have $\chi_{xyxx}^Q = \chi_{xzxz}^Q = 0$, and therefore $B_0 = 0$. This can be checked by inspecting the quadrupole susceptibility tensor for the undistorted bulk point group D_{3d} (which preserves vertical mirror symmetry) defined in Boyd [13].

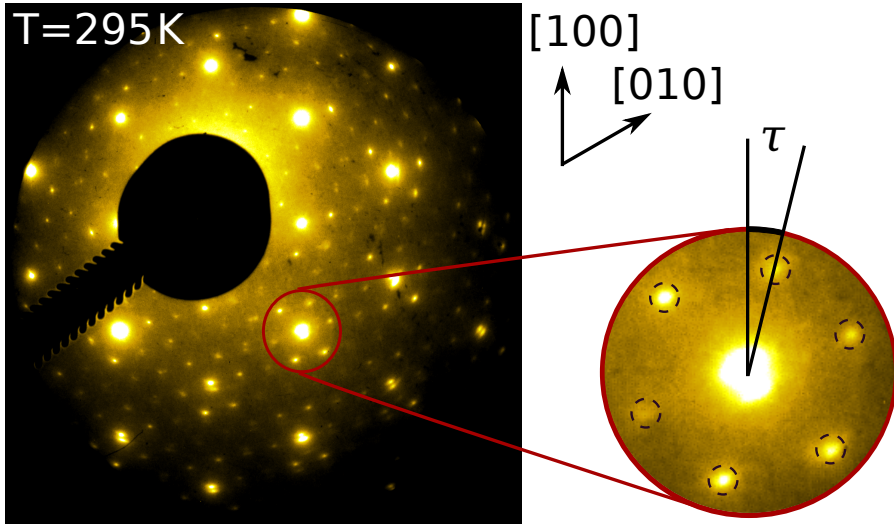


Figure 5.8: Electron diffraction data from a sample of 1T-TaS₂ in the NC phase of the same batch as the one used in RA-SHG measurements. Surrounding each Bragg reflection can be seen six CDW peaks, which are rotated about $\tau = 13^\circ$ from the high-symmetry axes. The sign of the rotation angle τ indicates whether the CDW configuration is α or β . The lack of additional CDW peaks -13° from the high-symmetry axes indicates that the sample is single-domain.

Since $B_0 = 0$ if the pattern possesses sixfold rotational symmetry (as can be seen by taking $\phi \rightarrow \phi + 60^\circ$), we have that the breaking of sixfold rotational symmetry in the RA-SHG pattern (Fig. 5.4(c) of the main text) implies $B \neq 0$. This implies that $\chi_{xyxx}^Q \neq 0$, and therefore mirror symmetry is broken in the bulk.

There are two additional important remarks which can be made about Eq. 5.29. For one, it should be noted that the θ dependence observed in Figs. 5.4(a) and 5.4(b) is consistent with Eq. 5.29, since $B_0 = 0$ for $\theta = 0$. Additionally, we see that in the absence of the quadrupole component (i.e. for purely electric dipole SHG), $B_0 = 0$ and the pattern should have sixfold rotational symmetry. Since the data in Figs. 5.4(a) and 5.4(c) clearly break

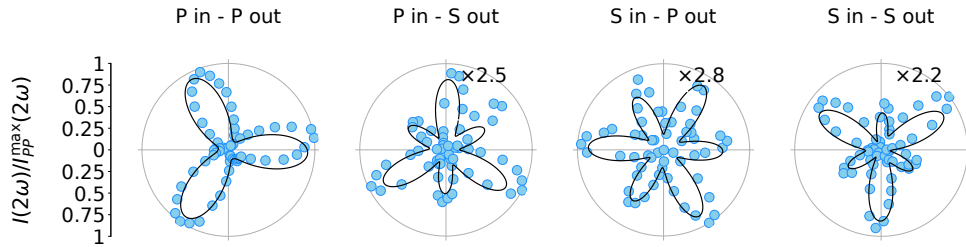


Figure 5.9: RA-SHG intensity as a function of ϕ at $T = 295K$. Solid lines are best fits to the data using a surface electric dipole term in the point group C_3 , as well as a bulk electric quadrupole term in the point group S_6 . Data is normalized to the maximum value of the $P_{\text{in}}-P_{\text{out}}$ signal.

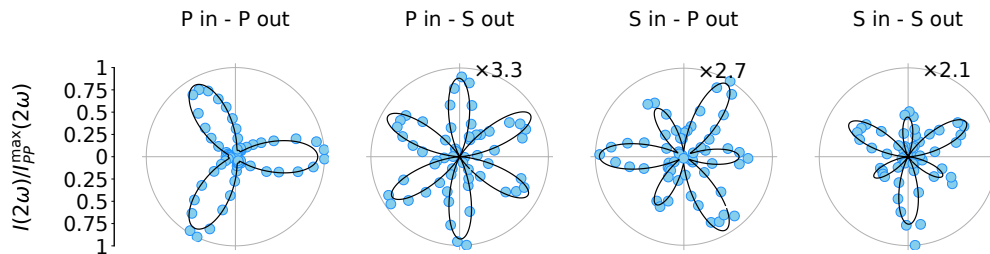


Figure 5.10: RA-SHG intensity as a function of ϕ at $T = 356K$. Solid lines are best fits to the data using a surface electric dipole term in the point group C_{3v} , as well as a bulk electric quadrupole term in the point group S_6 . Data is normalized to the maximum value of the $P_{\text{in}}-P_{\text{out}}$ signal.

this symmetry, this supports our claim that there is an extra contribution to the RA-SHG beyond the surface electric dipole contribution.

A more intuitive way to understand why the threefold spectral component in Fig. 5.4(a) and Fig. 5.4 is not allowed by pure electric dipole SHG is to note that, for purely electric dipole SHG, the rotational anisotropy always has at least twofold symmetry in the $S_{\text{in}}-S_{\text{out}}$ channel. To see that this is true, consider the effect of taking $\phi \rightarrow \phi + \pi$ in an S -polarized input geometry. In the frame where the sample is stationary, this simply changes the sign of the input field. Since the polarization is proportional to the square of the input field ($P_i(2\omega) = \chi_{ijk}E_jE_k$), then it will be symmetric under $\phi \rightarrow \phi + \pi$, as will be its projection out of the plane of incidence

(note, however, that because the component of $\mathbf{P}(2\omega)$ parallel to the direction of propagation is not visible in the experiment, the same cannot be said for the P -polarized output). Therefore, if the measured RA-SHG in the S_{in} - S_{out} channel lacks twofold symmetry, then there is a contribution to the rotational anisotropy which exists beyond the electric dipole.

For the sake of completeness, we also note here two alternative explanations for the breaking of sixfold rotational symmetry depicted in Fig. 5.4(c) which do not appeal to an additional quadrupole contribution. Firstly, it is possible that the surface of the sample was rough or nonuniform in such a way as to modulate the observed SHG intensity as a function of ϕ . In principle, this could result in a nonzero B_0 . To account for this artifact, we measured SHG on 1T-TaS₂ in multiple locations and on multiple different samples, and found that the results in this work were consistent across all measurements. Furthermore, with SHG measurements there is always the possibility of an additional contribution arising from the presence of adsorbates on the sample surface[9]. While such a contribution may be present in our experiment, we note that this too is an unlikely explanation for the nonzero B_0 because of the wavevector dependence of Figs. 5.4(a) and 5.4(b). This is because the dominant contribution from adsorbates is generally of the electric dipole type and therefore should not depend on k in S_{in} - S_{out} .

5.7.6 Methods

RA-SHG data was taken with the 800 nm pulsed output of a regeneratively amplified Ti:Sapphire laser operating at 5 kHz. The beam was scattered by a transmissive phase grating into multiple diffraction orders, and the +1-order component was steered through a polarizer and focused onto the sample with a fluence of 1.4 mJ/cm² and a spot diameter of \sim 150 μ m at a 10° angle with respect to the (001) sample normal. This experimental geometry is similar to that described in Harter et al. [37] and Torchinsky et al. [99]. The reflected light at 400 nm was directed through an analyzer and into a photomultiplier tube, where the intensity was measured with a lock-in amplifier synchronized to the 5 kHz pulsed output of the laser with a 1 ms time constant. We rotated the phase grating at \sim 5 Hz and recorded the signal as a function of time with an oscilloscope triggered on an optical rotary encoder marking 360° rotations. Each polarization combination required averaging 5000 rotations. Using the aforementioned encoder, we

expressed the corresponding time trace in terms of the azimuthal angle ϕ (Fig. 5.1(b)) to obtain the full rotational anisotropy.

The thickness of the samples used in the RA-SHG experiments was $\sim 50 \mu\text{m}$.

Chapter Six

Light-induced reorientation transition in the antiferromagnetic semiconductor CaMn_2Bi_2

6.1 Preface

This chapter is based on a manuscript intended for standalone publication and modified to fit the format of this thesis. It was coauthored by myself and Baiqing Lv (as co-first authors), along with Karna Morey, Zongqi Shen, Changmin Lee, Elizabeth Donoway, Alex Liebman-Peláez, Anshul Kogar, Takashi Kurumaji, Martin Rodriguez-Vega, Rodrigo Humberto Aguilera del Toro, Mikel Arruabarrena, Batyr Ilyas, Tianchuang Luo, Peter Müller, Aritz Leonardo, Andres Ayuela, Gregory A. Fiete, Joseph G. Checkelsky, Joseph Orenstein, and Nuh Gedik. A detailed description of each author's contributions may be found in ??.

6.2 Abstract

Due to the lack of a net magnetic moment, antiferromagnets possess a unique robustness to external magnetic fields and are thus predicted to play an important role in future magnetic technologies. However, this robustness also makes them quite difficult to control, and the development of novel methods to manipulate these systems with external stimuli is a fundamental goal of antiferromagnetic spintronics. In this work, we

report evidence for a metastable reorientation of the order parameter in an antiferromagnetic semiconductor triggered by an ultrafast quench of the equilibrium order via photoexcitation above the band gap. The metastable state forms less than 10 ps after the excitation pulse, and persists for longer than 150 ps before decaying to the ground state via thermal fluctuations. Importantly, this transition cannot be induced thermodynamically, and requires the system to be driven out of equilibrium. Broadly speaking, this phenomenology is ultimately the result of large magnetoelastic coupling in combination with a relatively low symmetry of the magnetic ground state. Since neither of these properties are particularly uncommon in magnetic materials, the observations presented here imply a generic path toward novel device technology enabled by ultrafast dynamics in antiferromagnets.

6.3 Introduction

When the Hamiltonian of a system contains multiple interaction strengths of comparable magnitude, the corresponding free energy is often host to a diverse collection of metastable states just barely separated in energy from the true ground state. This phenomenology results in an extreme sensitivity to external stimuli[5, 20, 112], which can be exploited in an ultrafast way using light to drive transitions between these states[6, 26, 49, 67].

One important application is in magnetic devices, where the electron spins form an ordered state in equilibrium and may thus be used to store information. AFMs have received special attention in this regard, as they possess zero net magnetic moment and are thus robust to stray magnetic fields from adjacent magnetic devices[46]. The dominance of exchange rather than anisotropy energies in the dynamics of spins which are antiferromagnetically ordered also leads to order-of-magnitude faster switching timescales compared to their ferromagnetic counterparts[72].

Importantly, the ground state of an AFM is typically not unique, with the number of degenerate states (corresponding generically to various rotations of the AFM OP) being determined by the number of symmetries which are broken at the magnetic ordering temperature. In the context described above, this degeneracy invites the possibility of an ultrafast antiferromagnetic device which uses light to switch between these different

states. Moreover, if the symmetry of the magnetic phase is sufficiently low (relative to the parent phase), the number of such states can be quite high, and a multi-step magnetic memory might be constructed which operates via ultrafast reorientation transitions of the AFM OP between states that are not anti-parallel.

Broadly speaking, one can distinguish two different approaches for achieving such transitions in real materials. In the first case, one imagines manipulating the AFM orientation “coherently” by, for example, resonantly driving an infrared-active phonon mode to large amplitude, although this usually requires large electric fields (as the relevant light-matter interactions are usually highly nonlinear[1]) which are difficult to obtain in the frequency range associated with phonons in crystals. An alternative mechanism—which has been shown to occur abundantly in superconductivity (SC)[26] and CDW[49] systems—is to *quench* the equilibrium order by exciting carriers above the band gap, and then exploit the subsequent relaxation dynamics which may, in the right system, show a preference for one state over the other[95]. In contrast to the case of resonant phonon driving, this mechanism involves primarily electronic excitations and therefore requires relatively little energy if the photon frequency is above the band gap. However, despite successful demonstrations of this approach in nonmagnetic systems[26, 49], evidence for this mechanism occurring in AFMs does not currently exist, and whether the phenomenology described here actually occurs in real magnetic materials remains a fundamental open question.

In this work, we report a light-induced phase transition between nearly degenerate AFM states in the antiferromagnetic semiconductor CaMn₂Bi₂[35] triggered by an ultrafast quench of the equilibrium OP with a femtosecond light pulse. Using tr-SHG, a pump-probe technique with the unique ability to track both the magnitude and direction of the AFM order parameter as a function of time, we find that above-gap optical excitation indeed causes the system to switch to a new, metastable orientation of the AFM OP. The transition is fast (occurring less than 10 ps after photoexcitation), requires low pump fluence ($\sim 200 \mu\text{J} \cdot \text{cm}^{-2}$ vs. $\sim 10 \text{ mJ} \cdot \text{cm}^{-2}$ [1]), and cannot be induced thermodynamically. These findings suggest a new way to manipulate AFMs, and open the door to novel opto-spintronic device architectures exploiting nonequilibrium phase transitions between different nearly degenerate states.

6.4 Results

6.4.1 Equilibrium

Crystallographically, CaMn_2Bi_2 consists of a puckered-honeycomb tiling of Mn atoms with a high-temperature crystallographic point group of $\bar{3}m$ (see Fig. 6.1(a)). The electronic gap is on the order of 4 meV (see Fig. 6.1(b)) and is thought to be due to a delicate combination of correlations and hybridization between relatively localized Mn $3d$ states and dispersive Bi $6p$ / Mn $4s$ hybrid bands[35, 53, 79]. Néel-type antiferromagnetic long-range order (LRO) with spins lying in the ab -plane develops in this material at $T_c = \sim 150$ K, accompanied by a kink in the electrical resistivity (Fig. 6.1(b)) and the appearance of a new peak in the powder neutron diffraction[35]. Importantly, the powder neutron refinement indicates that the ordered moments are slightly misaligned with the a - and b -axes of the high-symmetry phase (see Fig. 6.1(a)), so that the low-temperature magnetic point group is $\bar{1}'$; i.e., the only symmetries that are preserved in the low temperature phase are the identity operator and the product of inversion and time-reversal[35]. The remarkably low symmetry of this magnetic ground state is likely due to highly frustrated magnetic interactions, as suggested by the proximity of isostructural CaMn_2Sb_2 to a mean-field magnetic tricritical point[63, 64]. In contrast, the lattice is thought to remain fully symmetric at all temperatures, so that the symmetry-breaking at T_c is solely due to the AFM order (this is verified with single-crystal X-ray diffraction (XRD), see Supplementary material, Fig. 6.13).

As spin-orbit coupling is expected to be strong in this material, the breaking of inversion symmetry by the magnetic order should result in a strong SHG signal below T_c , despite the fact that the lattice remains centrosymmetric[74, 88]. We probe this SHG signal using a RA-SHG apparatus (Fig. 6.1(c)) which measures the reflected second harmonic intensity as the plane of incidence is rotated about the sample normal[27, 37, 99]. Figs. 6.1(b) and 6.1(d) depict the SHG signal from the (011) surface of CaMn_2Bi_2 as a function of temperature across T_c , demonstrating that RA-SHG is indeed sensitive to the magnetic order in this material.

Frequently, AFM materials may host intricate domain configurations, the details of which greatly impact the relevant magnetic functionalities[83, 106]. Because the low-temperature magnetic point group of CaMn_2Bi_2 breaks

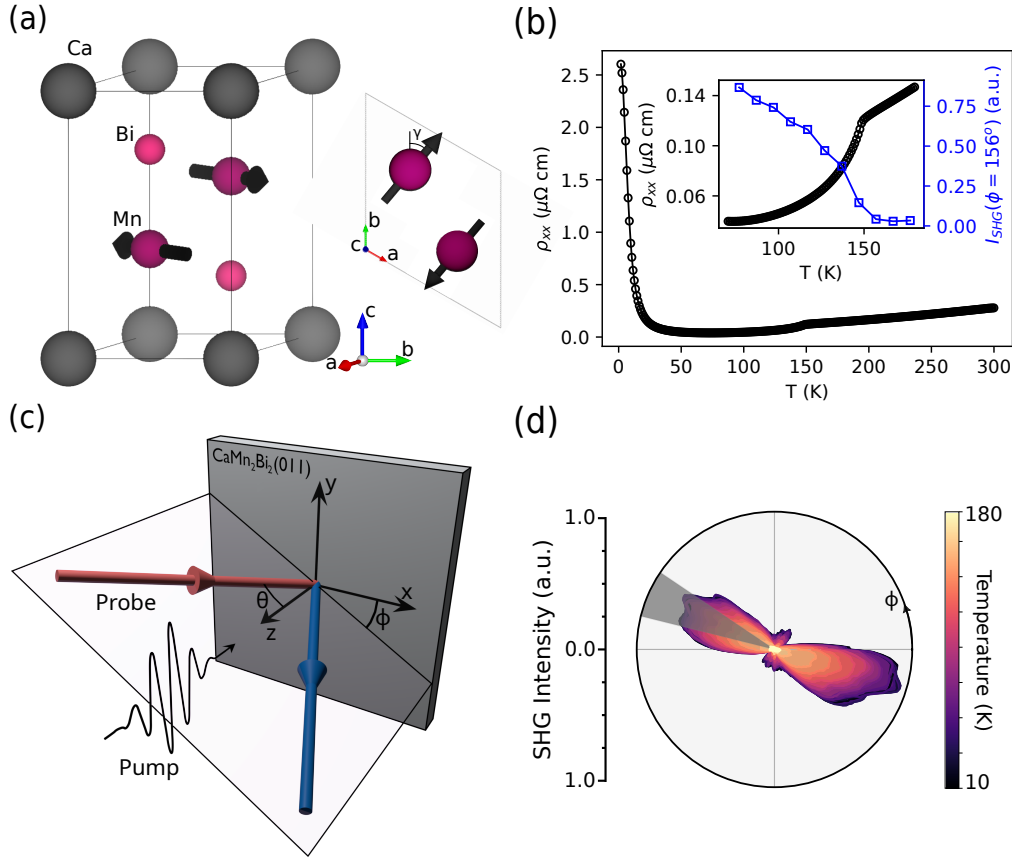


Figure 6.1: (a) Magnetic unit cell of CaMn_2Bi_2 . The angle γ is such that the Mn spin does not lie precisely along any particular crystallographic axis. (b) Resistivity as a function of temperature for a representative sample. Inset shows an enlarged view of the resistivity near T_c plotted against the SHG intensity integrated across the region indicated in 6.1(d). (c) Schematic of the RA-SHG setup. (d) Temperature dependence of the RA-SHG intensity in the $P_{\text{in}}P_{\text{out}}$ polarization channel from the (011) surface of CaMn_2Bi_2 . Other polarization channels are shown in the Supplementary material, Fig. 6.14. The shaded area indicates the region integrated to produce the inset of 6.1(b).

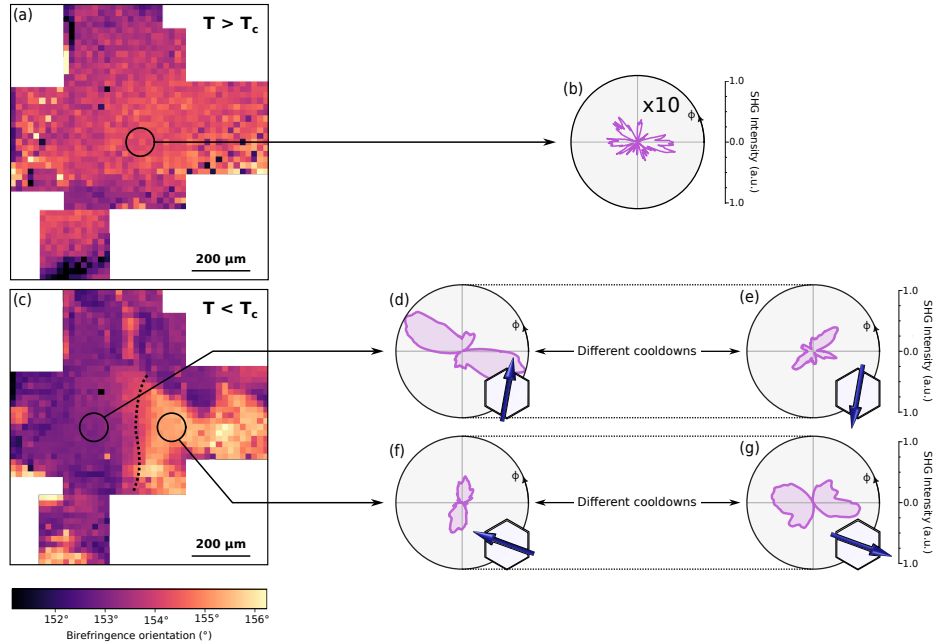


Figure 6.2: (a) Birefringence orientation map for $T = 200 \text{ K} > T_c$. (b) RA-SHG intensity in the $P_{\text{in}}P_{\text{out}}$ polarization channel for the region indicated in 6.2(a) at 157 K. Other polarization channels are shown in the Supplementary material, Fig. 6.15. (c) Birefringence orientation map for $T = 152.5 \text{ K} < T_c$. (d) (e) RA-SHG intensity at 8 K in the $P_{\text{in}}P_{\text{out}}$ polarization channel for consecutive cooldowns for the region indicated in 6.2(c). The system randomly chooses the RA-SHG pattern in 6.2(d) or 6.2(e) on each cooldown. Insets show the corresponding value of the AFM OP proposed in the text, relative to the hexagonal crystallographic motif. Other polarization channels are shown in the Supplementary material, Fig. 6.15. (f) (g) RA-SHG intensity at 8 K in the $P_{\text{in}}P_{\text{out}}$ polarization channel for consecutive cooldowns for the region indicated in 6.2(c). The system randomly chooses the RA-SHG pattern in 6.2(f) or 6.2(g) on each cooldown. Insets show the corresponding value of the AFM OP proposed in the text, relative to the hexagonal crystallographic motif. Other polarization channels are shown in the Supplementary material, Fig. 6.15. The schematic representations beneath the RA-SHG plots are for illustration purposes only and the depicted angles are not quantitatively verified.

multiple symmetries of the high-temperature point group, we indeed expect that the low-temperature magnetic ground state should involve some number of energetically degenerate domains. In Fig. 6.2, we characterize these domains using a combination of RA-SHG and a spatially-resolved optical polarimetry technique known as photo-thermal modulated birefringence (PTMB), which is a sensitive technique for measuring small changes in the anisotropic index of refraction (and consequently, the direction of the AFM OP)[54, 58].

Fig. 6.2(a) shows the PTMB signal from the (011) surface of CaMn_2Bi_2 above T_c . No contrast is found within a $\sim 500 \mu\text{m} \times 500 \mu\text{m}$ area on the sample, suggesting that the thermally modulated index of refraction is spatially uniform at high temperature. As the temperature is lowered below T_c (Fig. 6.2(c)), a pronounced contrast appears in the PTMB map which indicates the presence of two separate AFM domains with different OP directions.

While PTMB is nominally sensitive to the direction of the AFM OP, it cannot differentiate between 180° domains as it couples only to the linear index of refraction of the material. Therefore, it is not clear from PTMB alone whether the domains in Fig. 6.2(c) are truly homogeneous or may contain a mixture of 180° domains. In contrast, nonlinear spectroscopies like SHG can differentiate 180° AFM domains due to an interference between the SHG sources (e.g. electric dipole, magnetic dipole, and electric quadrupole) which transform differently under time-reversal symmetry[29–32]. This effect can be especially pronounced in the presence of magnetostriction[31]. We thus proceed to investigate the presence of 180° domains in this material using RA-SHG.

Figs. 6.2(d–g) depict the RA-SHG results at 8 K in the two regions identified in Fig. 6.2(c). The same crystal piece was used for both measurements. As with PTMB, we do find that the SHG domains are large and apparently homogenous (on a scale of hundreds of μm). Surprisingly, however, in different cooldowns we observe that the RA-SHG pattern in the leftmost region of Fig. 6.2(c) randomly takes the form of either Fig. 6.2(d) or Fig. 6.2(e), and in the rightmost region, it takes the form of either Fig. 6.2(f) or Fig. 6.2(g). In contrast, the PTMB does not change upon thermal cycling. Anticipating again that RA-SHG should be sensitive to the phase of the AFM OP as well as its direction, we interpret Fig. 6.2 as follows: Fig. 6.2(d) and Fig. 6.2(e) correspond to opposite 180° AFM domains, as do Fig. 6.2(f) and Fig. 6.2(g); in addition, there is a relative

angle between Figs. 6.2(d)–e) and Figs. 6.2(f)–g), as indicated by the PTMB. This interpretation is depicted schematically in the insets to Figs. 6.2(d)–g), where the AFM OP (defined as the difference in the magnetic moment on the two Mn sublattices, see Fig. 6.1(a)) is represented by a blue arrow. Importantly, within a single location, the two opposite orientations are accessible via thermal cycling; hence they are energetically degenerate. We have verified that the identification described here is consistent with the SHG susceptibility tensors[13] extracted by fitting the data in Fig. 6.2 (see Supplementary material, section 6.10.3). In addition, the data presented in Fig. 6.2 is not consistent with an alternative interpretation involving the interference of two independent order parameters (see Supplementary material, section 6.10.2).

6.4.2 Nonequilibrium

Having demonstrated that CaMn_2Bi_2 hosts an elaborate free energy surface with multiple degenerate or nearly degenerate ground states, we now turn to the question of whether light can be used to manipulate or possibly switch between these states. To answer this question, we pump each of the OP directions identified in Fig. 6.2 at 8 K with a \sim 100 fs normally incident near-infrared light pulse ($\hbar\omega \approx 1$ eV) and probe the AFM OP with RA-SHG using a subsequent probe pulse. By varying the delay Δt between the two pulses, we create a series of snapshots of the AFM OP at different times following excitation. The results are shown in Fig. 6.3, where the four rows correspond to the four OP directions identified in Fig. 6.2, and the horizontal axis is the time delay between the pump and probe pulses. The first two rows (Figs. 6.3(a)–b)) correspond to the left-most domain in Fig. 6.2(c), for which it is found that, after pumping, the strength of the RA-SHG signal is quickly extinguished. After a delay of around \sim 8 – 10 ps, the AFM order recovers so that the shape of the RA-SHG pattern is similar to before zero delay up to small changes in the relative peak heights. The OP magnitude and direction inferred by this data is depicted schematically in the insets to Figs. 6.3(a)–b).

The striking observation is in the latter two rows (Figs. 6.3(c)–d)), which depict the time-resolved RA-SHG results in the rightmost domain of Fig. 6.2(c). In this domain, the RA-SHG signal again quickly decreases, and the shape does not initially change. However, roughly \sim 6 – 8 ps after excitation, the RA-SHG pattern abruptly changes shape, so that the

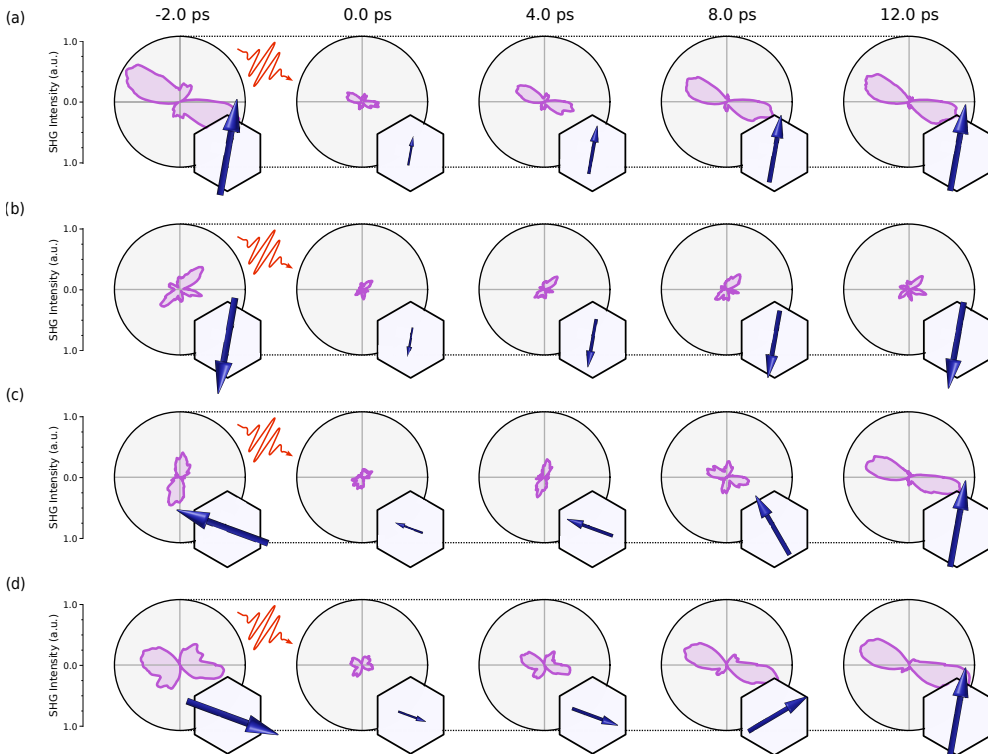


Figure 6.3: RA-SHG intensity at 8 K in the $P_{\text{in}}P_{\text{out}}$ polarization channel as a function of time for the AFM OP identified in (a) Fig. 6.2(d), (b) Fig. 6.2(e), (c) Fig. 6.2(f), and (d) Fig. 6.2(g). The pump fluence is set to $\sim 600 \mu\text{J} \cdot \text{cm}^{-2}$. Insets show the corresponding value of the AFM OP proposed in the text, relative to the hexagonal crystallographic motif. Other polarization channels are shown in the Supplementary material, Fig. 6.16. The schematic representations beneath the RA-SHG plots are for illustration purposes only and the depicted angles are not quantitatively verified.

pattern after ~ 10 ps is equivalent to Fig. 6.3(a). Together with the findings of Fig. 6.2, these results suggest that the final state in Figs. 6.3(c)–d) is one in which the AFM OP direction has indeed been reoriented relative to equilibrium. Remarkably, one must use light to reach this metastable state as it is not present in thermal equilibrium at this spot.

We performed the above measurements out to $\Delta t \gtrsim 150$ ps (see Supplementary material, Fig. 6.19) and found that the reoriented state persists at least this long before relaxing back to equilibrium in time for the next pair of pulses to arrive (roughly 200 μ s later). As the pump fluence is decreased (see Supplementary material, Fig. 6.11), the effect of the excitation is diminished until, at low fluences ($\sim 100 \mu\text{J} \cdot \text{cm}^{-2}$), the final state is equivalent to the initial state, and only small changes to the SHG (associated with dynamics that do not launch the system into the metastable state) are visible near zero delay. Interestingly, which of the two opposite directions (Fig. 6.2(d) or Fig. 6.2(e)) the magnetic order favors after excitation is consistent from pulse to pulse, but not from one sample to another (see Supplementary material, Figs. 6.18 and 6.19), suggesting that, below the magnetic ordering temperature, interactions between neighboring domains break the degeneracy between these states. Finally, we note that no aspect of these observations changes with the polarization of the pump pulse (see Supplementary material, Fig. 6.17).

6.5 Discussion

Taken together, these considerations indeed point to a *bona fide* ultrafast phase transition in CaMn₂Bi₂ induced by a femtosecond light pulse. We now seek to understand, at least qualitatively, the microscopic nature of this transition. Before discussing the time-resolved data of Fig. 6.3, we must first understand the equilibrium phenomenology implied by Fig. 6.2. Group theory (see Supplementary material, section 6.10.1) suggests that there should be twelve energetically degenerate OP directions, independent of location on the sample. However, only two directions are observed per measurement location in our experiment. This observation is explained by recognizing that local strain fields in the material are expected to pole the LRO (see Supplementary material, section 6.10.1), so that certain OP directions are energetically favored relative to others at a given spot[40, 71]. Since these strain fields may vary from one loca-

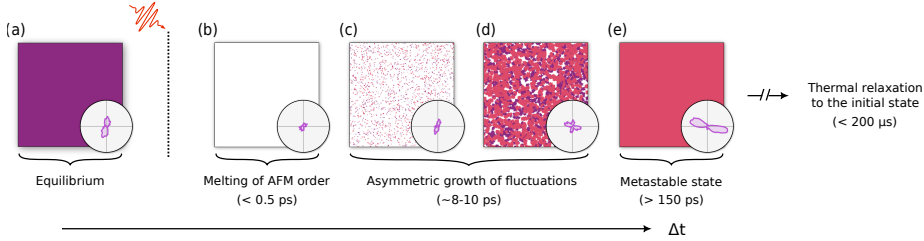


Figure 6.4: Illustration of the dynamics following laser excitation as described in the text. Ultrafast melting of the AFM order (6.4(a)-6.4(b)) is followed by the rapid growth of fluctuations (6.4(c)-6.4(d)), with the final state (6.4(e)) determined by the relative growth rate of different orders. The fluctuation growth step (6.4(c)-6.4(d)) may occur with or without a background of coherent oscillations (see Supplementary material, section 6.10.1).

tion to another (the details of which depend subtly on the local growth conditions), different locations on the sample would then show different sets of RA-SHG patterns, in agreement with the findings of Fig. 6.2. This picture also explains the observation that opposite AFM configurations are energetically degenerate, as strain itself is inherently symmetric under 180° rotations.

Turning now to the nonequilibrium phenomenology (Figs. 6.3 and 6.4), we begin by noting that the sudden suppression of the SHG intensity at early times indicates that the primary effect of the pump pulse is simply to quench the AFM OP (Figs. 6.4(a) and 6.4(b)). According to recent theoretical work [22, 95], the dynamics following such a quench are governed not by the global minimum of the free energy, but rather by the exponential amplification of spatial OP fluctuations (Figs. 6.4(c) and 6.4(d)), which may occur differently for different orders (Supplementary material, section 6.10.1). The final state of the transition (Fig. 6.4(e)) is then determined by which state supports the fastest-growing fluctuations. In the context of light-induced SC[17, 26], for example, the dominant order in equilibrium is a CDW, whose fluctuations naturally involve motion of the massive nuclei and are thus much slower than fluctuations of the SC OP[91, 95]. Note that, in the general case, the final state is determined not

just by the relaxation rates, but also by their start times; that is, if one order is *quenched* faster than another, fluctuations of that order are afforded a longer period to grow and may thus dominate at long times.

In our system, the relatively slow ($\sim 8 - 10$ ps, see Fig. 6.3) recovery timescale indicates that the dynamics of the AFM OP, like the CDW order of Fausti et al. [26], also likely involve motion of the atomic nuclei (i.e. magnetoelastic coupling). However, in contrast to the CDW-SC competition referred to above, the dominant and subdominant orders in our system correspond not to completely different orders, but rather to different orientations of the same order. One would thus naively expect the corresponding fluctuations to exhibit more or less the same dynamics. However, as described above, this naive symmetry of the material is in fact broken at all temperatures by the internal strain; thus, it is appropriate to think of the two non-parallel AFM orientations as truly distinct orders. Importantly, it is noted in Sun and Millis [95] that small variations in the density of different fluctuations are exponentially amplified as the system relaxes, so that only a modest difference in the relevant dynamics is sufficient to favor the metastable state as the system recovers. Such asymmetric amplification of non-parallel AFM orientations thus likely forms the basis for the reorientation transition in CaMn₂Bi₂.

Evidence supporting this picture may be found by examining the time dependence of the SHG signal at short times (Supplementary material, Fig. 6.10), before the OP switches to the metastable state. In particular, on examining the initial decay rates it can be seen that the SHG signal corresponding to Fig. 6.3(a) reaches 30 % of its original value just 0.5 ps after zero delay; the equivalent drop in SHG intensity for Fig. 6.3(c) takes > 0.5 ps longer. That is, the quench dynamics associated with the metastable state are roughly twice as fast as those associated with the equilibrium state. As a result, long-wavelength fluctuations of the subdominant, metastable order experience a longer period of exponential amplification compared to the equilibrium order, which may explain the dominance of the metastable state at long times. The metastability of the final state is provided by the fact that the long-term relaxation dynamics are presumably dependent on the thermal nucleation and subsequent motion of AFM domain walls, which can be quite slow[48, 75]. Finally, we remark that while the quench dynamics described here can explain all features of our data, they also likely occur alongside a background of coherent excitations (e.g. coherent phonons, which are observable in

time-resolved reflectivity, see Supplementary material, Fig. 6.12) which can couple to the order parameter via the lattice strain (see Supplementary material, section 6.10.1). While no evidence of these excitations is apparent in our SHG data, further studies will be needed to determine the extent to which they might still be important.

6.6 Conclusion

To summarize, we have presented evidence of a magnetic reorientation transition in the antiferromagnetic semiconductor CaMn₂Bi₂ induced by above-gap optical excitation. Looking forward, we note two ingredients that seem to be most important for the transition demonstrated in this work: low symmetry, so that there are multiple energetic minima in the magnetic phase, and, presumably, some degree of magnetoelastic coupling, so that the different minima are not precisely degenerate in thermal equilibrium. Neither of these properties are unique to CaMn₂Bi₂, and analogous materials may exist with similar light-induced phenomenology. The apparently pronounced coupling between light and magnetic order in this material also invites the fascinating possibility that the magnetic order could be manipulated via additional tuning parameters like strain or current. This is a key prediction of so-called \mathcal{PT} -symmetric systems, in which inversion and time-reversal symmetries are independently broken but the product of the two is preserved[103–105]. Further investigation of these and related compounds could have far-reaching impacts for future opto-spintronic technology.

6.7 Methods

6.7.1 Material growth

Single crystals of CaMn₂Bi₂ were grown by a Bi flux method following Gibson et al. [35]. The starting materials were Ca ingot, Mn powder, and Bi powder. They were loaded into an alumina crucible in the molar ratio of Ca : Mn : Bi = 1 : 2 : 10, which was sealed in an evacuated quartz tube. The ampoule was heated to 1000°C and kept at this temperature for 11 hours before being slowly cooled to 400°C in 10 days. The excess flux was removed by a centrifuge at this temperature. The single phase

nature of the crystals was checked by powder XRD and the orientation was checked by a single-crystal x-ray diffractometer.

6.7.2 Tr-SHG measurements

The tr-SHG measurements were performed using a fast-rotating optical grating method which has been described previously[27, 37, 99]. Ultra-short (\sim 100 fs) probe pulses were sourced from a regeneratively amplified Ti:Sapphire laser operating at a repetition rate of 5 kHz. A portion of the Ti:Sapphire output was directed to an optical parametric amplifier, producing \sim 1 eV pump pulses which were delayed relative to the probe pulses with an optical delay line. The incident probe fluence was \sim 250 $\mu\text{J} \cdot \text{cm}^{-2}$, with the probe spot diameter being \sim 100 μm at the sample surface, and the pump pulses (with varying fluence) were focused to a spot roughly \sim 400 μm in diameter. The pump was normally incident to the sample surface, but the probe was incident with an angle of \sim 10°. The reflected SHG signal was collected with a photomultiplier tube, filtered with a lock-in amplifier operating at the repetition rate of the regenerative amplifier, and correlated with the rotation angle of the grating with an optical rotary encoder and homebuilt oscilloscope. To eliminate potential artifacts due to low-frequency fluctuations in the laser intensity, multiple random sweeps of the delay stage were averaged together for each dataset, and the polarizers were controlled automatically at each delay using custom polarization rotators described in Morey et al. [68].

6.7.3 PTMB measurements

The polarization-dependent optical birefringence (linear dichroism) measurements were conducted using the experimental setup detailed in Little et al. [58]. A 633 nm probe laser beam was focused onto a 5 μm spot at surface of the sample, while a 780 nm pump/heating beam was similarly focused onto the same location. To improve the signal-to-noise ratio and eliminate polarization artifacts originating from the experimental setup, the sample temperature was modulated at 2 kHz by passing the pump beam through an optical chopper. The linear dichroism signal was subsequently measured using a standard balanced photodetection scheme and a lock-in amplifier. Position-dependent measurements of optical birefringence were obtained by scanning the sample position with a piezo-

electric scanner. The dependence of the polarization rotation on the probe polarization angle was fit to a sinusoidal function at each spot, and the phase shift parameter extracted from each fit was plotted in Figs. 6.2(a) and 6.2(c). Note that the birefringence signal involves contributions from both the lattice and the magnetism, so that the angle extracted from this fit should not be identified with the angle of the AFM OP.

6.7.4 XRD measurements

XRD data (Supplementary material, Fig. 6.13) were collected at 100 K and 180 K on a Bruker-AXS X8 Kappa Duo diffractometer with $\text{I}\mu\text{S}$ micro-sources, coupled to a Photon 3 CPAD detector using Mo $\text{K}\alpha$ radiation ($\lambda = 0.710\,73\text{\AA}$), performing ϕ -and ω -scans. Reconstructed precession images of the $(0kl)$, $(h0l)$ and $(hk0)$ planes were calculated directly from the diffraction images using algorithms included in the APEX3[14] software.

6.7.5 Data availability

Data supporting the figures within this paper and other findings of this study are available from the corresponding author upon request.

6.8 Acknowledgments

The authors thank Clifford Allington, Martin Eckstein, Shiang Fang, Feng Hao, David Hsieh, Honglie Ning, Jia Xu, and Guangua Zhang for several helpful discussions. The authors also acknowledge the MIT SuperCloud and Lincoln Laboratory Supercomputing Center for providing HPC resources that have contributed to the research results reported within this paper. B.F., B.L., K.M., Z.S., B.I., T.L., and N.G. acknowledge support from the US Department of Energy, BES DMSE (data taking and analysis), and Gordon and Betty Moore Foundation's EPiQS Initiative grant GBMF9459 (instrumentation). C.L., E.D., A.L.-P., and J.O. acknowledge support from the Quantum Materials program under the Director, Office of Science, Office of Basic Energy Sciences, Materials Sciences and Engineering Division, of the US Department of Energy, Contract No. DE-AC02-05CH11231. G.A.F. gratefully acknowledges support from the NSF through the Center for Dynamics and Control of Materials: an NSF MRSEC under DMR-

1720595, NSF DMR2114825, and the Alexander von Humboldt Foundation. R.H.A.d.T., M.A., A.L., and A.A. acknowledge support from the Spanish Ministry of Science and Innovation through grants PID2019-105488GB-I00, TED2021-132074B-C32 and PID2022-PID2022-139230NB-I00, the European Commission from the MIRACLE (ID 964450), and the Basque Government through Project No. IT-1569-22.

6.9 Author contributions

B.F. and B.L. led the project, under the supervision of N.G. B.F., B.L., K.M., and A.K. designed the SHG experiments. B.F., B.L., K.M., Z.S., and A.K. performed the SHG measurements. B.F., B.L., K.M., and Z.S. analyzed the SHG data. B.F., B.L., and A.K. conceived of the project. C.L, E.D., A.L.-P., and J.O. performed and analyzed the PTMB measurements. T.K. and J.C. grew the samples and performed the resistivity measurements. B.I. and T.L. performed the time-resolved reflectivity measurements. P.M. performed and analyzed the XRD measurements. M.R.V., G.A.F., R.H.A.d.T., M.A., A.L., and A.A. developed the theoretical models and performed the calculations. B.F. wrote the paper and supplemental material, except for the supplemental theoretical discussion, which was written by M.R.V. with input from R.H.A.d.T. All authors assisted in revising the manuscript.

6.10 Supplementary Material

6.10.1 Supporting theoretical discussion

Equilibrium strain-spin coupling

To study the coupling between intrinsic strain and magnetic order in CaMn₂Bi₂, theoretical calculations were performed using the projected augmented wave method (PAW) implemented in the Vienna Ab-initio Software Package (VASP)[50, 51]. For the exchange and correlation potential, we use the Perdew-Burke-Ernzerhof form of the generalized gradient approximation (GGA), which is further corrected with the Coulomb U parameter following the GGA+U formulation of Dudarev[25]. We perform a test calculation of the partial density of states (PDOS) using the

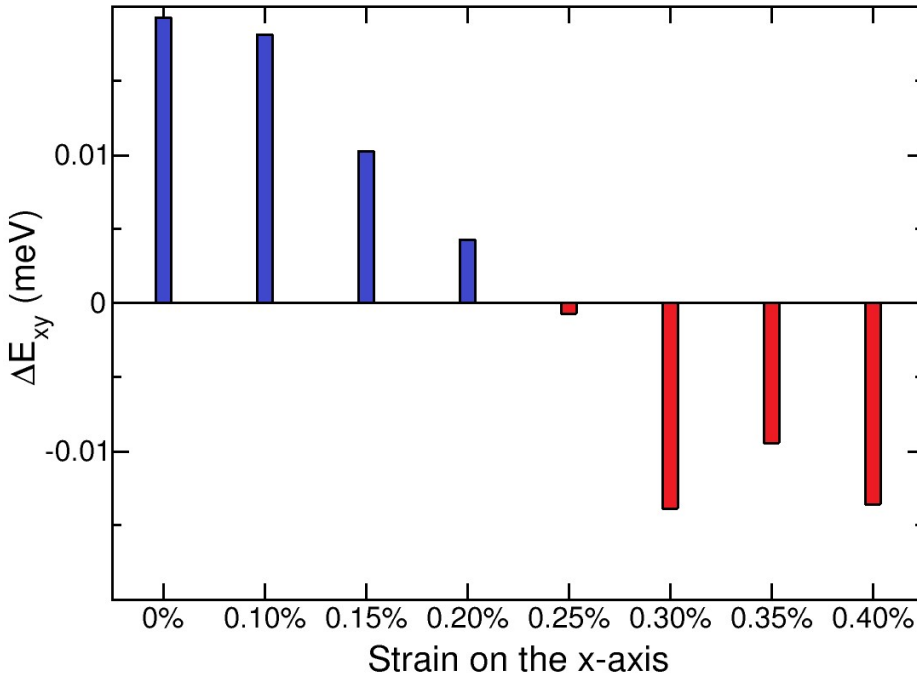


Figure 6.5: Energy difference between x and y -directions with respect to the easy axis. Blue bars indicate the x -direction for the AFM OP is preferred, and red bars indicate the y -direction for the AFM OP is preferred. Note that for strains in experiments, the difference value goes to zero, indicating a change in the in-plane magnetic moment direction.

HSE06 hybrid functional. Comparing this with the GGA and GGA+U calculations, we determine that for an improved system description, it is necessary to include the terms $U(\text{Mn}) = 4 \text{ eV}$ and $U(\text{Bi}) = 3 \text{ eV}$. All calculations were performed with a well-converged plane-wave cutoff energy of 700 eV, a gamma-centered $15 \times 15 \times 8$ Monkhorst-Pack k -point mesh, and a Fermi smearing of 20 meV. Atomic coordinates were relaxed until forces in all directions were smaller than 0.5 meV/Å. An energy convergence criterion of $1 \times 10^{-7} \text{ eV}$ is used. The atomic valence configuration for Ca, Mn and Bi are $3s^23p^64s^24p^{0.01}$, $4s^23d^5$ and $6s^26p^3$, respectively. The ground state in the trigonal unit cell shows AFM order between the Mn atoms with an energy difference of about 200 meV.

By including the spin-orbit coupling, we performed additional tests to converge the magnetocrystalline anisotropy energy (MAE) with respect to the Brillouin zone sampling. The spin-orbit coupling energetically favors certain spin orientations in the crystal. We have determined that the easy axis is the x -axis. The energy needed to align the spin out-of-plane is 2.4 meV, a value that is about a hundred times larger than the MAE difference with the y -axis, which is on the order of 0.02 meV. The MAE difference with respect to the z -axis remains constant regardless of strain. The MAE difference between the x and y directions decreases by applying strain along the x -axis, as shown in Fig. 6.5. With a strain of around 0.25%, the easy spin orientation of the crystal changes to lie along the y -axis.

Laser-induced dynamics of competing magnetic domains: “incoherent” scenario

In this section, we explore the possibility of interpreting the results of the main text based on the recent quench dynamics theory introduced by Sun and Millis [95], and Dolgirev et al. [22].

We consider the four observed domains A, B, C, and D as competing AFM orders favored in equilibrium by the local sample anisotropy, regardless of its microscopic origin. Normally, in the absence of anisotropies, the magnetism in CaMn_2Bi_2 would be described by model-G [42]. However, the presence of anisotropies, indicated by the existence of only four domains out of the expected twelve configurations due to symmetry, suggests that total magnetization is not conserved. Thus, the relaxational behavior of type A studied in detail in [22, 95], is applicable. The corresponding relaxational time-dependent-Ginzburg-Landau model is given by $\frac{1}{\gamma_i} \partial_t \psi_i(\mathbf{r}, t) = -\frac{\delta F(t)}{\delta \psi_i(\mathbf{r}, t)} + \eta_i(\mathbf{r}, t)$, where ψ_i corresponds to the staggered magnetization in domain $i = A, B, C$, and D . γ_i and η_i are the i -th domain relaxation rate and Gaussian white noise source. The free-energy functional follows the form of Equation (2) in [95], with interactions among the domains, $F = \int d^D \mathbf{r} (\sum_i f_i + f_c)$, $f_i = -\alpha_i \psi_i^2 + (\xi_{i0} \nabla \psi_i)^2 + \psi_i^4$, and $f_c = \psi_C^2 (c_{AC} \psi_A^2 + c_{CB} \psi_B^2) + \psi_D^2 (c_{AD} \psi_A^2 + c_{BD} \psi_B^2)$. ξ_{i0} is the bare coherence lengths, and $\alpha_i = \alpha_i(t)$ is a time-dependent dimensionless coefficient influenced by the laser pump excitation’s temperature profile.

During the laser pump excitation, characterized by a high temperature and $\alpha_i(t) < 0$, and until $\alpha_i(t) = 0$, the mean-field order parameters have small values, and the dynamics are governed by order-parameter

fluctuations. Subsequently, the fluctuations grow exponentially, leading to a metastable state determined by the fastest-relaxing domain. In our experiment, domain A always goes to A, domain B always goes to B, while domain C and D can go to either A or B. Assuming that the coefficients α_i in equilibrium are equal across the four domains, this observation aligns with the theory prediction if $\gamma_{A/B} > \gamma_{C/D}$ and $\gamma_A \approx \gamma_B$.

Laser-induced dynamics of competing magnetic domains: “coherent” scenario

Group theory aspects of the magnetic order

CaMn₂Bi₂ belongs to the trigonal symmorphic space group $P\bar{3}m1$ (No. 164) [35]. The Wyckoff positions of the atoms are Bi 2d, Mn 2d, and Ca 1a. The Ca atoms form a triangular lattice on the top and bottom of the Bi and Mn atoms, while Mn and Bi form buckled hexagonal lattices. At the Γ point, the point group is $\bar{3}m$, which possess twelve symmetry operations:

$$\begin{aligned}\{1|0\}: (x, y, z) &\rightarrow (x, y, z) \\ \{3_{001}^+|0\}: (x, y, z) &\rightarrow (-y, x - y, z) \\ \{3_{001}^-|0\}: (x, y, z) &\rightarrow (-x + y, -x, z) \\ \{2_{110}|0\}: (x, y, z) &\rightarrow (y, x, -z) \\ \{2_{100}|0\}: (x, y, z) &\rightarrow (x - y, -y, -z) \\ \{2_{010}|0\}: (x, y, z) &\rightarrow (-x, -x + y, -z)\end{aligned}$$

plus their composition with inversion symmetry $\{-1|0\} : (x, y, z) \rightarrow (-x, -y, -z)$. With this lattice information above the magnetic transition temperature, we proceed with a group theory analysis of the possible magnetic orders with the aid of ISOTROPY [93]. In CaMn₂Bi₂, the magnetic transition is not accompanied by a lattice deformation, such that the magnetic unit cell coincides with the chemical unit cell. Therefore, the magnetic order is associated with Γ point irreducible representations. The magnetic subgroups resulting from the onset of all possible Γ point irreducible representations are shown in table 6.1. The A_{2g} and A_{1u} irreducible representations (irreps) correspond to out-of-plane ferromagnetic and antiferromagnetic order, respectively. The two-dimensional irreps E_g and E_u induce in-plane magnetic and AFM order,

respectively. A general direction of the OP is associated with the magnetic subgroup $P\bar{1}'$, which corresponds to the experimental magnetic space group [35]. Notice that special directions of the OP lead to magnetic structures with higher symmetry and corresponding magnetic space groups $C2/m'$ or $C2'/m$.

Finally, noting that each of the twelve symmetry operations listed above leads to a different AFM OP direction (as the real OP does not lie along any of the special directions), the free energy surface in equilibrium should have exactly twelve minima in the absence of strain, as referenced in the text.

IR	Subgroup	Direction
$\Gamma_1^+ (A_{1g})$	(164.85) $P\bar{3}m1$	P1 (a)
$\Gamma_2^+ (A_{2g})$	(164.89) $P\bar{3}m'1$	P1 (a)
$\Gamma_3^+ (E_g)$	(12.58) $C2/m$	P1 (a,-1.732a)
	(12.62) $C2'/m'$	P2 (a,0.577a)
	(2.4) $P\bar{1}$	C1 (a,b)
$\Gamma_1^- (A_{1u})$	(164.88) $P\bar{3}'m'1$	P1 (a)
$\Gamma_2^- (A_{2u})$	(164.87) $P\bar{3}'m1$	P1 (a)
$\Gamma_3^- (E_u)$	(12.60) $C2'/m$	P1 (a,-1.732a)
	(12.61) $C2/m'$	P2 (a,0.577a)
	(2.6) $P\bar{1}'$	C1 (a,b)

Table 6.1: Subgroups obtained by the onset of magnetic order of a given irreducible representation. The columns indicate the irreducible representations, the magnetic group, and the OP direction in the representation space.

Free energy model

Now we construct a free energy model considering magnetic order, strain, and phonon modes. As discussed in the previous section, the in-plane AFM groundstate corresponds to the magnetic irrep Γ_3^- , with general in-plane OP directions L_1, L_2 . The parent cell supports strain mode distortions with irrep Γ_1^+ and Γ_3^+ . We consider a two component Γ_3^+ mode with components $\epsilon_{xx} = -\epsilon_{yy}$ (ϵ_1) and ϵ_{xy} (ϵ_2). Finally, the phonon mode (Q) is assumed to be totally symmetric. The free energy, to fourth order, then takes the form $\mathcal{F} = \mathcal{F}_M + \mathcal{F}_S + \mathcal{F}_C + \mathcal{F}_P$,

with

$$\mathcal{F}_M = (T/T_c - 1)L_1^2 + (T/T_c - 1)L_2^2 + (L_1^2 + L_2^2)^2, \quad (6.1)$$

$$\mathcal{F}_S = \frac{1}{2}(e_1^2 + e_2^2) + e_1^3 - e_1 e_2^2 + (e_1^2 + e_2^2)^2, \quad (6.2)$$

$$\mathcal{F}_P = \frac{\omega^2}{2}Q^2 + Q^3 + Q^4, \quad (6.3)$$

$$\begin{aligned} \mathcal{F}_C = & (L_1^2 - L_2^2)e_1 - L_1 L_2 e_2 + (L_1^2 + L_2^2)(e_1^2 + e_2^2) \\ & + L_1 L_2 e_1 e_2 + (L_1^2 + L_2^2)(Q + Q^2) + (e_1^2 + e_2^2)(Q + Q^2) \\ & + (L_1^2 - L_2^2)e_1 Q - L_1 L_2 e_2 Q + e_1^3 Q - e_1 e_2^2 Q. \end{aligned} \quad (6.4)$$

Each of the terms in the model \mathcal{F} is preceded by a constant whose sign and absolute value cannot be determined within group theory and are sample-dependent. The magnetic term, \mathcal{F}_M , could include anisotropic terms (due to spin-orbit coupling or single-ion anisotropies, for example), which we omit as the simplest model presented can describe the phenomenology in the experiment.

We assume that the laser excites the totally-symmetric phonon coherently via a displacive excitation mechanics [111]. The laser-phonon coupling term is given by $\mathcal{F}_l = E_0 \eta(t)Q$, where $\eta(t) = \kappa \int_0^\infty g(t - \tau) e^{-\beta\tau} d\tau$, and $g(t)$ is the laser pulse shape, and β is a parameter associated with rate of electronic relaxation to the groundstate. The differential equations governing the system can be obtained by taking the variation of the $\mathcal{F} + \mathcal{F}_l$ potential with respect to the AFM OPs, strain, and phonon. For the results in the main text, we include phenomenological damping. The equations of motion are $-\delta(\mathcal{F} + \mathcal{F}_l)/\delta\chi_i = \partial_t^2\chi_i(t) + \gamma_i\partial_t\chi_i(t)$, where $\chi = \{Q, L_1, L_2\}$ and γ_i is the damping coefficient.

Phonon coupling effect.

First, we assume that there is no strain in the sample. The only term linking the AFM OP to the time-dependent phonon is $(L_1^2 + L_2^2)(Q + Q^2)$. We find that this term can lead to flips of L_1 and L_2 by 180 degrees for long-enough laser pulses. Fig. 6.6(a) shows the phonon dynamics following photo-excitation with a 1eV pulse and duration $\tau = 1.1$ ps. The phonon frequency was assumed to be $\omega/(2\pi) = 3$ THz, and the initial temperature is $T = 0$.

Strain

The presence of strain mediates coupling terms between the phonon and the AFM OP that can lead to orientations absent in equilibrium. In particular, the coupling term $L_1 L_2 e_2 Q$ induces a solution where the components L_1, L_2 oscillate around a position distinct to the initial configuration and to 180-degree flips. We consider a pulse with duration $\tau = 1.2$ ps, phonon frequency $\omega/(2\pi) = 3$ THz, $T = 0$, and strains $\epsilon_1 = 0.01, \epsilon_2 = 0.05$. The long-time average of $L_2(t)$ acquires values comparable with $L_1(t)$, as seen in Fig. 6.7(b).

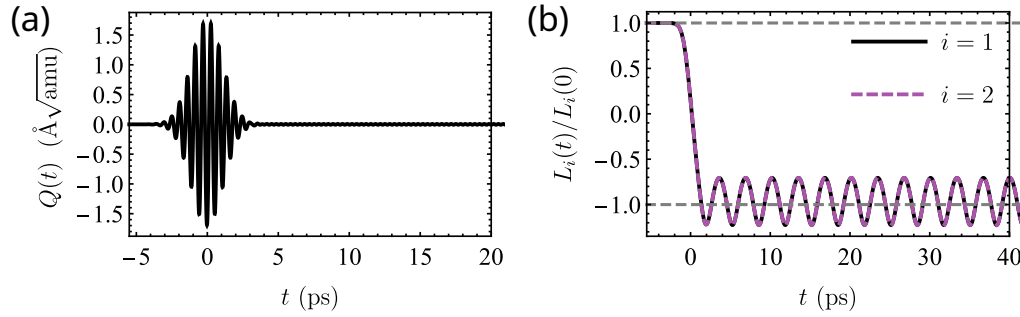


Figure 6.6: (a) Phonon mode and (b) AFM OP following photo-excitation with coupling $(L_1^2 + L_2^2)(Q + Q^2)$.

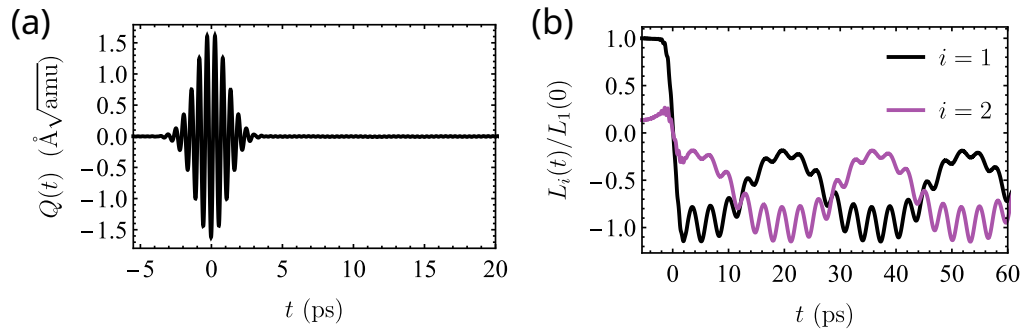


Figure 6.7: (a) Phonon mode and (b) AFM OP following photo-excitation with coupling $L_1 L_2 e_2 Q$.

6.10.2 Nonviability of secondary order parameter in describing the RA-SHG data

Using a combination of PTMB and RA-SHG, we argue in the main text that, in equilibrium, the magnetism in CaMn_2Bi_2 that we observe is described by a spatial distribution of four domains A , B , C , and D , for which the order parameters satisfy the relations $l_A = -l_B$, $l_C = -l_D$, and $l_C = R(l_A)$, where R is an element of the high-temperature point group $\bar{3}m$. In this scenario, the contrast in SHG between e.g. l_A and l_B comes from the fact that there can be two contributions to the RA-SHG signal which interfere with each other and transform differently as $l_A \rightarrow l_B$. That is, we can write

$$I_{\text{SHG}} \propto |e_i^{\text{out}} \chi_{ijk} e_j^{\text{in}} e_k^{\text{in}}|^2, \quad (6.5)$$

where

$$\chi_{ijk} \equiv \chi_{ijk}^\alpha + \chi_{ijk}^\beta, \quad (6.6)$$

$$\begin{aligned} T(\chi_{ijk}^\alpha) &= -\chi_{ijk}^\alpha, \\ T(\chi_{ijk}^\beta) &= \chi_{ijk}^\beta, \end{aligned} \quad (6.7)$$

T is the time-reversal operator which takes $l_A \rightarrow -l_A = l_B$, and e^{in} and e^{out} are unit vectors in the direction of the polarization of the incoming and outgoing electric fields, respectively.

An important question thus arises: what is the origin of the two sources χ^α and χ^β ? The simplest explanation is that both contributions are due to the AFM OP; the relations in Eq. 6.7 are then permitted below T_c , where time-reversal symmetry is broken and so χ_{ijk} can, in general, have parts which transform as both even and odd under time-reversal. However, an alternative interpretation is that there are in fact two OPs l and g , with g being e.g. some structural OP, so that, e.g.

$$\begin{aligned} \chi^C &\propto l + g, \text{ and} \\ \chi^D &\propto l + Rg, \end{aligned} \quad (6.8)$$

for some $R \in \bar{3}m$.

In this interpretation, alternative descriptions of the time-resolved results, involving e.g. a melting of g while the l stays fixed, may explain Fig. 6.3, but not imply a reorientation of l as we claim in the main text. However, we argue that such an interpretation is not a viable description of our results, both in and out of equilibrium. This can be understood by considering the fact that the RA-SHG pattern in Fig. 6.2(f) has nodes at $\phi = 0$ and $\phi = \pi$ for all temperatures below T_c (see Fig. 6.20). In the case $Rg = -g$, this suggests that, if there are

indeed two independent order parameters contributing to the RA-SHG pattern, their amplitudes must exactly cancel for all $T < T_c$. This is unlikely as the two independent order parameters should in general depend differently on temperature. Moreover, the case $Rg \neq -g$ is difficult to reconcile in light of the result that the PTMB signal is invariant under thermal cycling. In nonequilibrium, any scenario involving the melting of one OP while the other stays fixed must also be reconciled with the observation that the nodes in Fig. 6.3(c) in the initial state (before $t = 0$) become peaks in the final state.

Furthermore, the above interpretation must also explain how the final state of the transition seems to differ from sample to sample (as explained in the main text; see Figs. 6.18 and 6.19), as well as how the RA-SHG is poled in equilibrium to only two of many different degenerate states. Both of these facts fall out naturally from the assignment presented in the main text.

Together with the lack of a change in the XRD across T_c (see Fig. 6.13), the above considerations suggest that the scenario presented in the main text, which neatly describes the data both in and out of equilibrium, is the most likely. Future studies will be required to completely truly rule out all alternative scenarios.

6.10.3 Fits to susceptibility tensors

In the text, it was remarked that the OP assignment depicted in Figs. 6.2–6.3 was consistent with the SHG susceptibility tensors extracted by fitting the RA-SHG patterns. In this section, we state how this fitting was performed.

Before that discussion, however, we must mention one important point about the predictive power of these fits. Since the low-temperature point group of CaMn₂Bi₂ is $\bar{1}'$, the relevant susceptibility tensors are entirely unconstrained and the cost function to be minimized may involve upward of 36 free parameters. Thus, in principle, many combinations of parameters may fit the data appropriately, thereby limiting the extent to which the SHG fits can be used to draw conclusions about the underlying state. One must look to other arguments, e.g. involving PTMB, to draw useful conclusions about the data, as was done in the text. However, once a conclusion has been made, it can at least be checked that a set of fitting parameters *does* exist that is consistent with the conclusion and with the data. This is the goal of this section.

The OP assignment discussed in the text involves two parts. In the first part, the equilibrium SHG in the four domains of Fig. 6.2 is assigned to four different OP directions, in which the SHG on consecutive cooldowns on a single spot is due to 180° AFM configurations, and adjacent spots have a relative angle between them. As argued in the text, since the 180° domains have different RA-SHG patterns, there are most likely two contributions to the SHG adding coherently

to give an interference term, as observed in other magnetic systems[29, 31, 32]. Designating the four configurations as A , B , C , and D (for Fig. 6.2(d), Fig. 6.2(e), Fig. 6.2(f), and Fig. 6.2(g), respectively), we thus have

$$\begin{aligned}\chi_{ijk}^A &= \chi_{ijk}^\alpha + \chi_{ijk}^\beta \\ \chi_{ijk}^B &= -\chi_{ijk}^\alpha + \chi_{ijk}^\beta \\ \chi_{ijk}^C &= R(\chi_{ijk}^\alpha + \chi_{ijk}^\beta) \\ \chi_{ijk}^D &= R(-\chi_{ijk}^\alpha + \chi_{ijk}^\beta),\end{aligned}\tag{6.9}$$

where χ^α is the susceptibility tensor related to the magnetic order[32], χ^β is the susceptibility tensor corresponding to the secondary component discussed above, and $R(\cdot)$ refers to an operation by some element R of the high-temperature point group ($\bar{3}m$), i.e.

$$R(\chi_{ijk}) \equiv R_{il}R_{jm}R_{kn}\chi_{lmn}.$$

In the time-resolved case, 6.9 should hold before zero delay, and a similar set of equations should hold after zero delay in the final state:

$$\begin{aligned}\chi_{ijk}^{A'} &= \alpha\chi_{ijk}^\alpha + \chi_{ijk}^\beta \\ \chi_{ijk}^{B'} &= -\alpha\chi_{ijk}^\alpha + \chi_{ijk}^\beta \\ \chi_{ijk}^{C'} &= \alpha\chi_{ijk}^\alpha + \chi_{ijk}^\beta \\ \chi_{ijk}^{D'} &= \alpha\chi_{ijk}^\alpha + \chi_{ijk}^\beta.\end{aligned}\tag{6.10}$$

Here, α is an overall factor to account for the fact that the magnitude of the OP may change due to heating following the transition. We also allow a relative scale (close to unity) between A / B / A' / B' and C / D / C' / D' to account for the fact that these are taken on different spots on the sample.

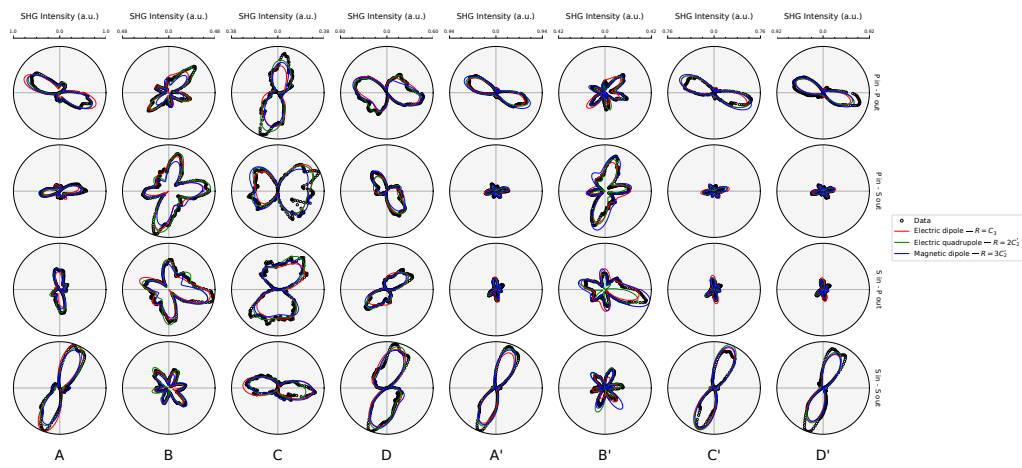


Figure 6.8: Fits to the RA-SHG pattern in the four domains of Fig. 6.2 2.0 ps before (A, B, C, D) and ~ 40 ps after (A', B', C', D') zero delay. Data is represented by black circles; solid lines are fits to Eqs. 6.5 and 6.6 with χ^β denoted in the legend.

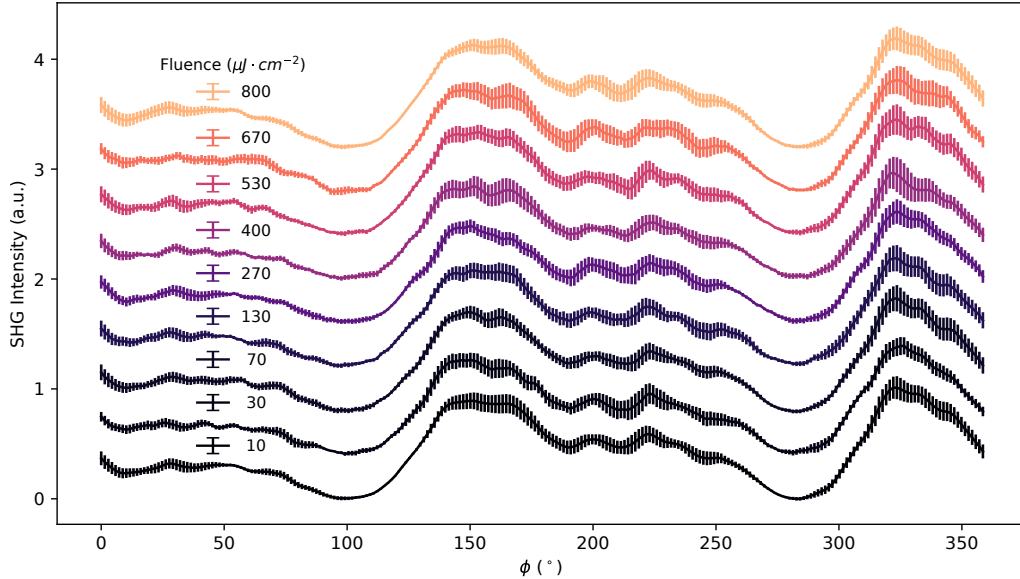


Figure 6.9: RA-SHG results of Fig. 6.11 depicted with estimated errorbars (see text).

For χ_{ijk}^α , we use the totally asymmetric complex electric dipole SHG tensor in the point group $\bar{1}'$, which has 36 independent elements. In the language of Birss [10], this would be referred to as a *c*-type tensor and should have purely imaginary components; however, in the presence of dispersion or dissipation, complex components are also allowed. For χ_{ijk}^β , many options are possible, including an *i*-type electric dipole component, electric quadrupole component, or magnetic dipole component, each of which may couple with the AFM OP. With each of these options for χ^α and χ^β , we fit the RA-SHG data at $\Delta t = -2$ ps and at long times ($\Delta t \approx 40$ ps). It is found that all possibilities for χ^β produce an appropriate fit to the data (see Fig. 6.8).

6.10.4 Error bar estimation for Fig. 6.11

The errorbars in Fig. 6.9 are ultimately due to uncertainty in the value of the SHG intensity at each angle ϕ . When these angles are integrated over, the associated uncertainties in the SHG intensity are summed in quadrature. To extract the uncertainties in the SHG intensity as a function of angle is a somewhat difficult process, as these uncertainties are largely systematic rather than statistical. Indeed, the RA-SHG pattern should in general be a smooth function of ϕ ; however,

it is seen (e.g. Fig. 6.3(d)) that the RA-SHG patterns are not necessarily smooth. We therefore estimate the size of the errorbars using more heuristic methods, which, while imprecise, should at least give a rough approximation to the true uncertainty.

These heuristic errorbars in the SHG intensity are found by estimating the size of the variations in the RA-SHG pattern compared to a smoothed approximation (approximated with an $N = 6$ FFT filter). The errorbars computed this way are shown in Fig. 6.9.

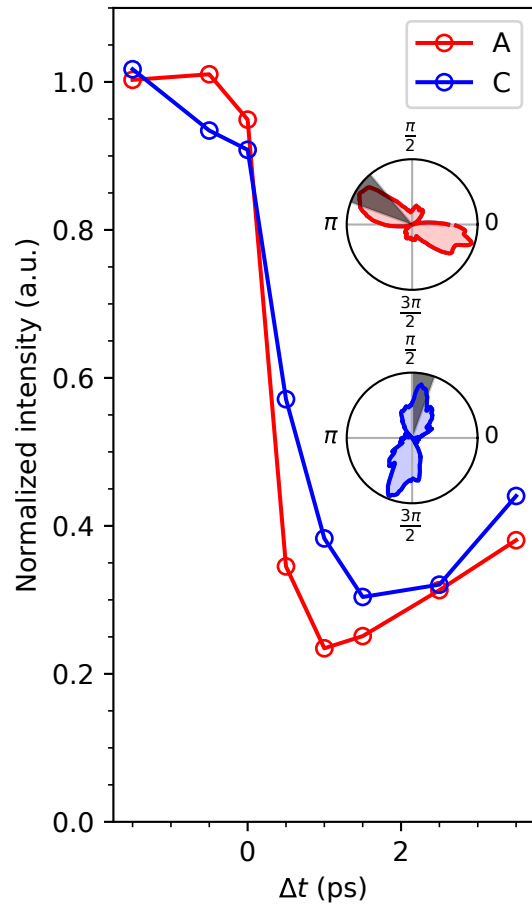


Figure 6.10: Integrated SHG intensity as a function of time corresponding to Fig. 6.4(a) (A, red) and Fig. 6.4(c) (C, blue). Insets show the equilibrium SHG patterns in the $P_{in}P_{out}$ polarization combination for the two domains, with the integration region indicated in gray. The y -axis normalization for either domain is defined such that the average signal before zero delay equal to 1.0.

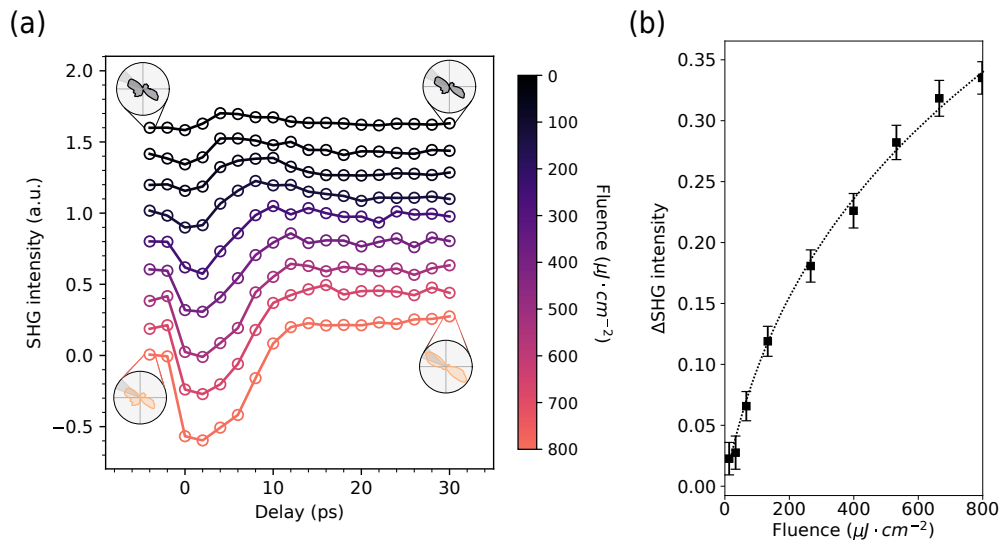


Figure 6.11: (a) Integrated SHG intensity for a representative AFM domain as a function of delay and pump fluence. Insets show the initial (left) and final (right) states at high (bottom) and low (top) pump fluences, as well as the integration region (indicated by the shaded area). (b) Difference between the intensity of the integration region specified in 6.11(a) at long times (averaged from $\Delta t = 40$ to $\Delta t = 50$ ps) and the intensity before zero delay (averaged from $\Delta t = -4$ to $\Delta t = -2$ ps). Dashed line is a guide to the eye.

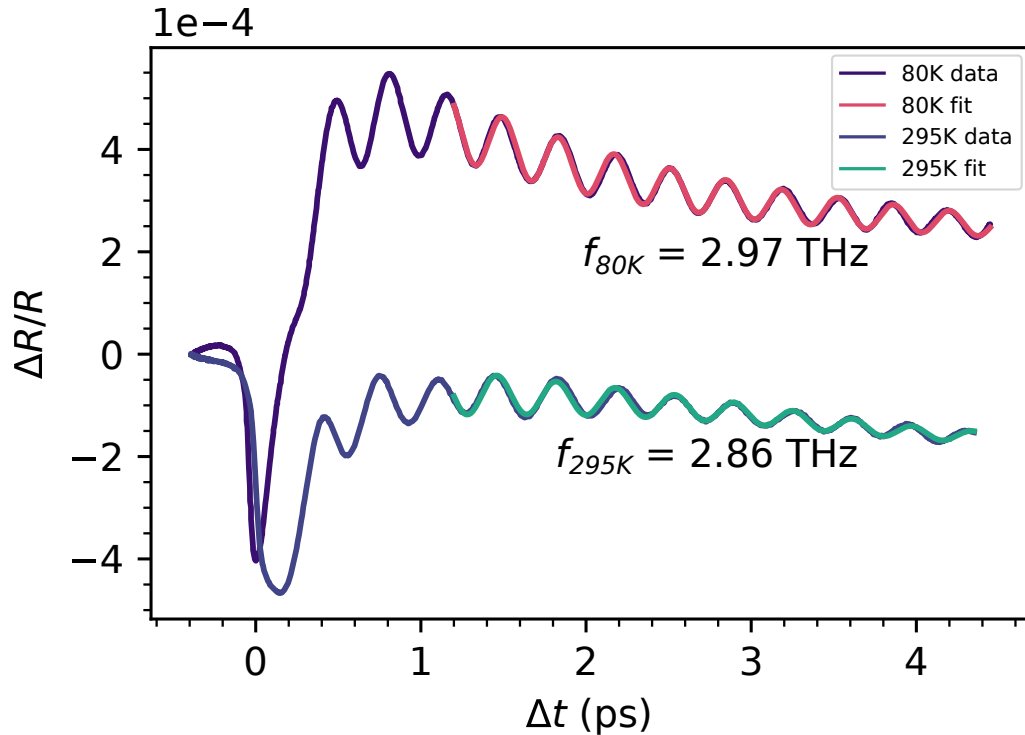


Figure 6.12: Time-resolved reflectivity obtained from CaMn_2Bi_2 at 80 K and 295 K. The pump and probe wavelengths were both 800 nm, the pulse width was 28 fs, and the pump and probe fluences were 10 and $1 \mu\text{J} \cdot \text{cm}^{-2}$, respectively. The data is windowed after the initial transients and then fit to a damped harmonic oscillator plus a polynomial background.

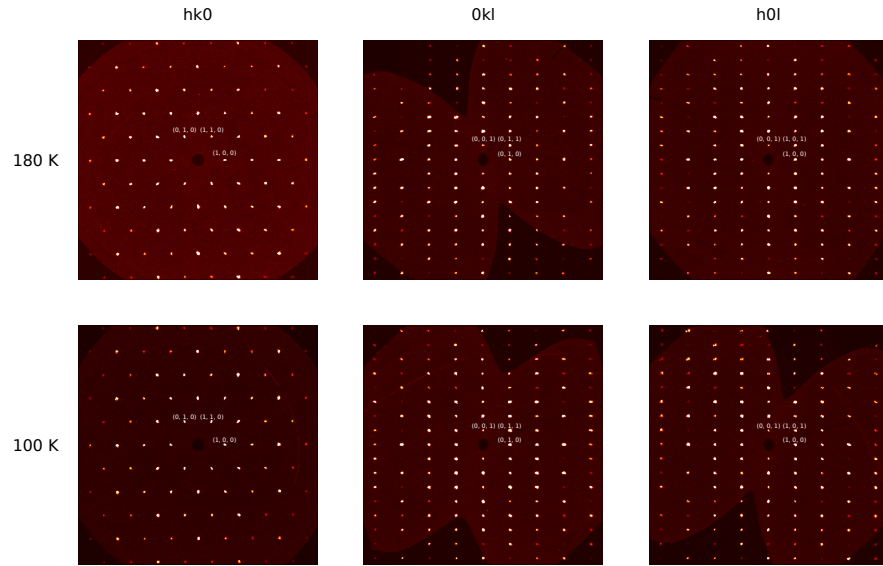


Figure 6.13: Single-crystal XRD precession images obtained from CaMn_2Bi_2 . The high temperature refinement is in agreement with previous reports[35]. No change in the crystal structure is observed across $T_c = 150 \text{ K}$.

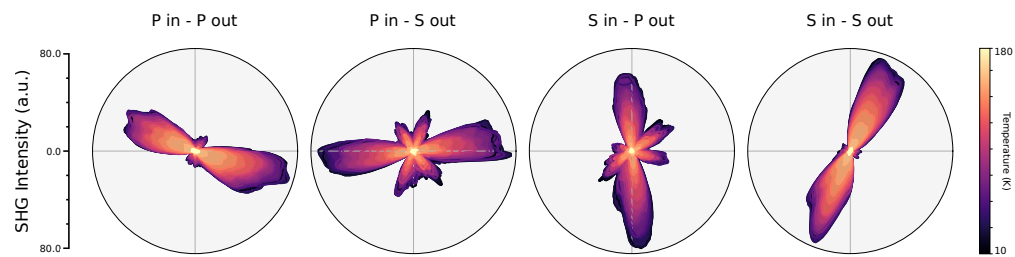


Figure 6.14: RA-SHG results of Fig. 6.1 depicted in all four polarization channels ($P_{\text{in}}P_{\text{out}}$, $P_{\text{in}}S_{\text{out}}$, $S_{\text{in}}P_{\text{out}}$, and $S_{\text{in}}S_{\text{out}}$)

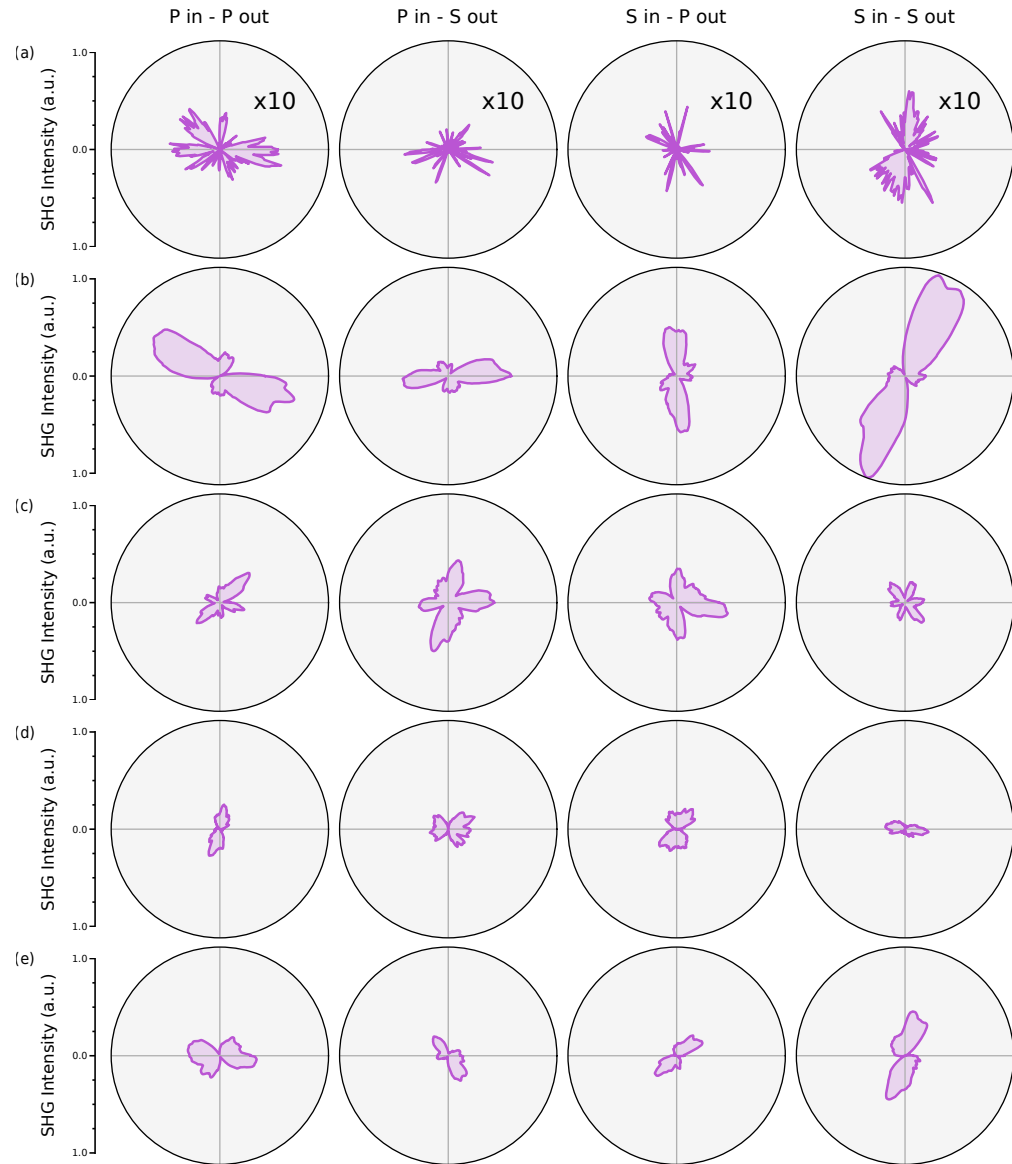


Figure 6.15: (a) (b) (c) (d) (e) RA-SHG results of Figs. 6.2(b) and 6.2(d)–g) depicted in all four polarization channels ($P_{\text{in}}P_{\text{out}}$, $P_{\text{in}}S_{\text{out}}$, $S_{\text{in}}P_{\text{out}}$, and $S_{\text{in}}S_{\text{out}}$).

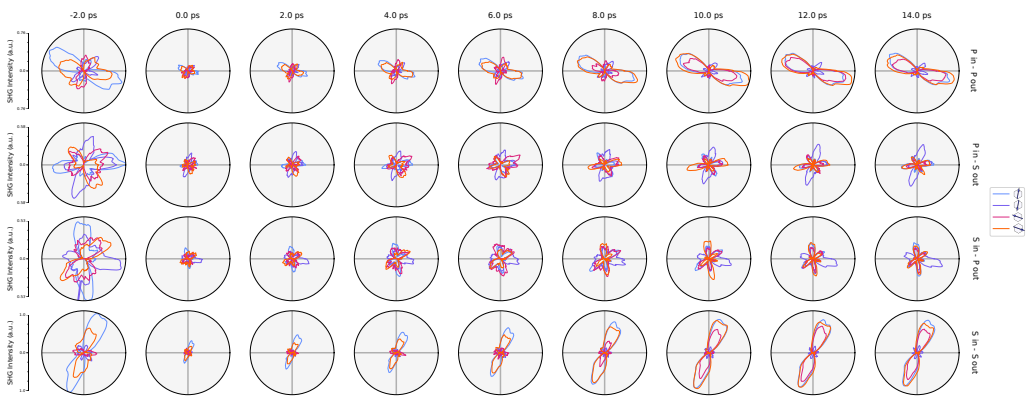


Figure 6.16: RA-SHG results of Fig. 6.3 depicted in all four polarization channels ($P_{\text{in}}P_{\text{out}}$, $P_{\text{in}}S_{\text{out}}$, $S_{\text{in}}P_{\text{out}}$, and $S_{\text{in}}S_{\text{out}}$). The pump fluence is set to $\sim 600 \mu\text{J} \cdot \text{cm}^{-2}$.

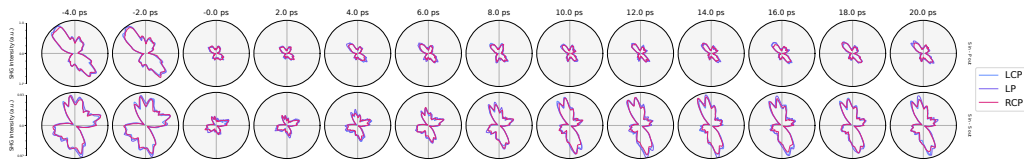


Figure 6.17: RA-SHG results in a representative domain as a function of time for different pump polarization states (left circularly- (LCP), right circularly- (RCP), and linearly-polarized). The pump fluence is set to $\sim 600 \mu\text{J} \cdot \text{cm}^{-2}$.

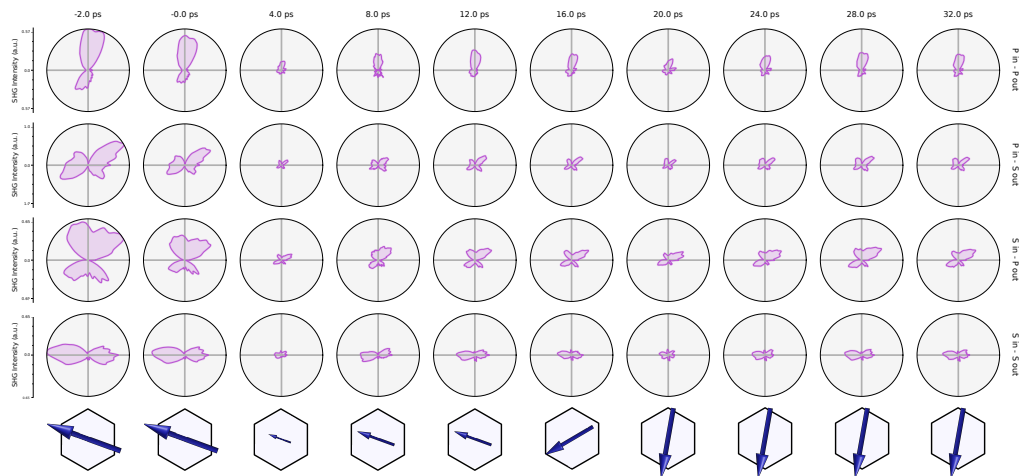


Figure 6.18: RA-SHG snapshots showing a transition to the state opposite to Figs. 6.3(c–d). The pump fluence is set to $\sim 600 \mu\text{J} \cdot \text{cm}^{-2}$. The last row depicts the corresponding value of the AFM OP proposed in the text, relative to the hexagonal crystallographic motif. The schematic representations beneath the RA-SHG plots are for illustration purposes only and the depicted angles are not quantitatively verified.

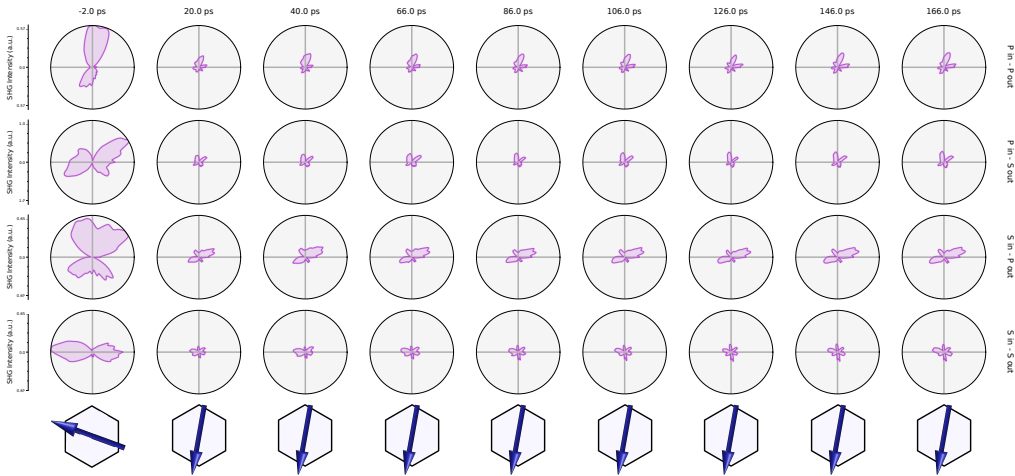


Figure 6.19: RA-SHG results in the same domain as Fig. 6.18 plotted out to longer times. The pump fluence is set to $\sim 600 \mu\text{J} \cdot \text{cm}^{-2}$. The last row depicts the corresponding value of the AFM OP proposed in the text, relative to the hexagonal crystallographic motif. The schematic representations beneath the RA-SHG plots are for illustration purposes only and the depicted angles are not quantitatively verified.

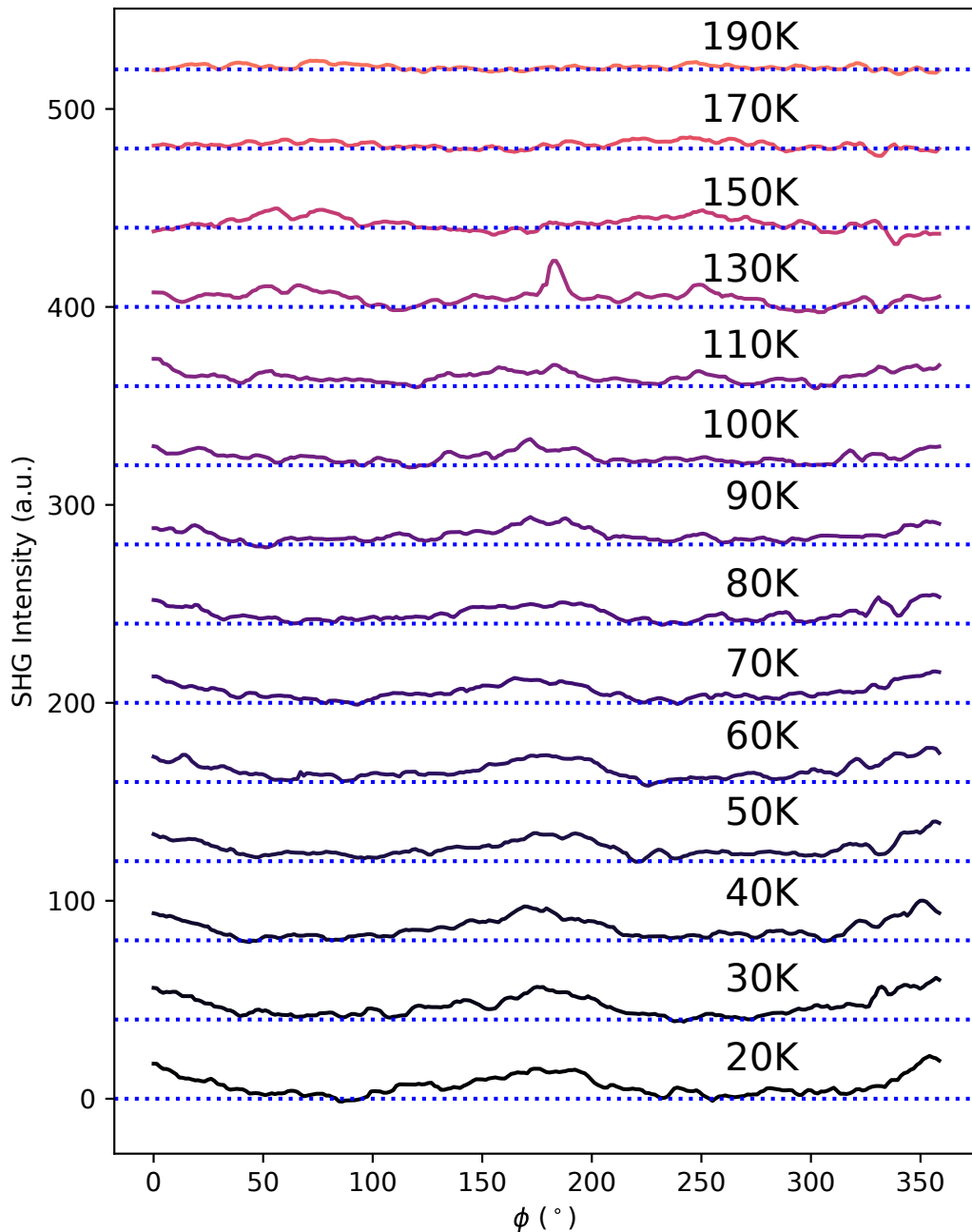


Figure 6.20: SHG intensity in the same domain as Fig. 6.2(f) as a function of temperature.

Chapter Seven

Amplitude-mode electromagnon in the XXZ chain CuBr₂

Chapter Eight

Concluding remarks

*

Bibliography

- [1] D. Afanasiev, J. R. Hortensius, B. A. Ivanov, A. Sasani, E. Bousquet, Y. M. Blanter, R. V. Mikhaylovskiy, A. V. Kimel, and A. D. Caviglia.
Ultrafast control of magnetic interactions via light-driven phonons.
Nat. Mater., 20(5):607–611, May 2021.
doi: 10.1038/s41563-021-00922-7.
- [2] A. Alexandradinata, N. P. Armitage, Andrey Baydin, Wenli Bi, Yue Cao, Hitesh J. Changlani, Eli Chertkov, Eduardo H. da Silva Neto, Luca Delacretaz, Ismail El Baggari, G. M. Ferguson, William J. Gannon, Sayed Ali Akbar Ghorashi, Berit H. Goodge, Olga Goulko, G. Grisonnanche, Alannah Hallas, Ian M. Hayes, Yu He, Edwin W. Huang, Anshul Kogar, Divine Kumah, Jong Yeon Lee, A. Legros, Fahad Mahmood, Yulia Maximenko, Nick Pellatz, Hryhoriy Polshyn, Tarapada Sarkar, Allen Scheie, Kyle L. Seyler, Zhenzhong Shi, Brian Skinner, Lucia Steinke, K. Thirunavukkuarasu, Thaís Victa Trevisan, Michael Vogl, Pavel A. Volkov, Yao Wang, Yishu Wang, Di Wei, Kaya Wei, Shuolong Yang, Xian Zhang, Ya-Hui Zhang, Liuyan Zhao, and Alfred Zong.
The Future of the Correlated Electron Problem, July 2022.
arXiv:2010.00584 [cond-mat].
- [3] N. Argibay, J.A. Bares, and W.G. Sawyer.
Asymmetric wear behavior of self-mated copper fiber brush and slip-ring sliding electrical contacts in a humid carbon dioxide environment.
Wear, 268(3-4):455–463, February 2010.
doi: 10.1016/j.wear.2009.08.036.
- [4] George Edward Bacon.
X-ray and Neutron Diffraction.
Elsevier, 1966.
- [5] D. N. Basov, Richard D. Averitt, Dirk van der Marel, Martin Dressel, and Kristjan Haule.

- Electrodynamics of correlated electron materials.
Rev. Mod. Phys., 83(2):471–541, June 2011.
doi: 10.1103/RevModPhys.83.471.
- [6] D. N. Basov, R. D. Averitt, and D. Hsieh.
Towards properties on demand in quantum materials.
Nature Mater., 16(11):1077–1088, November 2017.
doi: 10.1038/nmat5017.
- [7] Klaus-Dieter Bauer and Kurt Hingerl.
Bulk quadrupole contribution to second harmonic generation from classical oscillator model in silicon.
Opt. Express, 25(22):26567, October 2017.
doi: 10.1364/OE.25.026567.
- [8] VI Belinicher and BI Sturman.
The photogalvanic effect in media lacking a center of symmetry.
Soviet Physics Uspekhi, 23(3):199, 1980.
- [9] G. Berkovic, Y. R. Shen, G. Marowsky, and R. Steinhoff.
Interference between second-harmonic generation from a substrate and from an adsorbate layer.
J. Opt. Soc. Am. B, 6(2):205–208, Feb 1989.
doi: 10.1364/JOSAB.6.000205.
- [10] Robert R. Birss.
Symmetry and Magnetism.
North-Holland Pub. Co., 1964.
- [11] N. Bloembergen, R. K. Chang, S. S. Jha, and C. H. Lee.
Optical Second-Harmonic Generation in Reflection from Media with Inversion Symmetry.
Physical Review, 174(3):813–822, October 1968.
doi: 10.1103/PhysRev.174.813.
- [12] M. Bovet, D. Popović, F. Clerc, C. Koitzsch, U. Probst, E. Bucher, H. Berger, D. Naumović, and P. Aebi.
Pseudogapped Fermi surfaces of 1 T - TaS 2 and 1 T - TaSe 2 : A charge density wave effect.
Physical Review B, 69(12), March 2004.
doi: 10.1103/PhysRevB.69.125117.

- [13] Robert Boyd.
Nonlinear Optics.
Academic Press, third edition, mar 2008.
- [14] Bruker.
APEX3.
Bruker-AXS Inc., Madison, Wisconsin, USA, 2022.
- [15] Branton J. Campbell, Harold T. Stokes, David E. Tanner, and Dorian M. Hatch.
ISODISPLACE : a web-based tool for exploring structural distortions.
J Appl Crystallogr, 39(4):607–614, August 2006.
doi: 10.1107/S0021889806014075.
- [16] Wikipedia contributors.
List of space groups — Wikipedia, the free encyclopedia, 2024.
[Online; accessed 06-March-2024].
- [17] Kevin A. Cremin, Jingdi Zhang, Christopher C. Homes, G. D. Gu, Zhiyuan Sun, Michael M. Fogler, Andrew J. Millis, D. N. Basov, and Richard D. Averitt.
Photoenhanced metastable c-axis electrodynamics in stripe-ordered cuprate $\text{La}_{1.885}\text{Ba}_{0.115}\text{CuO}_4$.
Proc. Natl. Acad. Sci. U.S.A., 116(40):19875–19879, October 2019.
doi: 10.1073/pnas.1908368116.
- [18] N.A.C. Cressie.
Statistics for Spatial Data.
A Wiley-interscience publication. J. Wiley, 1991.
- [19] Pierre Curie.
Sur la symétrie dans les phénomènes physiques, symétrie d'un champ électrique et d'un champ magnétique.
J. Phys. Theor. Appl., 3(1):393–415, 1894.
- [20] Elbio Dagotto.
Complexity in Strongly Correlated Electronic Systems.
Science, 309(5732):257–262, July 2005.
doi: 10.1126/science.1107559.
- [21] F.M. Dekking, C. Kraaikamp, H.P. Lopuhaä, and L.E. Meester.
A Modern Introduction to Probability and Statistics: Understanding Why and How.

- Springer Texts in Statistics. Springer London, 2006.
- [22] Pavel E. Dolgirev, Marios H. Michael, Alfred Zong, Nuh Gedik, and Eugene Demler.
Self-similar dynamics of order parameter fluctuations in pump-probe experiments.
Phys. Rev. B, 101(17):174306, May 2020.
doi: 10.1103/PhysRevB.101.174306.
- [23] Douglas L Dorset.
Structural electron crystallography.
Springer Science & Business Media, 2013.
- [24] J. Ducuing and N. Bloembergen.
Observation of Reflected Light Harmonics at the Boundary of Piezoelectric Crystals.
Phys. Rev. Lett., 10(11):474–476, June 1963.
doi: 10.1103/PhysRevLett.10.474.
- [25] S. L. Dudarev, G. A. Botton, S. Y. Savrasov, C. J. Humphreys, and A. P. Sutton.
Electron-energy-loss spectra and the structural stability of nickel oxide: An LSDA+U study.
Phys. Rev. B, 57:1505–1509, 1998.
doi: 10.1103/PhysRevB.57.1505.
- [26] D. Fausti, R. I. Tobey, N. Dean, S. Kaiser, A. Dienst, M. C. Hoffmann, S. Pyon, T. Takayama, H. Takagi, and A. Cavalleri.
Light-Induced Superconductivity in a Stripe-Ordered Cuprate.
Science, 331(6014):189–191, January 2011.
doi: 10.1126/science.1197294.
- [27] Bryan T. Fichera, Anshul Kogar, Linda Ye, Bilal Gökce, Alfred Zong, Joseph G. Checkelsky, and Nuh Gedik.
Second harmonic generation as a probe of broken mirror symmetry.
Phys. Rev. B, 101(24):241106, June 2020.
doi: 10.1103/PhysRevB.101.241106.
- [28] Bryan T Fichera, Baiqing Lv, Karna Morey, Zongqi Shen, Changmin Lee, Alex Liebman-pel, Anshul Kogar, Takashi Kurumaji, Rodrigo Humberto, Mikel Arruabarrena, Batyr Ilyas, Tianchuang Luo, M Peter, Joseph G. Checkelsky, Joseph Orenstein, and Nuh Gedik.

- Light-induced reorientation transition in an antiferromagnetic semiconductor.
In preparation.
- [29] M. Fiebig, D. Fröhlich, B. B. Krichevtssov, and R. V. Pisarev.
Second Harmonic Generation and Magnetic-Dipole-Electric-Dipole Interference in Antiferromagnetic Cr₂O₃.
Phys. Rev. Lett., 73(15):2127–2130, October 1994.
doi: 10.1103/physrevlett.73.2127.
- [30] M. Fiebig, D. Fröhlich, G. Sluyterman v. L., and R. V. Pisarev.
Domain topography of antiferromagnetic Cr₂O₃ by second-harmonic generation.
Applied Physics Letters, 66(21):2906–2908, May 1995.
doi: 10.1063/1.113699.
- [31] M. Fiebig, D. Fröhlich, Th. Lottermoser, V. V. Pavlov, R. V. Pisarev, and H.-J. Weber.
Second Harmonic Generation in the Centrosymmetric Antiferromagnet NiO.
Phys. Rev. Lett., 87(13):137202, September 2001.
doi: 10.1103/PhysRevLett.87.137202.
- [32] Manfred Fiebig, Victor V. Pavlov, and Roman V. Pisarev.
Second-harmonic generation as a tool for studying electronic and magnetic structures of crystals: review.
Journal of the Optical Society of America B, 22(1):96, January 2005.
doi: 10.1364/JOSAB.22.000096.
- [33] Liang Fu.
Topological Crystalline Insulators.
Physical Review Letters, 106(10), March 2011.
doi: 10.1103/PhysRevLett.106.106802.
- [34] K.K. Fung, J.W. Steeds, and J.A. Eades.
Application of convergent beam electron diffraction to study the stacking of layers in transition-metal dichalcogenides.
Physica B+C, 99(1-4):47–50, January 1980.
doi: 10.1016/0378-4363(80)90208-9.
- [35] Q. D. Gibson, H. Wu, T. Liang, M. N. Ali, N. P. Ong, Q. Huang, and R. J. Cava.

- Magnetic and electronic properties of CaMn₂Bi₂ : A possible hybridization gap semiconductor.
Physical Review B, 91(8), February 2015.
doi: 10.1103/PhysRevB.91.085128.
- [36] K. Nakanishi H. Shiba.
Phenomenological Landau theory of charge density wave phase transitions in layered compounds.
In K. Motizuki, editor, *Structural Phase Transitions in Layered Transition Metal Compounds*, pages 175–266. D. Reidel Publishing Company, 1986.
- [37] J. W. Harter, L. Niu, A. J. Woss, and D. Hsieh.
High-speed measurement of rotational anisotropy nonlinear optical harmonic generation using position-sensitive detection.
Opt. Lett., 40(20):4671, October 2015.
doi: 10.1364/OL.40.004671.
- [38] J. W. Harter, Z. Y. Zhao, J.-Q. Yan, D. G. Mandrus, and D. Hsieh.
A parity-breaking electronic nematic phase transition in the spin-orbit coupled metal Cd₂Re₂O₇.
Science, 356(6335):295–299, April 2017.
doi: 10.1126/science.aad1188.
- [39] T. F. Heinz, M. M. T. Loy, and W. A. Thompson.
Study of si(111) surfaces by optical second-harmonic generation: Reconstruction and surface phase transformation.
Phys. Rev. Lett., 54:63–66, Jan 1985.
doi: 10.1103/PhysRevLett.54.63.
- [40] Tomoya Higo, Kouta Kondou, Takuya Nomoto, Masanobu Shiga, Shoya Sakamoto, Xianzhe Chen, Daisuke Nishio-Hamane, Ryotaro Arita, Yoshichika Otani, Shinji Miwa, and Satoru Nakatsuji.
Perpendicular full switching of chiral antiferromagnetic order by current.
Nature, 607(7919):474–479, July 2022.
doi: 10.1038/s41586-022-04864-1.
- [41] Patrik Hlobil, Akash V. Maharaj, Pavan Hosur, M. C. Shapiro, I. R. Fisher, and S. Raghu.
Elastoconductivity as a probe of broken mirror symmetries.
Physical Review B, 92(3), July 2015.
doi: 10.1103/PhysRevB.92.035148.

- [42] P. C. Hohenberg and B. I. Halperin.
Theory of dynamic critical phenomena.
Rev. Mod. Phys., 49:435–479, Jul 1977.
doi: 10.1103/RevModPhys.49.435.
- [43] Timothy H. Hsieh, Hsin Lin, Junwei Liu, Wenhui Duan, Arun Bansil, and Liang Fu.
Topological crystalline insulators in the SnTe material class.
Nature Communications, 3(1), January 2012.
doi: 10.1038/ncomms1969.
- [44] Takashi Ishiguro and Hiroshi Sato.
High-resolution electron microscopy of discommensuration in the nearly commensurate phase on warming of 1T-TaS₂.
Physical Review B, 52(2):759–765, July 1995.
doi: 10.1103/PhysRevB.52.759.
- [45] John David Jackson.
Classical electrodynamics.
Wiley, New York, NY, 3rd ed. edition, 1999.
- [46] T. Jungwirth, X. Marti, P. Wadley, and J. Wunderlich.
Antiferromagnetic spintronics.
Nature Nanotech, 11(3):231–241, March 2016.
doi: 10.1038/nnano.2016.18.
- [47] T.W.B Kibble and G.R Pickett.
Introduction. Cosmology meets condensed matter.
Phil. Trans. R. Soc. A., 366(1877):2793–2802, August 2008.
doi: 10.1098/rsta.2008.0098.
- [48] Min Gyu Kim, Andi Barbour, Wen Hu, Stuart B. Wilkins, Ian K. Robinson, Mark P. M. Dean, Junjie Yang, Choongjae Won, Sang-Wook Cheong, Claudio Mazzoli, and Valery Kiryukhin.
Real-space observation of fluctuating antiferromagnetic domains.
Sci. Adv., 8(21):eabj9493, May 2022.
doi: 10.1126/sciadv.abj9493.
- [49] Anshul Kogar, Alfred Zong, Pavel E. Dolgirev, Xiaozhe Shen, Joshua Straquadine, Ya-Qing Bie, Xirui Wang, Timm Rohwer, I-Cheng Tung, Yafang Yang, Renkai Li, Jie Yang, Stephen Weathersby, Suji Park, Michael E. Kozina, Edbert J. Sie, Haidan Wen, Pablo Jarillo-Herrero, Ian R. Fisher, Xijie Wang, and Nuh Gedik.

- Light-induced charge density wave in LaTe₃.
Nat. Phys., 16(2):159–163, February 2020.
doi: 10.1038/s41567-019-0705-3.
- [50] G. Kresse and J. Furthmüller.
Efficient iterative schemes for ab initio total-energy calculations using a plane-wave basis set.
Phys. Rev. B, 54:11169–11186, 1996.
doi: 10.1103/PhysRevB.54.11169.
- [51] G. Kresse and D. Joubert.
From ultrasoft pseudopotentials to the projector augmented-wave method.
Phys. Rev. B, 59:1758–1775, 1999.
doi: 10.1103/PhysRevB.59.1758.
- [52] Challa S.S.R. Kumar, editor.
Magnetic Characterization Techniques for Nanomaterials.
Springer Berlin Heidelberg, Berlin, Heidelberg, 2017.
doi: 10.1007/978-3-662-52780-1.
- [53] Christopher Lane, M. M. Piva, P. F. S. Rosa, and Jian-Xin Zhu.
Competition between electronic correlations and hybridization in CaMn₂Bi₂.
arXiv:1911.10122 [cond-mat], November 2019.
arXiv: 1911.10122.
- [54] Changmin Lee, Praveen Vir, Kaustuv Manna, Chandra Shekhar, J. E. Moore, M. A. Kastner, Claudia Felser, and Joseph Orenstein.
Observation of a phase transition within the domain walls of ferromagnetic Co₃Sn₂S₂.
Nat Commun, 13(1):3000, December 2022.
doi: 10.1038/s41467-022-30460-y.
- [55] Robert G Leisure and FA Willis.
Resonant ultrasound spectroscopy.
Journal of Physics: Condensed Matter, 9(28):6001, 1997.
- [56] Kenneth Levenberg.
A method for the solution of certain non-linear problems in least squares.
Quart. Appl. Math., 2(2):164–168, 1944.
doi: 10.1090/qam/10666.

- [57] Chen Li, Xiang Li, T. Deshpande, Xinwei Li, N. Nair, J. G. Analytis, D. M. Silevitch, T. F. Rosenbaum, and D. Hsieh.
High-pressure control of optical nonlinearity in the polar Weyl semimetal TaAs.
Phys. Rev. B, 106(1):014101, July 2022.
doi: 10.1103/PhysRevB.106.014101.
- [58] Arielle Little, Changmin Lee, Caolan John, Spencer Doyle, Eran Maniv, Nityan L. Nair, Wenqin Chen, Dylan Rees, Jörn W. F. Venderbos, Rafael M. Fernandes, James G. Analytis, and Joseph Orenstein.
Three-state nematicity in the triangular lattice antiferromagnet $\text{Fe}_{1/3}\text{NbS}_2$.
Nat. Mater., 19(10):1062–1067, October 2020.
doi: 10.1038/s41563-020-0681-0.
- [59] Baozhu Lu and Darius H. Torchinsky.
Fourier domain rotational anisotropy-second harmonic generation.
Opt. Express, 26(25):33192–33204, Dec 2018.
doi: 10.1364/OE.26.033192.
- [60] Baozhu Lu, Jason D. Tran, and Darius H. Torchinsky.
Fast reflective optic-based rotational anisotropy nonlinear harmonic generation spectrometer.
Review of Scientific Instruments, 90(5):053102, 2019.
doi: 10.1063/1.5080965.
- [61] Andreas Mann, Edoardo Baldini, Ahmad Odeh, Arnaud Magrez, Helmuth Berger, and Fabrizio Carbone.
Probing the coupling between a doublon excitation and the charge-density wave in TaS₂ by ultrafast optical spectroscopy.
Physical Review B, 94(11), September 2016.
doi: 10.1103/PhysRevB.94.115122.
- [62] Donald W. Marquardt.
An Algorithm for Least-Squares Estimation of Nonlinear Parameters.
Journal of the Society for Industrial and Applied Mathematics, 11(2):431–441, June 1963.
doi: 10.1137/0111030.
- [63] I. I. Mazin.
CaMn₂Sb₂: a fully frustrated classical magnetic system, September 2013.
arXiv:1309.3744 [cond-mat].

- [64] D. E. McNally, J. W. Simonson, J. J. Kistner-Morris, G. J. Smith, J. E. Has-singer, L. DeBeer-Schmitt, A. I. Kolesnikov, I. A. Zaliznyak, and M. C. Aronson.
 CaMn_2Sb_2 : Spin waves on a frustrated antiferromagnetic honeycomb lat-tice.
Phys. Rev. B, 91(18):180407, May 2015.
doi: 10.1103/PhysRevB.91.180407.
- [65] Aaron Meurer, Christopher P. Smith, Mateusz Paprocki, Ondřej Čertík, Sergey B. Kirpichev, Matthew Rocklin, AMiT Kumar, Sergiu Ivanov, Jason K. Moore, Sartaj Singh, Thilina Rathnayake, Sean Vig, Brian E. Granger, Richard P. Muller, Francesco Bonazzi, Harsh Gupta, Shivam Vats, Fredrik Johansson, Fabian Pedregosa, Matthew J. Curry, Andy R. Terrel, Štěpán Roučka, Ashutosh Saboo, Isuru Fernando, Sumith Kulal, Robert Cimrman, and Anthony Scopatz.
Sympy: symbolic computing in python.
PeerJ Computer Science, 3:e103, January 2017.
doi: 10.7717/peerj-cs.103.
- [66] A. Migliori, JL Sarrao, William M Visscher, TM Bell, Ming Lei, Z Fisk, and R Gi Leisure.
Resonant ultrasound spectroscopic techniques for measurement of the elastic moduli of solids.
Physica B: Condensed Matter, 183(1-2):1–24, 1993.
- [67] M. Mitrano, A. Cantaluppi, D. Nicoletti, S. Kaiser, A. Perucchi, S. Lupi, P. Di Pietro, D. Pontiroli, M. Riccò, S. R. Clark, D. Jaksch, and A. Caval-leri.
Possible light-induced superconductivity in K_3C_{60} at high temperature.
Nature, 530(7591):461–464, February 2016.
doi: 10.1038/nature16522.
- [68] K Morey, Bryan T. Fichera, Baiqing Lv, Zongqi Shen, and Nuh Gedik.
Automated polarization rotation for multi-axis rotational-anisotropy sec-ond harmonic generation experiments.
In preparation.
- [69] J. A. Nelder and R. Mead.
A Simplex Method for Function Minimization.
The Computer Journal, 7(4):308–313, January 1965.
doi: 10.1093/comjnl/7.4.308.

- [70] Franz Neumann.
Vorlesungen über die Theorie der Elasticität der festen Körper und des Lichtäthers, gehalten an der Universität Königsberg.
Leipzig, B. G. Teubner, 1885.
- [71] Zhuoliang Ni, A. V. Haglund, H. Wang, B. Xu, C. Bernhard, D. G. Mandrus, X. Qian, E. J. Mele, C. L. Kane, and Liang Wu.
Imaging the Néel vector switching in the monolayer antiferromagnet MnPSe₃ with strain-controlled Ising order.
Nat. Nanotechnol., 16(7):782–787, July 2021.
doi: 10.1038/s41565-021-00885-5.
- [72] P. Němec, M. Fiebig, T. Kampfrath, and A. V. Kimel.
Antiferromagnetic opto-spintronics.
Nature Phys, 14(3):229–241, March 2018.
doi: 10.1038/s41567-018-0051-x.
- [73] Shyue Ping Ong, William Davidson Richards, Anubhav Jain, Geoffroy Hautier, Michael Kocher, Shreyas Cholia, Dan Gunter, Vincent L. Chevrier, Kristin A. Persson, and Gerbrand Ceder.
Python Materials Genomics (pymatgen): A robust, open-source python library for materials analysis.
Computational Materials Science, 68:314–319, February 2013.
doi: 10.1016/j.commatsci.2012.10.028.
- [74] Ru-Pin Pan, H. D. Wei, and Y. R. Shen.
Optical second-harmonic generation from magnetized surfaces.
Phys. Rev. B, 39(2):1229–1234, January 1989.
doi: 10.1103/PhysRevB.39.1229.
- [75] Stuart Parkin and See-Hun Yang.
Memory on the racetrack.
Nature Nanotech, 10(3):195–198, March 2015.
doi: 10.1038/nnano.2015.41.
- [76] Shreyas Patankar, Liang Wu, Baozhu Lu, Manita Rai, Jason D. Tran, T. Morimoto, Daniel E. Parker, Adolfo G. Grushin, N. L. Nair, J. G. Analytis, J. E. Moore, J. Orenstein, and D. H. Torchinsky.
Resonance-enhanced optical nonlinearity in the Weyl semimetal TaAs.
Phys. Rev. B, 98(16):165113, October 2018.
doi: 10.1103/PhysRevB.98.165113.

- [77] P. S. Pershan.
Nonlinear Optical Properties of Solids: Energy Considerations.
Phys. Rev., 130(3):919–929, May 1963.
doi: 10.1103/PhysRev.130.919.
- [78] Jesse C. Petersen, Michael D. Caswell, J. Steven Dodge, Ivan A. Sergienko, Jian He, Rongying Jin, and David Mandrus.
Nonlinear optical signatures of the tensor order in Cd₂Re₂O₇.
Nature Phys., 2(9):605–608, September 2006.
doi: 10.1038/nphys392.
- [79] M. M. Piva, S. M. Thomas, Z. Fisk, J.-X. Zhu, J. D. Thompson, P. G. Pagliuso, and P. F. S. Rosa.
Putative hybridization gap in CaMn₂Bi₂ under applied pressure.
Phys. Rev. B, 100(4):045108, July 2019.
doi: 10.1103/PhysRevB.100.045108.
- [80] G. D. Powell, J.-F. Wang, and D. E. Aspnes.
Simplified bond-hyperpolarizability model of second harmonic generation.
Physical Review B, 65(20), May 2002.
doi: 10.1103/PhysRevB.65.205320.
- [81] Richard C. Powell.
Symmetry, Group Theory, and the Physical Properties of Crystals.
Springer New York, NY, 2010.
- [82] William H. Press, Saul A. Teukolsky, William T. Vetterling, and Brian P. Flannery.
Numerical Recipes 3rd Edition: The Art of Scientific Computing.
Cambridge University Press, 3 edition, 2007.
- [83] Sonka Reimers, Dominik Kriegner, Olena Gomonay, Dina Carbone, Filip Krizek, Vit Novák, Richard P. Campion, Francesco Maccherozzi, Alexander Björling, Oliver J. Amin, Luke X. Barton, Stuart F. Poole, Khalid A. Omari, Jan Michalička, Ondřej Man, Jairo Sinova, Tomáš Jungwirth, Peter Wadley, Sarnjeet S. Dhesi, and Kevin W. Edmonds.
Defect-driven antiferromagnetic domain walls in CuMnAs films.
Nat Commun, 13(1):724, February 2022.
doi: 10.1038/s41467-022-28311-x.
- [84] A. Ron, E. Zoghlin, L. Balents, S. D. Wilson, and D. Hsieh.
Dimensional crossover in a layered ferromagnet detected by spin correlation driven distortions.

- Nat Commun*, 10(1):1654, December 2019.
doi: 10.1038/s41467-019-09663-3.
- [85] D. Sa, R. Valentí, and C. Gros.
A generalized Ginzburg-Landau approach to second harmonic generation.
Eur. Phys. J. B, 14(2):301–305, March 2000.
doi: 10.1007/s100510050133.
- [86] C. B. Scruby, P. M. Williams, and G. S. Parry.
The role of charge density waves in structural transformations of 1T-TaS₂.
Philosophical Magazine, 31(2):255–274, February 1975.
doi: 10.1080/14786437508228930.
- [87] James Sethna.
Statistical mechanics: entropy, order parameters, and complexity.
Oxford University Press, 2006.
- [88] K. L. Seyler, A. de la Torre, Z. Porter, E. Zoghlin, R. Polski, M. Nguyen,
S. Nadj-Perge, S. D. Wilson, and D. Hsieh.
Spin-orbit-enhanced magnetic surface second-harmonic generation in
Sr₂IrO₄.
Phys. Rev. B, 102(20):201113, November 2020.
doi: 10.1103/PhysRevB.102.201113.
- [89] Jun-Yi Shan, M. Ye, H. Chu, Sungmin Lee, Je-Geun Park, L. Balents, and
D. Hsieh.
Giant modulation of optical nonlinearity by Floquet engineering.
Nature, 600(7888):235–239, December 2021.
doi: 10.1038/s41586-021-04051-8.
- [90] Y.R. Shen.
The Principles of Nonlinear Optics.
Pure & Applied Optics Series: 1-349. Wiley, 1984.
- [91] Christopher L. Smallwood, James P. Hinton, Christopher Jozwiak, Wen-
tao Zhang, Jake D. Koralek, Hiroshi Eisaki, Dung-Hai Lee, Joseph
Orenstein, and Alessandra Lanzara.
Tracking Cooper Pairs in a Cuprate Superconductor by Ultrafast Angle-
Resolved Photoemission.
Science, 336(6085):1137–1139, June 2012.
doi: 10.1126/science.1217423.

- [92] Albert Spijkerman, Jan L. de Boer, Auke Meetsma, Gerrit A. Wiegers, and Sander van Smaleen.
X-ray crystal-structure refinement of the nearly commensurate phase of 1T-TaS₂ in (3+2)-dimensional superspace.
Physical Review B, 56(21):13757–13767, December 1997.
doi: 10.1103/PhysRevB.56.13757.
- [93] H. T. Stokes, D. M. Hatch, and B. J. Campbell.
Isotropy software suite, .
- [94] H. T. Stokes, D. M. Hatch, and B. J. Campbell.
Isodistort, .
- [95] Zhiyuan Sun and Andrew J. Millis.
Transient Trapping into Metastable States in Systems with Competing Orders.
Phys. Rev. X, 10(2):021028, May 2020.
doi: 10.1103/PhysRevX.10.021028.
- [96] Jeffrey C. Y. Teo, Liang Fu, and C. L. Kane.
Surface states and topological invariants in three-dimensional topological insulators: Application to $\text{Bi}_{1-x}\text{Sb}_x$.
Phys. Rev. B, 78:045426, Jul 2008.
doi: 10.1103/PhysRevB.78.045426.
- [97] David Thouless.
Topological quantum numbers in nonrelativistic physics.
World Scientific, 1998.
- [98] D. H. Torchinsky, H. Chu, L. Zhao, N. B. Perkins, Y. Sizuk, T. Qi, G. Cao, and D. Hsieh.
Structural Distortion-Induced Magnetoelastic Locking in Sr₂IrO₄ Revealed through Nonlinear Optical Harmonic Generation.
Physical Review Letters, 114(9), March 2015.
doi: 10.1103/PhysRevLett.114.096404.
- [99] Darius H. Torchinsky, Hao Chu, Tongfei Qi, Gang Cao, and David Hsieh.
A low temperature nonlinear optical rotational anisotropy spectrometer for the determination of crystallographic and electronic symmetries.
Review of Scientific Instruments, 85(8):083102, August 2014.
doi: 10.1063/1.4891417.

- [100] Pauli Virtanen, Ralf Gommers, Travis E. Oliphant, Matt Haberland, Tyler Reddy, David Cournapeau, Evgeni Burovski, Pearu Peterson, Warren Weckesser, Jonathan Bright, Stéfan J. van der Walt, Matthew Brett, Joshua Wilson, K. Jarrod Millman, Nikolay Mayorov, Andrew R. J. Nelson, Eric Jones, Robert Kern, Eric Larson, C J Carey, İlhan Polat, Yu Feng, Eric W. Moore, Jake VanderPlas, Denis Laxalde, Josef Perktold, Robert Cimrman, Ian Henriksen, E. A. Quintero, Charles R. Harris, Anne M. Archibald, Antônio H. Ribeiro, Fabian Pedregosa, Paul van Mulbregt, and SciPy 1.0 Contributors.
SciPy 1.0: Fundamental Algorithms for Scientific Computing in Python.
Nature Methods, 17:261–272, 2020.
doi: 10.1038/s41592-019-0686-2.
- [101] H. Wackernagel.
Multivariate Geostatistics: An Introduction with Applications.
Springer Berlin Heidelberg, 2003.
- [102] David J. Wales and Jonathan P. K. Doye.
Global Optimization by Basin-Hopping and the Lowest Energy Structures of Lennard-Jones Clusters Containing up to 110 Atoms.
J. Phys. Chem. A, 101(28):5111–5116, July 1997.
doi: 10.1021/jp970984n.
- [103] Hikaru Watanabe and Youichi Yanase.
Group-theoretical classification of multipole order: Emergent responses and candidate materials.
Physical Review B, 98(24), December 2018.
doi: 10.1103/PhysRevB.98.245129.
- [104] Hikaru Watanabe and Youichi Yanase.
Symmetry analysis of current-induced switching of antiferromagnets.
Phys. Rev. B, 98(22):220412, December 2018.
doi: 10.1103/PhysRevB.98.220412.
- [105] Hikaru Watanabe and Youichi Yanase.
Nonlinear electric transport in odd-parity magnetic multipole systems: Application to Mn-based compounds.
Phys. Rev. Research, 2(4):043081, October 2020.
doi: 10.1103/PhysRevResearch.2.043081.
arXiv: 2010.08480.
- [106] N. B. Weber, H. Ohldag, H. Gomonaj, and F. U. Hillebrecht.

- Magnetostrictive Domain Walls in Antiferromagnetic NiO.
Phys. Rev. Lett., 91(23):237205, December 2003.
doi: 10.1103/PhysRevLett.91.237205.
- [107] J.A. Wilson, F.J. Di Salvo, and S. Mahajan.
Charge-density waves and superlattices in the metallic layered transition metal dichalcogenides.
Advances in Physics, 24(2):117–201, March 1975.
doi: 10.1080/00018737500101391.
- [108] Liang Wu, S. Patankar, T. Morimoto, N. L. Nair, E. Thewalt, A. Little, J. G. Analytis, J. E. Moore, and J. Orenstein.
Giant anisotropic nonlinear optical response in transition metal monopnic-tide Weyl semimetals.
Nature Phys., 13(4):350–355, April 2017.
doi: 10.1038/nphys3969.
- [109] X. L. Wu and C. M. Lieber.
Hexagonal Domain-Like Charge Density Wave Phase of TaS₂ Determined by Scanning Tunneling Microscopy.
Science, 243(4899):1703–1705, March 1989.
doi: 10.1126/science.243.4899.1703.
- [110] Y Xiang, D.Y Sun, W Fan, and X.G Gong.
Generalized simulated annealing algorithm and its application to the Thomson model.
Physics Letters A, 233(3):216–220, August 1997.
doi: 10.1016/S0375-9601(97)00474-X.
- [111] H. J. Zeiger, J. Vidal, T. K. Cheng, E. P. Ippen, G. Dresselhaus, and M. S. Dresselhaus.
Theory for displacive excitation of coherent phonons.
Phys. Rev. B, 45:768–778, Jan 1992.
doi: 10.1103/PhysRevB.45.768.
- [112] J. Zhang and R.D. Averitt.
Dynamics and Control in Complex Transition Metal Oxides.
Annu. Rev. Mater. Res., 44(1):19–43, July 2014.
doi: 10.1146/annurev-matsci-070813-113258.
- [113] Alfred Zong, Xiaozhe Shen, Anshul Kogar, Linda Ye, Carolyn Marks, Debanjan Chowdhury, Timm Rohwer, Byron Freelon, Stephen Weathersby, Renkai Li, Jie Yang, Joseph Checkelsky, Xijie Wang, and Nuh Gedik.

Ultrafast manipulation of mirror domain walls in a charge density wave.
Science Advances, 4(10), 2018.
doi: 10.1126/sciadv.aau5501.